

**TWO-DIMENSIONAL JOINT INVERSION OF  
DIRECT-CURRENT RESISTIVITY DATA AND  
MAGNETOTELLURIC DATA**

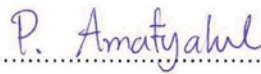
**PUWIS AMATYAKUL**

**A THESIS SUBMITTED IN PARTIAL FULFILLMENT  
OF THE REQUIREMENTS FOR  
THE DEGREE OF MASTER OF SCIENCE (PHYSICS)  
FACULTY OF GRADUATE STUDIES  
MAHIDOL UNIVERSITY  
2010**

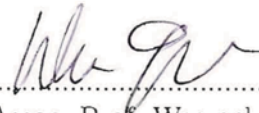
**COPYRIGHT OF MAHIDOL UNIVERSITY**

Thesis  
entitled

**TWO-DIMENSIONAL JOINT INVERSION OF  
DIRECT-CURRENT RESISTIVITY DATA AND  
MAGNETOTELLURIC DATA**



Mr. Puwis Amatyakul  
Candidate



Assoc. Prof. Weerachai Siripunvaraporn,  
Ph.D. (Geophysics)  
Major advisor




Lect. Phichet Kittara,  
Ph.D. (Astrophysics)  
Co-advisor



Lect. Withoon Chunwachirasiri,  
Ph.D. (Physics)  
Co-advisor




Prof. Banchong Mahaisavariya,  
M.D., Dip Thai Board of Orthopedics  
Dean  
Faculty of Graduate Studies  
Mahidol University

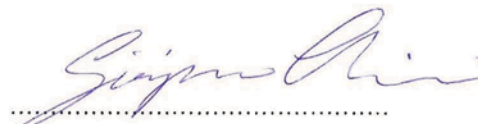


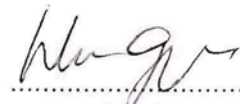
Assoc. Prof. Wannapong Triampo,  
Ph.D. (Physics)  
Program Director  
Master of Science Program  
in Physics  
Faculty of Science  
Mahidol University


Thesis  
entitled  
**TWO-DIMENSIONAL JOINT INVERSION OF  
DIRECT-CURRENT RESISTIVITY DATA AND  
MAGNETOTELLURIC DATA**


was submitted to the Faculty of Graduate Studies, Mahidol University  
for the degree of Master of Science (Physics)  
on  
September 13, 2010

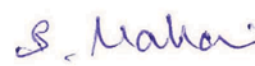
  
.....  
Mr. Puwis Amatyakul  
Candidate

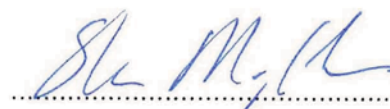
  
.....  
Lect. Siriporn Chaisri,  
Ph.D. (Geophysics)  
Chair

  
.....  
Assoc. Prof. Weerachai Siripunvaraporn,  
Ph.D. (Geophysics)  
Member

  
.....  
Lect. Phichet Kittara,  
Ph.D. (Astrophysics)  
Member

  
.....  
Lect. Withoon Chunwachirasiri,  
Ph.D. (Physics)  
Member

  
.....  
Prof. Banchong Mahaisavariya,  
M.D., Dip Thai Board of Orthopedics  
Dean  
Faculty of Graduate Studies  
Mahidol University

  
.....  
Prof. Skorn Mongkolsuk,  
Ph.D.  
Dean  
Faculty of Science  
Mahidol University

## ACKNOWLEDGEMENTS

I would like to thank my advisor, Assoc. Prof. Dr. Weerachai Siripunvaraporn for his valuable advice, instruction and inspiration, not only for this thesis, but for the research and projects since I was in Grade 11. I appreciate his patience, suggestions and support during the past years of developing this thesis and my life also. I would like to express my sincere gratitude to him for everything he did. For me, he is not just an advisor. He is far beyond that.

I wish to thank my co-advisors, Dr. Phichet Kittara and Dr. Withoon Chunwachirasiri, for providing suggestions and support in several progress reports. I also wish to thank the thesis defense chairman, Dr. Siriporn Chaisri for her support and suggestions for improving the thesis. I appreciate the support and cheerfulness from Dr. Wannapong Triampo and Dr. Srisuda Varamit. Special thanks to the department staff, Miss Nipaporn Suwannawong and Mrs. Wannuch Aroonrungruangkit, for their supports during my M.Sc. study.

I would like to thank Dr. Michael Allen for his valuable suggestions for correcting my English grammar and also providing the  $\LaTeX$  class file.

I would like to thank Mr. Chatchai Vachirateinchai and Mr. Songkhun Boonchaisuk for providing their codes and sharing the ideas. I appreciate their support and encouragement during the time I developed this thesis. I would like to thank my friend, Mr. Tawat Rung-arunwan, for providing his *ready-to-use*  $\LaTeX$  template and all the support he gave to me. I also wish to thank my friends, Nattapong and Punyachai, and people of the Mahidol geophysics research group, Weerachai, Suntaree, Ananya, Patchawee and also B.Sc. students, for their supports and cheerfulness.

I would like to give sincere thanks to the Development and Promotion of Science and Technology Talents Project (DPST) for the financial support since I was in high school.

Special thanks to Dad, Mom, Grandmom, Poomwut and Karn for their cheerfulness, encouragement, love and care. I could not come this far without them. No words can express how important they are to me.

I dedicate this thesis to all of them.

TWO-DIMENSIONAL JOINT INVERSION OF DIRECT-CURRENT RESISTIVITY DATA AND MAGNETOTELLURIC DATA.

PUWIS AMATYAKUL 5036971 SCPY/M

M.Sc. (PHYSICS)

THESIS ADVISORY COMMITTEE : WEERACHAI SIRIPUNVARAPORN, Ph.D. (GEOPHYSICS), PHICHET KITARA, Ph.D. (ASTROPHYSICS), WITHOON CHUNWACHIRASIRI, Ph.D. (PHYSICS)

ABSTRACT

Direct-current resistivity (DCR) and magnetotelluric (MT) methods are popular geophysical techniques used to obtain an electrical resistivity model of subsurfaces. The DCR method is better for shallow surveys up to a few hundred meters in depth. The MT method is commonly applied in deeper explorations to depths of several kilometers. However, the MT method often gives poor accuracy in shallow surveys. The combination of the two method reduces the ambiguity of the interpretation and also makes the subsurface model more accurate.

In this thesis, a two-dimensional (2-D) joint inversion program of the DCR and MT methods was developed using the data-space Occam's (DASOCC) inversion algorithm. The DASOCC algorithm is an efficient version of the classical Occam's inversion. The computational time and the memory usage are significantly reduced making it practical to apply to survey problems. This program was developed by basing it on the existing 2-D DCR inversion program of Vachiratienchai (2007) and the 2-D MT inversion program of Siripunvaraporn & Egbert (2000).

The developed joint inversion program was tested with both synthetic and real data. The results indicate that our developed joint inversion program provides a more accurate and reliable subsurface resistivity model than that of the individual inversion.

KEY WORDS : MAGNETOTELLURIC /  
DIRECT-CURRENT RESISTIVITY /  
JOINT INVERSION

77 pages

การแก้ปัญหาย้อนกลับร่วมในสองมิติของข้อมูลสภาพต้านทานไฟฟ้ากระแสตรงและข้อมูลแมกนีโตเทลลูริก

TWO-DIMENSIONAL JOINT INVERSION OF DIRECT-CURRENT RESISTIVITY DATA AND MAGNETOTELLURIC DATA

ภูวิศ อมาตยกุล 5036971 SCPY/M

วท.ม. (ฟิสิกส์)

คณะกรรมการที่ปรึกษาวิทยานิพนธ์ : วีระชัย สิริพันธ์วรารณ, Ph.D. (GEOPHYSICS), พิเชษฐ กิจธรา, Ph.D. (ASTROPHYSICS), วิฑูร ชื่นวชิรศิริ, Ph.D. (PHYSICS)

บทคัดย่อ

วิธีสภาพต้านทานไฟฟ้ากระแสตรงและวิธีแมกนีโตเทลลูริก เป็นเทคนิคที่นิยมในการสำรวจทางธรณีฟิสิกส์ ทั้งสองวิธีให้แบบจำลองสภาพต้านทานไฟฟ้าใต้ผิวดิน โดยปกติวิธีสภาพต้านทานไฟฟ้ากระแสตรงมีความแม่นยำในการสำรวจระดับตื้น ที่มีความลึกไม่เกินห้าร้อยเมตรจากผิวดิน ในขณะที่วิธีแมกนีโตเทลลูริกจะใช้ในการสำรวจระดับลึกโดยมีความลึกของการสำรวจได้ถึงหลายกิโลเมตร แต่บางครั้งแบบจำลองที่ได้จะขาดความแม่นยำในระดับตื้น การรวมข้อมูลจากทั้งสองวิธีจะช่วยเพิ่มความถูกต้อง และลดความกำกวมในการตีความจากแบบจำลองที่ได้

วิทยานิพนธ์ฉบับนี้ เป็นการพัฒนาการแก้ปัญหาย้อนกลับร่วมในสองมิติของข้อมูลสภาพต้านทานไฟฟ้ากระแสตรงและข้อมูลแมกนีโตเทลลูริก ด้วยอัลกอริทึมดาต้าสเปสจากหลักของออกแคม โดยพัฒนาเพิ่มเติมจากการแก้ปัญหาย้อนกลับในสองมิติของข้อมูลสภาพต้านทานไฟฟ้าของ วชิระเกียรติชัย (2007) และการแก้ปัญหาย้อนกลับในสองมิติของข้อมูลแมกนีโตเทลลูริกของ สิริพันธ์วรารณ และ เอ็กเบิร์ท (2000) อัลกอริทึมดาต้าสเปสเป็นการพัฒนาที่มีประสิทธิภาพจากหลักการของออกแคมในแบบดั้งเดิม โดยสามารถลดเวลาในการคำนวณและจำนวนหน่วยความจำที่ใช้ได้อย่างเห็นได้ชัด เหมาะที่จะนำมาประยุกต์ในการสำรวจทางธรณีฟิสิกส์

จากการทดสอบการแก้ปัญหาย้อนกลับร่วมที่พัฒนาขึ้น โดยข้อมูลสังเคราะห์และข้อมูลที่ได้จากการสำรวจจริงพบว่า แบบจำลองที่ได้จากการแก้ปัญหาย้อนกลับร่วมจากทั้งสองข้อมูลนั้นมีความแม่นยำและน่าเชื่อถือมากกว่าการแก้ปัญหาย้อนกลับจากข้อมูลใดข้อมูลหนึ่ง

## CONTENTS

	<b>Page</b>
<b>ACKNOWLEDGEMENTS</b>	<b>iii</b>
<b>ABSTRACT (ENGLISH)</b>	<b>iv</b>
<b>ABSTRACT (THAI)</b>	<b>v</b>
<b>LIST OF TABLES</b>	<b>viii</b>
<b>LIST OF FIGURES</b>	<b>ix</b>
<b>CHAPTER I Introduction</b>	<b>1</b>
1.1 Geophysical Exploration	1
1.1.1 Survey	2
1.1.2 Modeling	2
1.1.3 Interpretation and non-uniqueness	4
1.2 Research problem	4
1.3 Outline of the thesis	4
<b>CHAPTER II Direct-current resistivity and magnetotelluric methods</b>	<b>6</b>
2.1 Electrical resistivity property of the Earth's subsurface	6
2.2 Direct-current resistivity method	8
2.2.1 Principle of direct-current resistivity method	8
2.2.2 Field measurement	9
2.2.3 Electrode configuration	10
2.2.4 Data response and interpretation	12
2.3 Magnetotelluric method	15
2.3.1 Principle of magnetotelluric method	15

## CONTENTS (cont.)

	<b>Page</b>
2.3.2 Field measurement	16
2.3.3 Data responses and interpretation	17
<b>CHAPTER III Inversion algorithm</b>	<b>20</b>
3.1 Geophysical inversion	20
3.2 Occam's inversion	21
3.2.1 Data functional	22
3.2.2 Model functional	23
3.2.3 Minimization of an objective function	24
3.3 Data-space Occam's inversion	25
3.4 Previous implementations of joint inversion of DCR & MT	28
3.5 Implementation to 2-D joint inversion of DCR & MT	29
3.5.1 Data functional	29
3.5.2 Forward modeling	29
3.5.3 Sensitivity matrix	32
3.5.4 Model covariance matrix $\mathbf{C}_m$	32
3.6 Inversion process	34
3.6.1 Line search for $\lambda$	34
<b>CHAPTER IV Numerical and real experiments</b>	<b>35</b>
4.1 Synthetic experiments	35
4.1.1 Synthetic case I: The two buried boxes	35
4.1.2 Synthetic case II: Complex structure	45

**CONTENTS (cont.)**

	<b>Page</b>
4.1.3 Synthetic case III: MT static shift correction	53
4.2 Real experiment	58
<b>CHAPTER V Conclusion</b>	<b>70</b>
<b>REFERENCES</b>	<b>72</b>
<b>BIOGRAPHY</b>	<b>77</b>

## LIST OF TABLES

<b>Tables</b>	<b>Page</b>
1.1 Data responses from the corresponding acquisition survey	2
2.1 Resistivity of some minerals at 0 °C.	7

## LIST OF FIGURES

Figures	Page
1.1 Elements of geophysical exploration.	1
1.2 Dimensionality of the surveys and the models. (a) 1-D model, (b) 2-D model and (c) 3-D model.	3
2.1 Electrical resistivity of minerals, rocks and sediments.	7
2.2 Electrical potential from two point current source.	9
2.3 Typical electrode configuration.	9
2.4 Electrode arrays commonly used in surveys.	11
2.5 Sounding curve of a DCR survey.	13
2.6 A systematic arrangement of Wenner arrays investigating different depths and locations.	14
2.7 Pseudosection of DCR electrode array calculated from the synthetic model (a) Dipole-dipole array, (b) Wenner array and (c) Schlumberger array. The synthetic pseudosections are generated from the model of one conductive box buried in a resistive homogeneous host (d). The electrode spacing is 5 m with 10 levels of pseudodepth.	14
2.8 A typical configuration of a single MT station	16
2.9 The acquired components of the time varying electric and magnetic fields	17
2.10 MT sounding curve. (a) Apparent resistivity and (b) phase are plotted as a function of frequency from a two layers model with various values of resistivity of the second layer.	18
2.11 (a) is the pseudosection of 9 MT stations with spacing of 20 m generated from synthetic model. (b) is an apparent resistivity pseudosection. (c) is a phase pseudosection.	19
3.1 The diagram shows the basic idea of the general inversion.	20
3.2 2-D model discretization.	22

## LIST OF FIGURES (cont.)

Figures	Page
4.1 Synthetic model of the two boxes case	36
4.2 RMS misfits and model norms for each iteration from (a) single DCR inversion, (c) single MT inversion and (e) joint inversion of DCR & MT. The solid line with the circles represent the RMS misfit. The dashed line with the squares represent the model norm. $\log_{10} \lambda$ for each iteration are also shown (b), (d) and (f) for DCR, MT and joint inversion, respectively.	37
4.3 Inverted models from (a) the single DCR inversion, (b) the single MT inversion and (c) the joint inversion of DCR & MT. The white squares show the boundary of the boxes from the synthetic model.	39
4.4 Schlumberger array data. All use the same color scale.	40
4.5 Apparent resistivity and phase responses in TE mode.	41
4.6 Apparent resistivity and phase responses in TM mode.	42
4.7 The model resolution matrix (a) DCR, (b) TE & TM and (c) TE & TM + DCR.	43
4.8 Synthetic model of case II.	45
4.9 Inverted models of the inversions (a) single DCR inversion, (b) single MT inversion and (c) joint inversion of DCR & MT. The white squares show the boundary of the features from the synthetic model.	47
4.10 DCR data of Schlumberger array from the inversions. All use the same color scale.	48
4.11 Apparent resistivity and phase responses in TE mode from the MT inversions.	49
4.12 Apparent resistivity and phase responses in TM mode from the MT inversions.	50
4.13 The model resolution matrix (a) DCR, (b) TE&TM (c) TE&TM+DCR.	51
4.14 An example three-layer model, (a) is an example model without surface inhomogeneity. (b) is an example model with surface inhomogeneity.	53

## LIST OF FIGURES (cont.)

Figures	Page
4.15 Synthetic data, (a) generated from an example model without surface inhomogeneity. (b) generated from an example model with surface inhomogeneity.	55
4.16 The inverted model from a single MT inversion, (a) from the data without surface inhomogeneity. (b) from the data with surface inhomogeneity.	56
4.17 Inverted model from a single DCR inversion. The data is generated including the near-surface inhomogeneity	56
4.18 Inverted model from joint inversion of DCR & MT.	57
4.19 The data generated from the inverted model of the joint inversion of DCR & MT.	57
4.20 The exploration plan at the Creex Extension (CreeX) project (After Cameco Corporation). The established survey grid is used in both AMT and pole-pole DCR surveys. We are authorized to access the data of the profile L0 which passes through the ore mining site.	58
4.21 The generic model of an unconformity-type uranium deposition in the Athabasca Basin (after Tuncer <i>et al.</i> , 2006). There are four major groups of Manitou Falls formation (MF). MFd is the medium-fine sandstone with mudstone intraclasts; MFc is the granule sandstone; MFb is the interbedded conglomerate and pebbly sandstone; and MFa is the discontinuous basal conglomerate, intercalated coarse sandstone, conglomerate and red mudstone. The metmorphic basement consists of the hanging wall of Wollaston Group (WG) and Mudjatik Domain (MD) footwall (see also Mwenifumbo, 2004).	59
4.22 The resistivity model from a single DCR inversion.	61
4.23 The resistivity models obtained from a single MT inversion. (a) TE mode only, (b) TM model only and (c) TE&TM modes.	63
4.24 The resistivity models obtained from a joint inversion. (a) TE+DCR, (b) TM+DCR (c) TE&TM+DCR.	64
4.25 DCR data of Schlumberger array from the inversions. All use the same color scale	65

**LIST OF FIGURES (cont.)**

<b>Figures</b>	<b>Page</b>
4.26 Apparent resistivity and phase responses in TE mode from the MT inversions.	66
4.27 Apparent resistivity and phase responses in TM mode from the MT inversions.	67
4.28 The model resolution matrix (a) DCR, (b) TE&TM (c) TE&TM+DCR.	68

# CHAPTER I

## INTRODUCTION

In order to understand the importance of this work, we start the first chapter by covering the basic elements of geophysical exploration. A conceptual understanding would lead the reader to appreciate the applicability of this thesis. The research problem and the outline of this thesis will be described at the end of this chapter.

### 1.1 Geophysical Exploration

Geophysical exploration is widely used as a tool to reveal the subsurface structures in various applications such as mineral ore, hydrocarbon, geothermal, environment and crustal studies. In many situations, direct sampling, e.g. drilling, core logging and borehole, is impractical or insufficient. Subsurface imaging techniques can be used for measuring the physical data at the surface to obtain the Earth's properties without direct sampling.

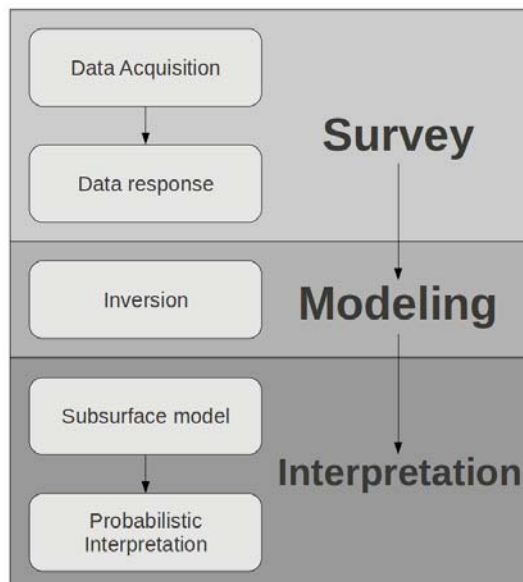


Figure 1.1: Elements of geophysical exploration.

Figure 1.1 illustrates the processes of geophysical exploration. There are three main parts: survey, modeling and inversion, and interpretation. The following

sections are organized to give an overview of each parts which is connected to the research problem of this thesis.

### 1.1.1 Survey

Different rocks have distinguishable physical properties. To sense these rock properties, a geophysical survey technique originates from the governing physics of the measurements associated with those physical properties.

For an individual survey, a specific instrument is used as an acquisition tool. The physical data can be acquired when a natural or man-made energy source is applied to the ground for collecting the information of the subsurface variation to the surface measurements. The acquired data are then transformed into the data response which is more convenient to indicate spatial variation of the physical property. Table 1.1 shows the examples of the acquisition data and their corresponding data responses.

Survey	Measuring quantity	Data response
Direct current resistivity	Potential difference	Apparent resistivity
Magnetotelluric	Electric & magnetic field	Apparent resistivity & phase
Gravity	Gravitational acceleration	Gravity anomaly

Table 1.1: Data responses from the corresponding acquisition survey

To start a field exploration, suitable techniques are selected from the geological characteristics of the target inside the investigation area. For example, in uranium exploration, uranium usually co-exists with graphite which is conductive and easily distinguished from a resistive host. The resistivity contrast of the target can be detected with EM or resistivity surveys.

### 1.1.2 Modeling

Modeling is an important procedure for determining the model of the subsurface from the data response by the associated governing physics principles. There are two essential parts of geophysical modeling, forward modeling and inversion.

#### Forward modeling

Forward modeling is a process which calculates the predicted data response of a survey from the known model through theoretical or numerical calculations. In most cases, numerical calculation is required because of the model complexity.

## Inversion

For geophysical problems, there is no simple and direct relation to calculate the subsurface model from the measurement data. This can be conducted through a mathematical optimization process called “inversion” which finds the model that fits the input data.

## Dimensionality of survey and model

Geophysical surveys can be conducted in many levels. For a simple structure when the Earth is only a function of depth (see Figure 1.2a), a single site is enough to probe the Earth. In a more complex structure such as when a fault zone cuts across, the Earth structure is invariant along the strike direction, here the  $x$ -direction (see Figure 1.2b). To map the structure, a profile or a series of stations are usually placed across the strike direction. For the most complicated structures, the Earth varies in all directions (see Figure 1.2c). To map the anomalies, a series of 2-D profiles or 3-D stations are usually used to cover the whole area.

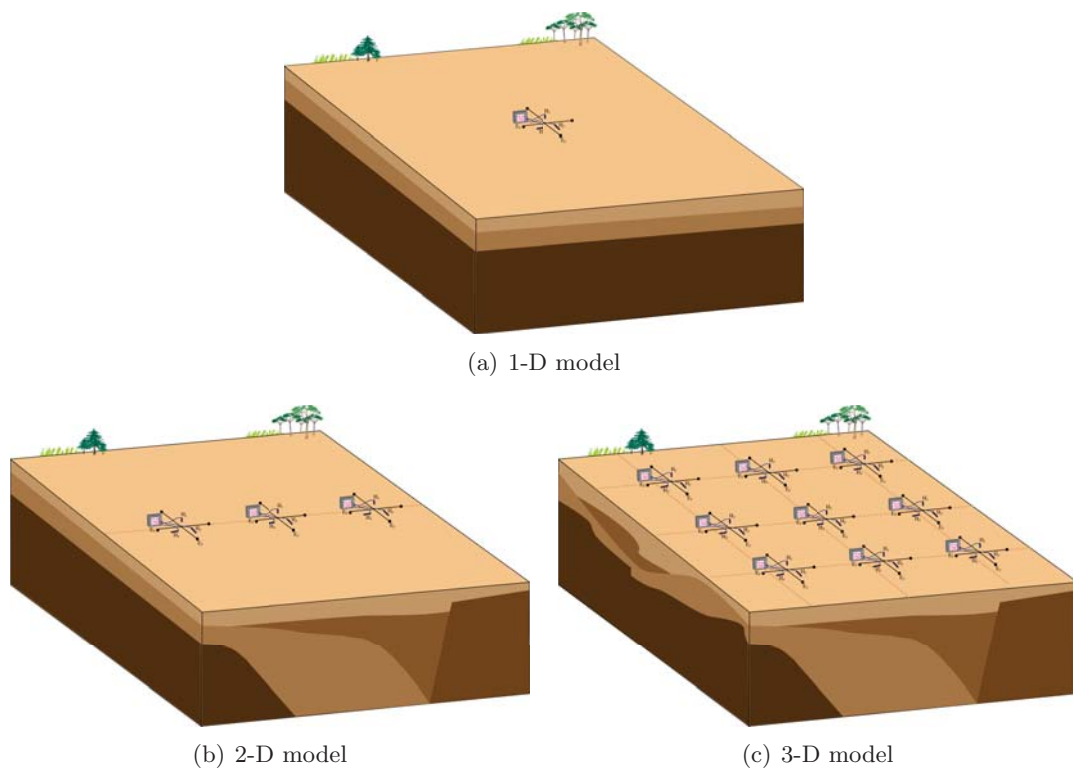


Figure 1.2: Dimensionality of the surveys and the models. (a) 1-D model, (b) 2-D model and (c) 3-D model.

### 1.1.3 Interpretation and non-uniqueness

An interpreter converts the physical models obtained from the inversion to geological models. Inversion is a type of underdetermined system. An inverse solution is therefore non-unique, i.e., more than one solution can fit the data at the same level. Prior information, geology of the area and interpreter's experience are the main factors for reliable interpretation to help avoiding ambiguity due to the non-uniqueness.

## 1.2 Research problem

In the past decades, integrated methods have been used in many explorations. Integrated methods provide a better constraint by increasing the amount of acquired data from the investigation area to help reduce the ambiguity in interpretation. In this thesis, we propose the integration of the direct current resistivity and magnetotelluric methods for mapping the Earth's resistivity structure.

The direct current resistivity (DCR) and magnetotelluric (MT) methods are some of the most used methods in modern geophysical surveys. Both DCR and MT sense the same physical property, the electrical resistivity. DCR is usually used for shallow explorations and provides high resolution from a few meters to hundreds of meters investigation depth. MT has a deeper investigation depth from a few meters to the mantle depth which corresponds to a wide range of EM frequencies. Therefore, combining the different characteristics of both methods helps better constrain the solution.

Here, the efficient 2-D joint inversion of DCR and MT data is developed based on the existing 2-D DCR inversion of Vachiratienchai (2007) and 2-D MT inversion of Siripunvaraporn & Egbert (2000). We demonstrate that the model resolution of the joint inversion is better than that of the individual DCR or MT inversions. In addition, the joint inversion could help with solving MT static shift problems due to a very small near surface structure.

## 1.3 Outline of the thesis

This thesis consists of five chapters. The first chapter reviews the fundamentals of geophysics and the basic idea of geophysical inversion. The research problem is mentioned here.

The fundamentals and the corresponding theory of the DCR and the MT methods are given in Chapter 2 starting with the electrical property of the subsurface. Measurement, common configurations, and data interpretation will then be described. In addition, advantages and limitations of both methods are discussed.

In Chapter 3, the elements of the inversion algorithms are explained including the 2-D forward modeling of both techniques, the sensitivity calculation, data covariance and model covariance. We then describe our developed joint inversion code based on the data space Occam's inversion.

In Chapter 4, the developed joint inversion is validated by numerical experiments with various synthetic models. The joint inversion is also applied to real measurements. Resolution analysis is then applied to the results to show the improvement of the inverted model obtained from the joint inversion. Finally, the last chapter includes the conclusion.

## CHAPTER II

### DIRECT-CURRENT RESISTIVITY AND MAGNETOTELLURIC METHODS

In this chapter, the fundamentals of both DCR and MT methods are described. The chapter begins with the electrical resistivity of the Earth. For each method, the contents are then consecutively organized starting with the governing physics principles, field surveys, data responses and interpretation. At the end of this chapter, the advantages and limitations of each method are discussed.

#### 2.1 Electrical resistivity property of the Earth's subsurface

Conductivity is the ability of a material to conduct an electron current when an electrical potential difference is applied. The electrical conductivity ( $\sigma$ ) in an isotropic media is defined as the ratio of the current density ( $\mathbf{J}$ ) to the electric field ( $\mathbf{E}$ ),

$$\mathbf{J} = \sigma \mathbf{E}. \quad (2.1)$$

The SI unit of the conductivity is the siemens per meter ( $\text{S m}^{-1}$ )

In this thesis, the electrical conductivity will be used as well as the electrical resistivity. Resistivity is a measure of how strongly a material opposes the flow of electric current when an electrical potential difference is applied. The electrical resistivity ( $\rho$ ) of an isotropic media is the reciprocal of the conductivity,

$$\rho = \frac{1}{\sigma}.$$

The SI unit of the resistivity is the ohm meter ( $\Omega \text{ m}$ )

Table 2.1 shows the resistivity values of various minerals. They are usually deposited with rocks aggregating at the subsurface. The resistivity of rocks also depends on porosity, filled-in water content and dissolved electrolytes. The most satisfactory expression for the overall resistivity of a rock is Archie's law which is attributed to Archie (1942). The expression is conveniently written in terms of the conductivity,

$$\sigma = a\sigma_w S^n \phi^m, \quad (2.2)$$

Refined metal	$\rho$ ( $\Omega$ m)
Gold	$2 \times 10^{-8}$
Tin	$10 \times 10^{-8}$
Lead	$14 \times 10^{-8}$
Titanium	$83 \times 10^{-8}$

Table 2.1: Resistivity of some minerals at 0 °C.

where  $\sigma$  is the overall conductivity of the rock,  $\sigma_w$  is the conductivity of the electrolyte filling the pore structure,  $S$  is the fraction of the pore space filled with fluid,  $\phi$  is the volume fraction of void space in the rock, and  $a$ ,  $m$  and  $n$  are the parameters of the given rock obtained from the standard experiment.

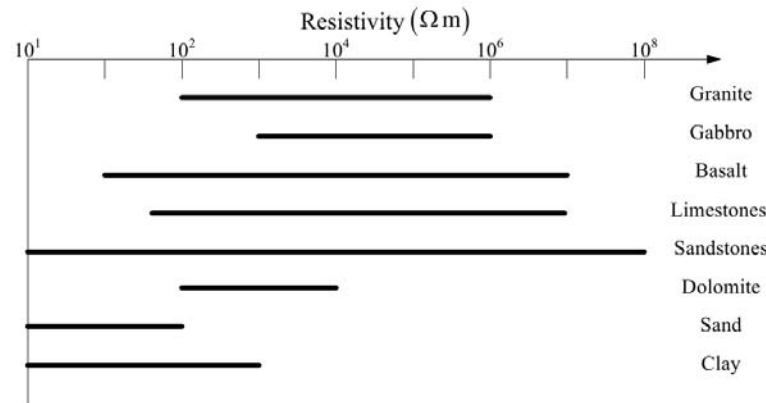


Figure 2.1: Electrical resistivity of minerals, rocks and sediments.

The resistivity of rock can be predetermined using equation (2.2). However, the resistivity of rocks varies according to the geological conditions. Several geological targets have a wide range of an overlapping resistivity while several have a specific value as shown in Figure 2.1. In spite of this variation and overlapping resistivity, the obtained model in conjunction with prior geology information remains one of the most useful models to reveal the subsurface.

All EM methods sense the resistivity variation of the subsurface. One EM method could be used to obtain a resistivity image. However, in several situations, when the area is complicated, the combination of more than one EM method is preferred to reduce the ambiguity of an interpretation (see Jupp & Vozoff, 1977; Tripp *et al.*, 1978; Harinarayana, 1999). In this chapter, we introduce the direct current resistivity and magnetotelluric methods.

## 2.2 Direct-current resistivity method

Direct current resistivity (DCR) is one popular geophysical method to reveal the subsurface structures in terms of the spatial resistivity variation where the source is direct current injected into the ground. The typical car battery is commonly used as the source. While the current is applied into the ground, the potential difference is measured. The measurements are then transformed into the “apparent resistivity”.

The investigation depth of DCR depends on the measuring electrode configuration and power of the source. DCR is generally used in various areas characterized by the resistivity contrast of the geologic targets, for example, in shallow mining, ground water exploration, contaminated waste site, archeology (Karlik & Kaya, 2001; Buselli & Lu, 2001; Corwin & Lesch, 2005). These are for shallow surveys. However, it can be used as deep as 500 m, for example, in sedimentary studies and shallow tectonic studies (Zohdy & Bisdorf, 1990).

### 2.2.1 Principle of direct-current resistivity method

The scalar potential distribution in a homogeneous Earth from an injecting current point source can be calculated using Ohm’s law (2.1).  $\mathbf{J}$  is defined as the ratio of the injecting current to the dissipating area. The resistivity of air is very high compared to that of the Earth. The current flow in the air can be eliminated. The dissipating area is then  $2\pi r^2$  (the area of a hemispherical shell at a given distance  $r$  from the injecting point source). Hence

$$J = \frac{I}{2\pi r^2}, \quad (2.3)$$

where  $I$  denotes an injecting current.

The electric field  $\mathbf{E}$  in equation (2.1) is the gradient of the scalar electrical potential  $\phi$ ,

$$\mathbf{E} = -\nabla\phi. \quad (2.4)$$

For an assumed homogeneous earth with resistivity  $\rho$ , the potential at any given  $r$ ,  $\phi(r)$ , can be obtained by substituting (2.3) and (2.4) into equation (2.1). This gives

$$\frac{\rho I}{2\pi r^2} = -\frac{\partial\phi}{\partial r}. \quad (2.5)$$

Rewriting equation (2.5) in an integral form,

$$\phi(r) = \int d\phi = -\rho I \int_0^r \frac{1}{2\pi r'^2} dr'. \quad (2.6)$$

Integrating equation (2.6), the potential of a point current source can be obtained,

$$\phi(r) = \frac{\rho I}{2\pi r}. \tag{2.7}$$

In the case that there are two injecting current sources denoted by  $A$  and  $B$  (see Figure 2.2), the potential at point  $P$  can be calculated as the superposition of the scalar potentials  $\phi_{P,A}$  and  $\phi_{P,B}$  from point sources  $A$  and  $B$ ,

$$\phi_P = \phi_{P,A} + \phi_{P,B}.$$

Considering  $I_B = -I_A = -I$  in equation (2.7),  $\phi_P$  can be simplified to give

$$\phi_P = \frac{\rho I}{2\pi} \left( \frac{1}{AP} - \frac{1}{PB} \right), \tag{2.8}$$

where  $AP$  is the distance between point  $A$  and  $P$ , and  $PB$  is the distance between point  $P$  and  $B$ .

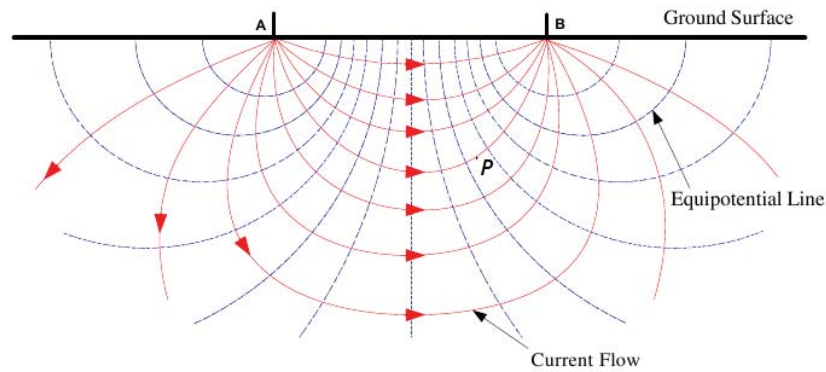


Figure 2.2: Electrical potential from two point current source.

### 2.2.2 Field measurement

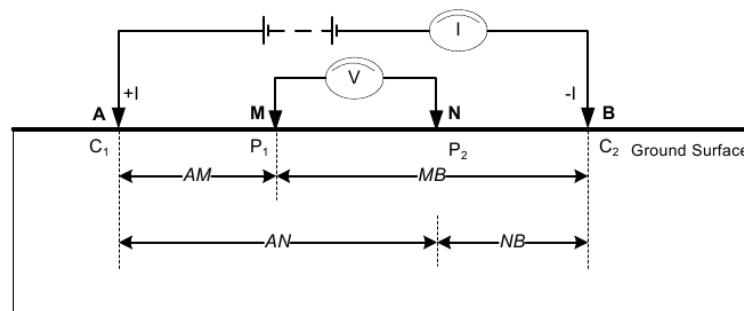


Figure 2.3: Typical electrode configuration.

Figure 2.3 shows a typical electrode configuration of a DCR survey. There are two injecting current electrodes and two potential electrodes. While electrode  $A$  and  $B$  inject the current into the subsurface, the potential difference  $\phi_{MN}$  between electrode  $M$  and  $N$  is then measured. The potential difference  $\phi_{MN}$  can be expressed as

$$\phi_{MN} = \phi_M - \phi_N \quad (2.9)$$

Using equation (2.2), equation (2.9) becomes

$$\phi_{MN} = \frac{\rho I}{2\pi} \left[ \left( \frac{1}{AM} - \frac{1}{MB} \right) - \left( \frac{1}{AN} - \frac{1}{NB} \right) \right]. \quad (2.10)$$

Therefore, the expression of the resistivity according to the potential difference and the injecting current can be obtained from

$$\rho = \frac{\phi_{MN}}{I} K, \quad (2.11)$$

where

$$K = 2\pi \left[ \left( \frac{1}{AM} - \frac{1}{MB} \right) - \left( \frac{1}{AN} - \frac{1}{NB} \right) \right]^{-1}. \quad (2.12)$$

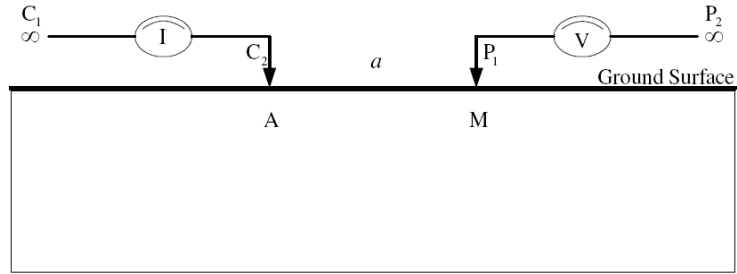
$K$  is defined as the geometric factor which depends on the electrode configuration.

### 2.2.3 Electrode configuration

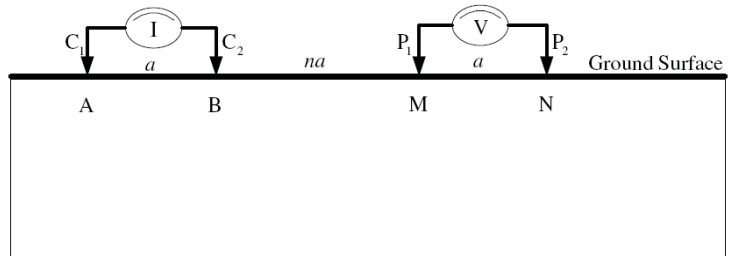
There are various types of DCR array configurations. The orientation of both current and potential electrodes determines the investigation depth and the subsurface resolution in both lateral and vertical directions. Each electrode array has its own characteristic and has been used in different kinds of explorations according to the specific geology of the investigation area. Here, four of the most famous electrode configurations are described (see Figure 2.4).

#### Pole-Pole array

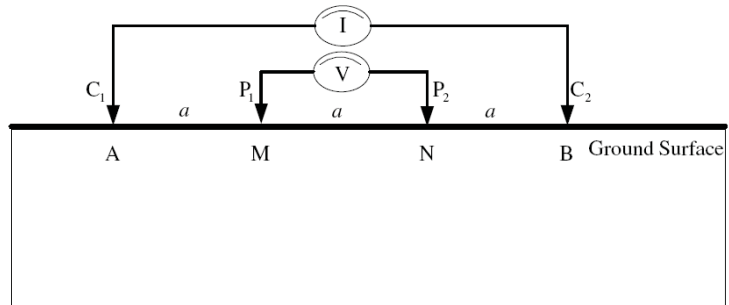
The pole-pole array (Figure 2.4a) consists of one current electrode  $A$  and one potential electrode  $M$ . The current electrode  $B$  and the potential electrode  $N$  are theoretically placed at an infinite distance, practically 3 times a profile length. Thus the impact from electrodes  $B$  and  $N$  is ignored.  $a$  is the distance between current electrode  $A$  and potential electrode  $M$ . Pole-pole has the deepest investigation depth and widest horizontal coverage (Loke & Barker, 1996). But it could have a large amount of telluric noises.



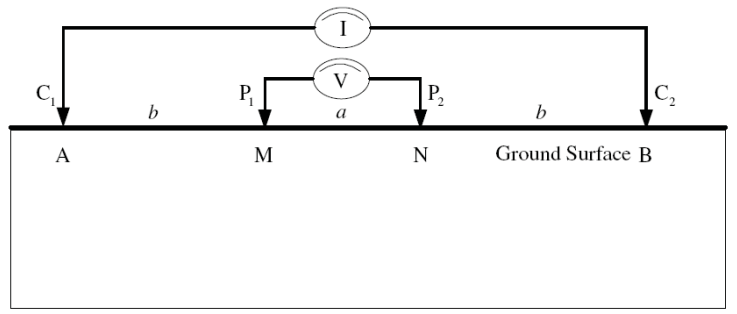
(a) Pole-pole array



(b) Dipole-dipole array



(c) Wenner array



(d) Schlumberger array

Figure 2.4: Electrode arrays commonly used in surveys.

### Dipole-Dipole array

For a dipole-dipole array (Figure 2.4b), the electrode spacing between the current dipoles ( $A$  and  $B$ ) and the potential dipoles ( $M$  and  $N$ ) remains  $a$  throughout the survey. The distance between the current dipoles and the potential dipoles is consequently extended by  $na$  to sense deeper structures. This array is good in mapping vertical structures (Loke & Barker, 1996) but it has a weak signal strength in which noises from the surrounding area can dominate.

### Wenner array

For a Wenner array (Figure 2.4c), the potential dipoles are located between the current dipoles. This array has a stronger signal than the dipole-dipole array. The electrode spacing ( $a$ ) between electrodes  $A - M$ ,  $M - N$  and  $N - B$  are equal. For sensing a deeper subsurface, the electrode spacing is then equally extended by  $na$ . It is good in mapping horizontal structures (Loke & Barker, 1996).

### Schlumberger array

For a Schlumberger array (Figure 2.4d), the potential dipoles are also located between the current dipoles. But both current electrodes are placed symmetrically opposite the potential dipoles or a distance  $b = na$ . It also has a strong signal and is moderately sensitive to both horizontal and vertical structures (Loke & Barker, 1996).

## 2.2.4 Data response and interpretation

Directly interpreting the potential may be difficult. In DCR surveys, the apparent resistivity  $\rho_a$  is mostly used for field interpretation. It is defined by

$$\rho_a = \frac{V}{I}K, \quad (2.13)$$

where  $V$  denotes the measuring potential associated with the injecting current  $I$ .

A plot of  $\rho_a$  as a function of the electrode spacing can give us a picture of the resistivity as a function of depth (Figure 2.5). Current from a larger electrode spacing flows deeper and therefore senses a deeper structure. In the homogeneous case,  $\rho_a = \rho$  and equation (2.13) is the same as equation (2.11). The geometric factor  $K$  varies with the electrode configuration used and can be calculated from equation (2.12).

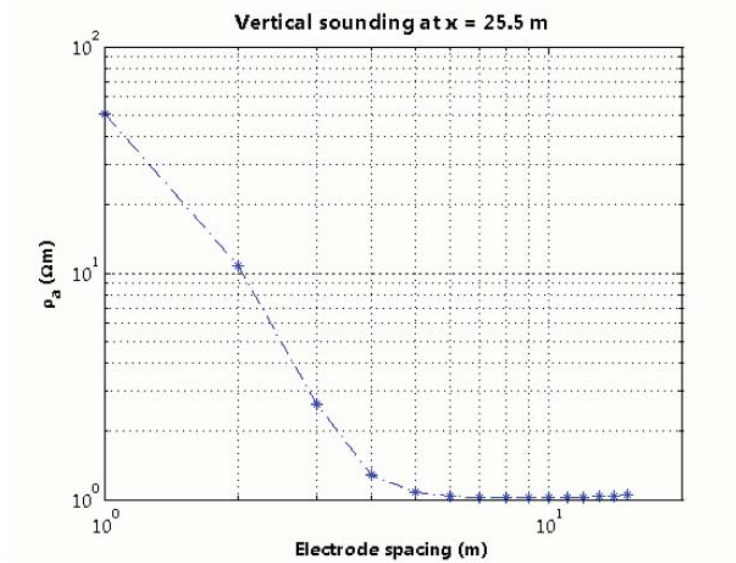


Figure 2.5: Sounding curve of a DCR survey.

### DCR pseudosection

In order to obtain the resistivity variation of the subsurface in 2-D, the measurement must be conducted at the other location in the same profile with different electrode spacing. This is demonstrated in Figure 2.6 for the Wenner array.

For the pseudodepth of  $n = 1$  (electrode spacing is  $a$ ), electrode  $A$ ,  $M$ ,  $N$  and  $B$  are placed at nodes 1, 2, 3 and 4, respectively. Then this electrode array is moved one electrode to the right to obtain another acquisition. The same procedure is repeated until the last electrode  $B$  reaches the end of the profile. A new set of  $n = 2$  (electrode spacing is  $2a$ ) is then operated similarly with twice of an electrode spacing until the end of the profile is reached. The systematic moving of the electrode array is repeated until the pseudodepth reaches a maximum or to the desired level. The plot of the apparent resistivity and pseudodepth is called the pseudosection.

The pseudosection is often used as a qualitative interpretation of the resistivity variation of the subsurface and also helps appraising the quality of the acquired data. Figure 2.7 shows a series of pseudosections from the dipole-dipole (Figure 2.7a), Wenner (Figure 2.7b) and Schlumberger (Figure 2.7c) arrays generated from the synthetic model shown in Figure 2.7d. The colorbar indicates the value of the apparent resistivity in  $\log_{10}$  scale. From the pseudosections, different features occur between each pseudosection even though they are generated from the same model. Interpretation of the subsurface directly from pseudosection needs experience. In order to obtain the true resistivity distribution of the subsurface, 2-D inversion is then required.

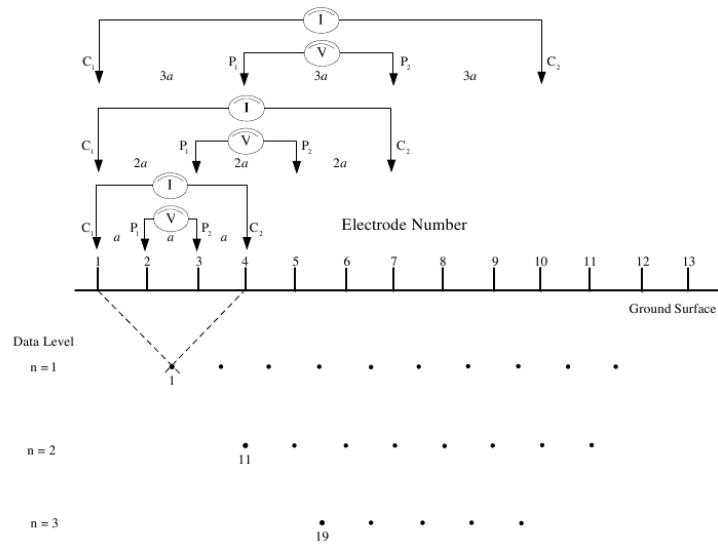


Figure 2.6: A systematic arrangement of Wenner arrays investigating different depths and locations.

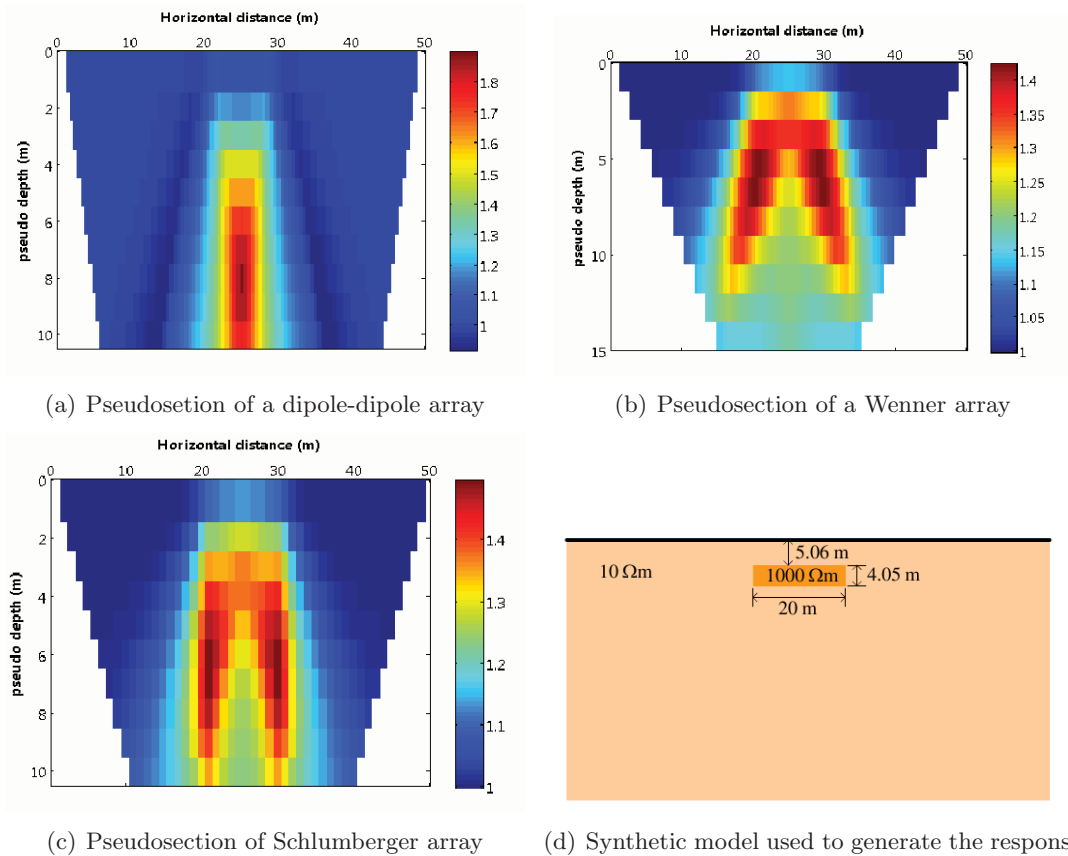


Figure 2.7: Pseudosection of DCR electrode array calculated from the synthetic model (a) Dipole-dipole array, (b) Wenner array and (c) Schlumberger array. The synthetic pseudosections are generated from the model of one conductive box buried in a resistive homogeneous host (d). The electrode spacing is 5 m with 10 levels of pseudodepth.

## 2.3 Magnetotelluric method

The magnetotelluric (MT) method is increasingly used in modern geophysical explorations. As with the DCR method, MT reveals the subsurface structures in terms of the spatial variation of the resistivity. MT is a passive-source method utilizing natural occurring electromagnetic (EM) waves as a source. The induced time-varying electric and magnetic fields are collected at the surface as time-series data. The acquired data is then transformed into the “apparent resistivity” and “phase” as a function of frequency domain.

The radiomagnetotelluric (RMT) method uses a very high frequency, between 10 Hz – 500 kHz, as a source for shallow studies (approximately 5 m to 50 m), e.g. in environmental applications (Pedersen *et al.*, 2005; Tezkan, 1999; Tezkan *et al.*, 2005). The audiomagnetotelluric (AMT) method utilizes frequencies from 10 Hz – 10 kHz to map structures that are deeper than can be detected by RMT, for example, in ore mineral (Tuncer *et al.*, 2006; Farquharson & Craven, 2009) and hydrocarbon (Constable *et al.*, 1998; Mitsuhashi *et al.*, 1999) exploration. The lower frequency MT is commonly applied for tectonic and crustal studies (Ingham & Brown, 1998; Ogawa *et al.*, 1998).

### 2.3.1 Principle of magnetotelluric method

MT sources can be categorized into two groups according to their frequency. The first group is the interaction between the solar wind and the ionosphere generating frequencies less of than 1 Hz. The other group is the phenomena in the atmosphere such as lightning which generate high frequency EM waves. When these EM waves travel as in a waveguide between the Earth surface and the ionosphere, the EM waves are assumed to be plane waves relative to the size of the survey area. The EM waves penetrate vertically downwards into the Earth subsurface and produce an electromagnetic induction within the Earth.

Different frequencies are reflected by the subsurface variation at different depths. The investigation depth of the MT survey can be adequately inferred from the “skin depth” which is defined as the length in which an EM wave decays by a factor of  $1/e$ ,

$$\text{skin depth} = \sqrt{\frac{2\rho}{\omega\mu}}. \quad (2.14)$$

The magnetic permeability of the earth subsurface  $\mu$  is assumed to be equal to that of free space  $\mu_0$ .  $\rho$  is the resistivity of an assumed homogeneous halfspace.  $\omega$  is the angular frequency  $\omega = 2\pi f$ . For simplicity and ease of use, equation (2.14) is simplified to

$$\text{skin depth} = 503\sqrt{\rho T}, \quad (2.15)$$

where  $T$  is the period of the EM wave,  $T = 1/f$ . Note that the unit of skin depth in equation (2.15) is meter.

### 2.3.2 Field measurement

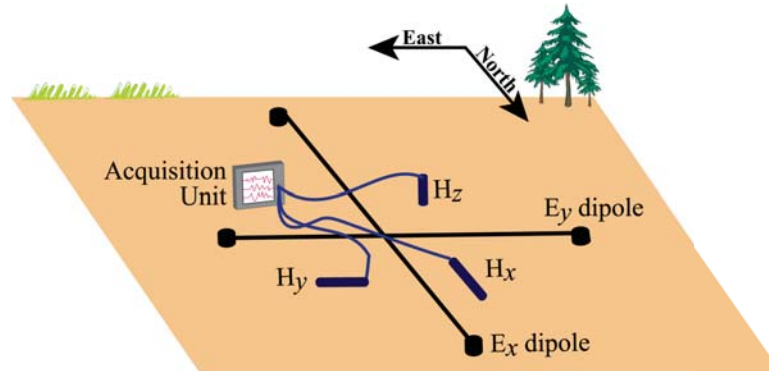


Figure 2.8: A typical configuration of a single MT station

Figure 2.8 illustrates the typical configuration of a single MT station which consist of the following important instruments:

- The “acquisition unit” is an analog–digital (A/D) converter used for acquiring and storing the time-varying electric and magnetic fields.
- The “electric dipoles” are used to record the time-varying electric field components,  $E_x$  and  $E_y$ . The electric dipoles in one direction consist of two electrodes buried in opposing directions at the desired distance. The potential difference is then used to calculate the electric field in that direction.
- The “magnetometer” is used to record the time-varying magnetic field of all the components,  $H_x$ ,  $H_y$  and  $H_z$ . The magnetometer in each direction is aligned parallel to that direction and buried at the desired position far enough from the acquisition unit and the connecting wires to avoid noise.

Figure 2.9 shows the acquired time series of the electric and magnetic fields. The time domain electric  $\mathbf{E}(t)$  and magnetic  $\mathbf{H}(t)$  fields are then transformed into the frequency domain  $\mathbf{E}(\omega)$  and  $\mathbf{H}(\omega)$  using the Fourier transform.

The impedance tensor  $\mathbf{Z}$  is expressed as the relation between  $\mathbf{E}(\omega)$  and  $\mathbf{H}(\omega)$ :

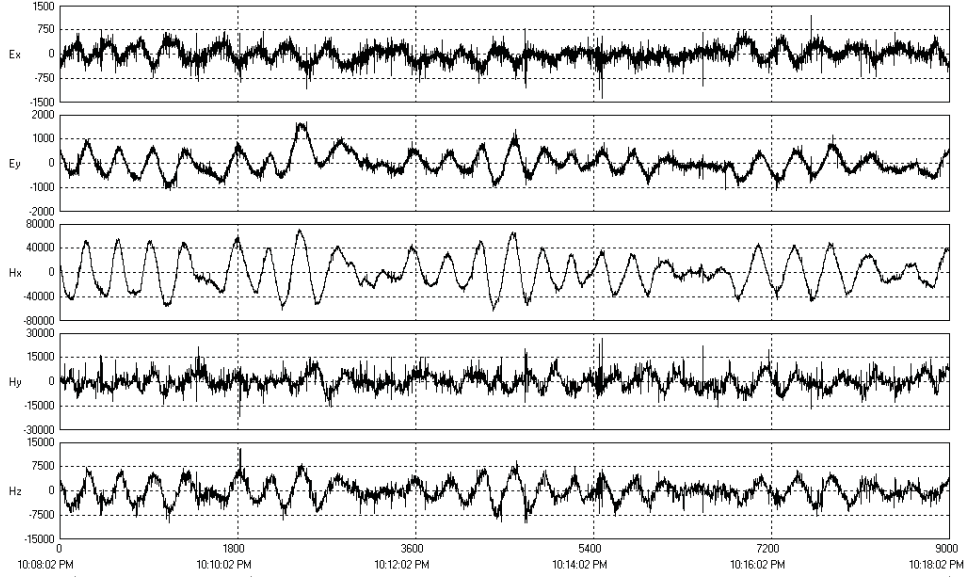


Figure 2.9: The acquired components of the time varying electric and magnetic fields

$$\mathbf{E}(\omega) = \mathbf{Z}(\omega)\mathbf{H}(\omega). \quad (2.16)$$

or

$$\begin{pmatrix} E_x \\ E_y \end{pmatrix} = \begin{pmatrix} Z_{xx} & Z_{xy} \\ Z_{yx} & Z_{yy} \end{pmatrix} \begin{pmatrix} H_x \\ H_y \end{pmatrix} \quad (2.17)$$

The elements of the impedance tensor can be used to indicate the dimensionality of the subsurface (see also section 1.1.2). For a 1-D Earth,  $\rho = \rho(z)$ ,

$$\begin{aligned} Z_{xx} &= Z_{yy} = 0, \\ Z_{xy} &= -Z_{yx}. \end{aligned} \quad (2.18)$$

For a 2-D Earth,  $\rho = \rho(y, z)$ , where  $x$  is an assumed strike direction, elements of the impedance tensor are then

$$\begin{aligned} Z_{xx} &= -Z_{yy}, \\ Z_{xy} &\neq -Z_{yx}. \end{aligned} \quad (2.19)$$

For a real 3-D Earth, all elements of the impedance tensor behave individually and so

$$\begin{aligned} Z_{xx} &\neq -Z_{yy}, \\ Z_{xy} &\neq -Z_{yx}. \end{aligned} \quad (2.20)$$

### 2.3.3 Data responses and interpretation

The impedance tensor is transformed into the ‘‘apparent resistivity’’ and ‘‘phase’’ for many frequencies via

$$\rho_{ij} = \frac{1}{\omega\mu_0} |Z_{ij}|^2, \quad (2.21)$$

and

$$\phi_{ij} = \tan^{-1} \left( \frac{\Im(Z_{ij})}{\Re(Z_{ij})} \right). \tag{2.22}$$

$i$  and  $j$  in equation (2.21) and (2.22) can be either  $x$  or  $y$ .

A plot of  $\rho_a$  and  $\phi$  indicates the resistivity structure as a function of depth (Figure 2.10). A lower frequency or longer period senses a deeper structure while a higher frequency senses a shallow structure.

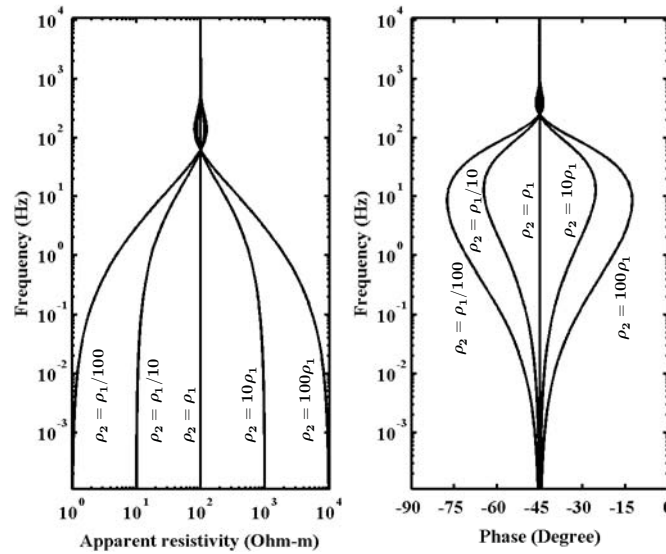
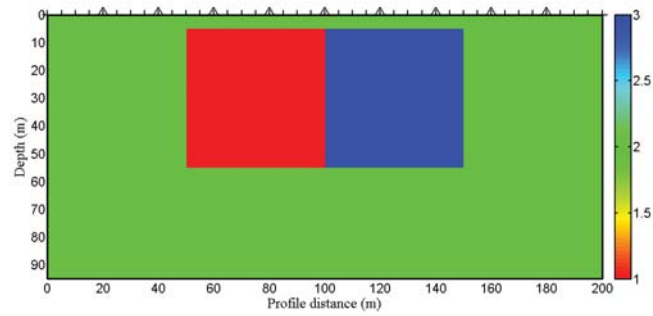


Figure 2.10: MT sounding curve. (a) Apparent resistivity and (b) phase are plotted as a function of frequency from a two layers model with various values of resistivity of the second layer.

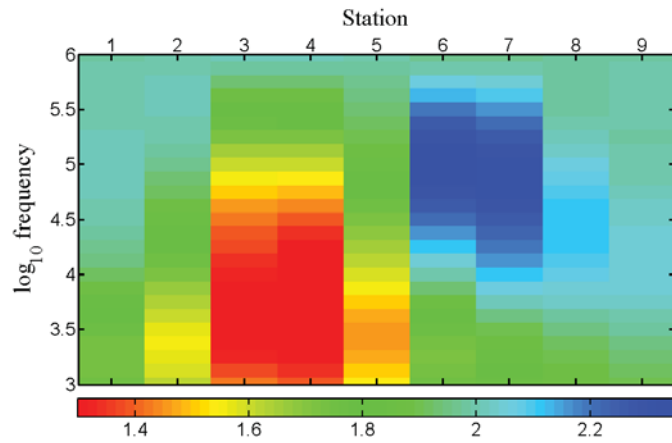
### MT Pseudosection

A single MT station gives the resistivity variation with depth beneath the station location. To obtain a 2-D resistivity variation, many of the MT stations are placed at different locations in the 2-D profile as demonstrated in Figure 2.11a.

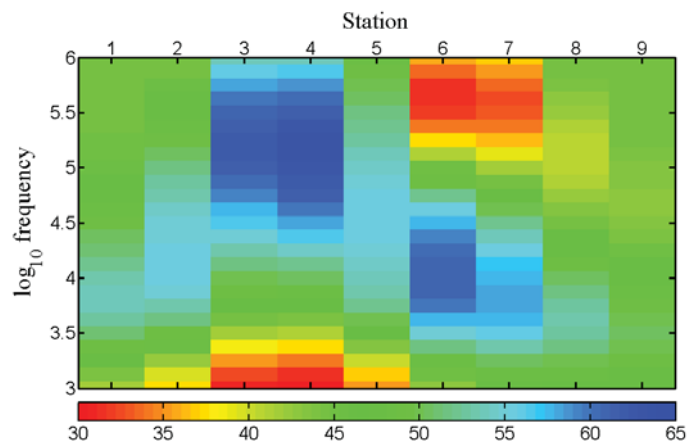
Figure 2.11b and 2.11c are the pseudosection of apparent resistivity and phase generated from Figure 2.11a. The MT method is superior to the DCR method in which MT has phase as an additional response. Phase exhibits a different characteristic from apparent resistivity which helps with constraining the interpretation. However, the direct interpretation from MT pseudosections requires experience. In order to obtain the true resistivity variation of the subsurface, 2-D inversion is needed.



(a) Synthetic model used to generate the responses. MT stations are denoted by triangle markers at the surface.



(b) Pseudosection of apparent resistivity. The color represents the  $\log_{10}$  of the apparent resistivity.



(c) Pseudosection of phase. The color represents the phase in degrees.

Figure 2.11: (a) is the pseudosection of 9 MT stations with spacing of 20 m generated from synthetic model. (b) is an apparent resistivity pseudosection. (c) is a phase pseudosection.

## CHAPTER III

### INVERSION ALGORITHM

#### 3.1 Geophysical inversion

“Inversion” is basically a mathematical optimization which finds the solution that fits the collected data and obeys the additional constraints made on the problem’s characteristics.

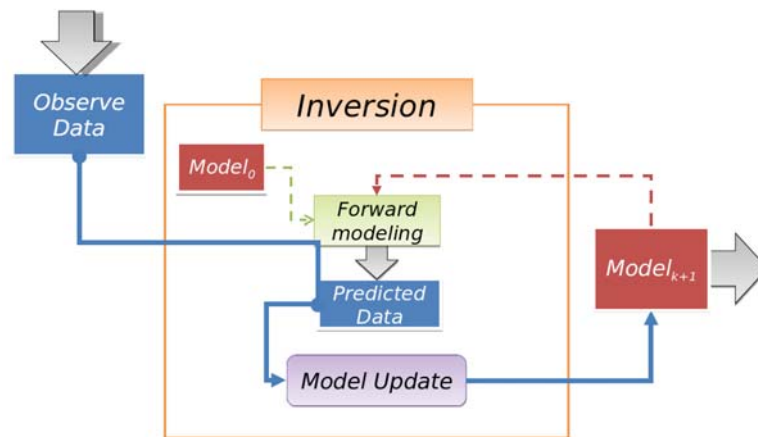


Figure 3.1: The diagram shows the basic idea of the general inversion.

In general, as illustrated in Figure 3.1, the inversion process begins with an appropriate starting model ( $\mathbf{m}_0$ ). The predicted data is then generated using forward modeling. After comparing the calculated data response with the measurement data, the difference determines the changes of the model for the next iteration ( $\mathbf{m}_{k+1}$ ). The process iterates until a model is obtained that has the predicted response fit to the measurement data within an acceptable level.

In geophysical problems, many inversion algorithms have been utilized such as Gauss-Newton (Degroot-Hedlin & Constable, 1990; Gunther *et al.*, 2006), quasi-Newton (QN) (Loke & Barker, 1996; Avdeev & Avdeeva, 2009), conjugate gradient (CG) (Ellis & Oldenburg, 1994; Zhang *et al.*, 1995), non-linear conjugate gradient (NLCG) (Rodi & Mackie, 2001), genetic algorithm (Schwarzbach *et al.*, 2005) and hybrid algorithms (Chunduru *et al.*, 1997).

Gauss-Newton (GN) and its variant methods is one of the successful inversion algorithms. Significant advantages of GN are the stability and robustness which guarantee the convergence to the solution (Boonchaisuk *et al.*, 2008). On the other hand, the direct approach GN-type inversion consumes large amounts of both computational time and memory due to the large matrices calculations. A further algorithm such as QN-type inversion reduces the memory usage by using an approximation. CG and NLCG are other approaches that use less computational time and less memory by avoiding the large matrices calculation. However, the stability and the convergence rate of QN, CG and NLCG may be questionable in some cases. Stochastic approaches such as genetic algorithms are of increasing interest. Nevertheless, because of the huge computational costs, stochastic inversions are mostly impractical and still in development (Schwarzbach *et al.*, 2005).

Due to stability and robustness, Occam's inversion which is a variant of the GN-type inversion will be used here. Occam's algorithm was developed based on the philosophy of the simple and smooth solution. An implemented data-space variant of Occam's inversion reduces the large memory usage and computational time. Therefore, its computational efficiencies are comparable to those of QN, CG and NLCG, but with a better convergence. This algorithm has been widely used and proven to be one of the efficient inversions (Degroot-Hedlin & Constable, 1990; Siripunvaraporn & Egbert, 2000; Siripunvaraporn *et al.*, 2005; Boonchaisuk *et al.*, 2008).

In this chapter, Occam's inversion and its data-space variant will be explained. Our implemented 2-D joint inversion of DCR and MT will then be described.

### 3.2 Occam's inversion

Occam's inversion was proposed by Constable *et al.* (1987) for 1-D MT and 1-D schlumberger DCR. The philosophy of the Occam approach is to seek the "smoothest" or "minimum" structure model subject to a constraint on the misfit (see Constable *et al.*, 1987; Siripunvaraporn & Egbert, 2000; Boonchaisuk *et al.*, 2008), which can be mathematically transformed into a problem of minimization of an objective function  $W$ ,

$$W = \Phi_m + \lambda^{-1}\Phi_d. \quad (3.1)$$

$\Phi_m$  denotes the "model function".  $\Phi_d$  represents the "data functional". Here, we want to minimize  $\Phi_m$  subject to  $\Phi_d = 0$ .  $\lambda$  is introduced as the Lagrange multiplier acting as the regularization or trade-off parameter between the model and data functionals.

### 3.2.1 Data functional

The data functional is defined as  $\Phi_d = \chi_d^2 - \chi_{d*}^2$ , when  $\chi_d^2$  is the “data misfit” which represents how the generated response from the solution fits the observed data, and  $\chi_{d*}^2$  is the desired data misfit. When the data misfit  $\chi_d^2$  is reduced to the desired misfit  $\chi_{d*}^2$ , the data functional  $\Phi_d = 0$ .

As with the least-square problem,  $\chi_d^2$  represents an average variance between the measured data ( $d$ ) and the numerically predicted data ( $f$ ) which can be expressed by

$$\chi_d^2 = \sum_{i=1}^N \left( \frac{d_i - f_i}{\epsilon_i} \right)^2, \quad (3.2)$$

where  $\epsilon_i$  is the error of the measured data  $d_i$  and  $N$  is the number of data.

Equation (3.2) can be expressed in matrix form as,

$$\chi_d^2 = (\mathbf{d} - \mathbf{F}[\mathbf{m}])^T \mathbf{C}_d^{-1} (\mathbf{d} - \mathbf{F}[\mathbf{m}]), \quad (3.3)$$

where  $\mathbf{d}$  is a vector containing the measured data.  $\mathbf{F}[\mathbf{m}]$  is a vector containing the predicted data generated by the forward modeling from the model vector  $\mathbf{m}$  ( $\mathbf{F}$  represents the forward modeling operator),

$$\mathbf{F}[\mathbf{m}] = \begin{pmatrix} f_1 \\ f_2 \\ f_3 \\ \vdots \\ f_N \end{pmatrix}_{N \times 1}. \quad (3.4)$$

In 2-D cases the model is discretized into blocks as shown in Figure 3.2.

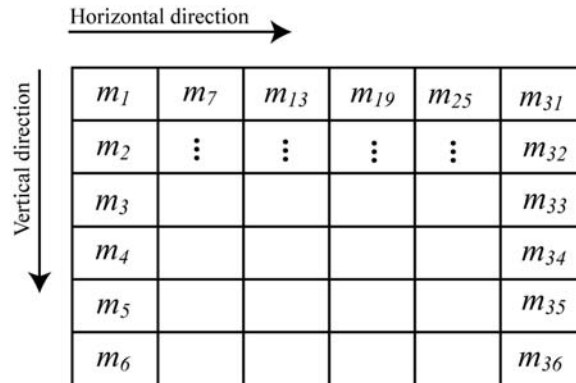


Figure 3.2: 2-D model discretization.

Model parameters are then ordered into a vector by column from top to

bottom elements,

$$\mathbf{m} = \begin{pmatrix} m_1 \\ m_2 \\ m_3 \\ \vdots \\ m_M \end{pmatrix}_{M \times 1}, \quad (3.5)$$

where  $M$  is the number of model parameters which is equal to the total number of discretized model blocks.

The inverse data covariance matrix  $\mathbf{C}_d^{-1}$  can be expressed as

$$\mathbf{C}_d^{-1} = \mathbf{W}_d^T \mathbf{W}_d \quad (3.6)$$

where

$$\mathbf{W}_d = \begin{pmatrix} 1/\epsilon_1 & & & & \\ & 1/\epsilon_2 & & & \\ & & 1/\epsilon_3 & & \\ & & & \ddots & \\ & & & & 1/\epsilon_N \end{pmatrix}_{N \times N}. \quad (3.7)$$

### 3.2.2 Model functional

The model functional ( $\Phi_m$ ) is the additional condition that constrains the inversion to obtain the solution according to the geological aspects of the model such as the smoothness constraint (Degroot-Hedlin & Constable, 1990; Siripunvaraporn & Egbert, 2000; Boonchaisuk *et al.*, 2008), sharp boundary condition (Degroot-Hedlin & Constable, 2004) and constraint from the known geological features (Auken & Christiansen, 2004).

Here, for Occam's inversion, the smoothness constraint is assumed according to the philosophy of minimum structure. The model functional  $\Phi_m$  is then estimated by the smoothness of the model represented by the "model norm" ( $\chi_m^2$ ) and is defined as an average variance of the model parameter between the consecutive discretized blocks.  $\chi_m^2$  can be expressed by

$$\chi_m^2 = \sum_{i=1}^M (m_{i+1} - m_i). \quad (3.8)$$

Equation (3.8) can be written in matrix form as,

$$\chi_m^2 = (\mathbf{m} - \mathbf{m}_0)^T \mathbf{C}_m^{-1} (\mathbf{m} - \mathbf{m}_0). \quad (3.9)$$

where  $\mathbf{m}_0$  is the reference prior model,  $\mathbf{C}_m$  is the model covariance.

The model roughness or the inverse of the model covariance ( $\mathbf{C}_m^{-1}$ ) operator is introduced in Degroot-Hedlin & Constable (1990) as,

$$\mathbf{C}_m^{-1} = \Delta_x^T \Delta_x + \Delta_z^T \Delta_z, \quad (3.10)$$

where  $\Delta_x$  and  $\Delta_z$  are the horizontal and vertical roughening matrices which operate on a 2-D model with an assumed  $y$  strike direction.

For an example of a 2-D model consisting of  $M_x$  elements in the  $x$  direction,  $M_z$  elements in  $z$  direction and  $M = M_x \times M_z$ ,  $\Delta_x$  and  $\Delta_z$  can be expressed as

$$\Delta_x = \begin{pmatrix} -1 & \dots & 1 & \dots \\ & -1 & & 1 & \dots \\ & & \ddots & & \ddots \\ \dots & & & -1 & \dots & 1 \\ & & & \mathbf{0} & & \end{pmatrix}_{M \times M}, \quad (3.11)$$

where  $\mathbf{0}$  is an  $M_z \times M$  zero matrix. There are  $M_z - 1$  zeros between the entries in each row of  $\Delta_x$  (according to the indexes of the consecutive horizontal elements).

$$\Delta_z = \begin{pmatrix} \Delta_1 & & & \\ & \Delta_2 & & \\ & & \ddots & \\ & & & \Delta_{M_z} \end{pmatrix}_{M \times M}, \quad (3.12)$$

where  $\Delta_i$  is the  $M_x \times M_x$  vertical roughening sub-matrix for the column of grid  $i$ ,

$$\Delta_i = \begin{pmatrix} 0 & & & & \\ -1 & 1 & & & \\ & -1 & 1 & & \\ & & \ddots & \ddots & \\ & & & -1 & 1 \end{pmatrix}_{M_x \times M_x} \quad (3.13)$$

### 3.2.3 Minimization of an objective function

For Occam's inversion, the objective function (3.1) can be expressed according to the given data functional (3.3) and model functional (3.9) as

$$W(\lambda, \mathbf{m}) = (\mathbf{m} - \mathbf{m}_0)^T \mathbf{C}_m^{-1} (\mathbf{m} - \mathbf{m}_0) + \lambda^{-1} \left[ (\mathbf{d} - \mathbf{F}[\mathbf{m}])^T \mathbf{C}_d^{-1} (\mathbf{d} - \mathbf{F}[\mathbf{m}]) - \chi_{d*}^2 \right] \quad (3.14)$$

where  $\chi_{d*}^2$  is the desired level of misfit.

Because this inverse problem is nonlinear, we therefore apply the perturbation  $\Delta \mathbf{m}$  to the model  $\mathbf{m}$  in order to form the iteration of the minimization process. We use a Taylor's series expansion to linearize  $\mathbf{F}[\mathbf{m}]$ ,

$$\mathbf{F}[\mathbf{m} + \Delta \mathbf{m}] = \mathbf{F}[\mathbf{m}] + \frac{\partial \mathbf{F}[\mathbf{m}]}{\partial \mathbf{m}} \Delta \mathbf{m}. \quad (3.15)$$

Since  $\mathbf{m}_{k+1} = \mathbf{m}_k + \Delta \mathbf{m}$ , equation (3.15) can be written in iterated form,

$$\mathbf{F}[\mathbf{m}_{k+1}] = \mathbf{F}[\mathbf{m}_k] + \mathbf{J}_k (\mathbf{m}_{k+1} - \mathbf{m}_k), \quad (3.16)$$

where  $k$  denotes the iteration number,  $\mathbf{m}_{k+1}$  represents the model at the next iteration, and the first derivative  $\mathbf{J}_k$  is the Jacobian or sensitivity calculated at iteration  $k$  and

$$\mathbf{J}_k \equiv \frac{\partial \mathbf{F}[\mathbf{m}_k]}{\partial \mathbf{m}}.$$

Substituting equation (3.16) into (3.14), the objective function can now be expressed in the iterative form,

$$\begin{aligned} W_\lambda = & (\mathbf{m}_{k+1} - \mathbf{m}_0)^T \mathbf{C}_m^{-1} (\mathbf{m}_{k+1} - \mathbf{m}_0) \\ & + \lambda^{-1} [(\mathbf{d} - \mathbf{F}[\mathbf{m}_k] + \mathbf{J}_k(\mathbf{m}_{k+1} - \mathbf{m}_k)) \mathbf{C}_d^{-1} (\mathbf{d} - \mathbf{F}[\mathbf{m}_k] + \mathbf{J}_k(\mathbf{m}_{k+1} - \mathbf{m}_k)) - \chi_{d*}^2] \end{aligned} \quad (3.17)$$

To incorporate the prior model  $\mathbf{m}_0$  into the inversion, we replace

$$\mathbf{m}_{k+1} - \mathbf{m}_k = (\mathbf{m}_{k+1} - \mathbf{m}_0) - (\mathbf{m}_k - \mathbf{m}_0)$$

and substitute into equation (3.17). The objective function becomes

$$\begin{aligned} W_\lambda = & (\mathbf{m}_{k+1} - \mathbf{m}_0)^T \mathbf{C}_m^{-1} (\mathbf{m}_{k+1} - \mathbf{m}_0) \\ & + \lambda^{-1} \left[ \left( \hat{\mathbf{d}} - \mathbf{J}_k(\mathbf{m}_{k+1} - \mathbf{m}_0) \right)^T \mathbf{C}_d^{-1} \left( \hat{\mathbf{d}} - \mathbf{J}_k(\mathbf{m}_{k+1} - \mathbf{m}_0) \right) - \chi_{d*}^2 \right] \end{aligned} \quad (3.18)$$

where  $\hat{\mathbf{d}} = \mathbf{d} - \mathbf{F}[\mathbf{m}_k] + \mathbf{J}_k(\mathbf{m}_k - \mathbf{m}_0)$ .

In order to find the  $\mathbf{m}_{k+1}$  that minimizes the objective function, we differentiate equation (3.18) with respect to  $\mathbf{m}_{k+1}$  at the stationary point,

$$\frac{\partial W_\lambda}{\partial \mathbf{m}_{k+1}} = 0. \quad (3.19)$$

Hence, the expression of the iterative sequence is (see Vachiratienchai, 2007; Boonchaisuk, 2007)

$$\mathbf{m}_{k+1} = (\lambda \mathbf{C}_m^{-1} + \mathbf{\Gamma}_k^m)^{-1} \mathbf{J}_k^T \mathbf{C}_d^{-1} \hat{\mathbf{d}} + \mathbf{m}_0, \quad (3.20)$$

where  $\mathbf{\Gamma}_k^m = \mathbf{J}_k^T \mathbf{C}_d^{-1} \mathbf{J}_k$ , The model cross-product matrix  $\mathbf{\Gamma}_k^m$  is an  $M \times M$  positive semidefinite symmetric matrix. This direct approach is known as the ‘‘model space’’ Occam’s inversion.

### 3.3 Data-space Occam’s inversion

Parker (1994) shows that the solution of equation (3.20) can be expressed as a linear combination of rows of the smoothed sensitivity matrix  $\mathbf{C}_m \mathbf{J}_k^T$ ,

$$\mathbf{m}_{k+1} - \mathbf{m}_0 = \mathbf{C}_m \mathbf{J}_k^T \boldsymbol{\beta}_{k+1}, \quad (3.21)$$

where  $\boldsymbol{\beta}_{k+1}$  is an unknown expansion coefficient vector. Siripunvaraporn and Egbert (2000) apply this approach with their 2-D MT inversion by rearranging equation (3.20)

(see Siripunvaraporn & Egbert, 2000; Vachiratiengchai, 2007; Boonchaisuk, 2007). We obtain

$$\begin{aligned}\mathbf{m}_{k+1} &= [\lambda \mathbf{C}_m^{-1} + \mathbf{J}_k^T \mathbf{C}_d^{-1} \mathbf{J}_k]^{-1} \mathbf{J}_k^T \mathbf{C}_d^{-1} \hat{\mathbf{d}} + \mathbf{m}_0 \\ &= \mathbf{C}_m \mathbf{J}_k^T [\lambda \mathbf{C}_d + \mathbf{J}_k \mathbf{C}_m \mathbf{J}_k^T]^{-1} \hat{\mathbf{d}} + \mathbf{m}_0\end{aligned}\quad (3.22)$$

Hence, the transformed expression of the iterative sequence (3.20) is

$$\mathbf{m}_{k+1} = \mathbf{C}_m \mathbf{J}_k^T \boldsymbol{\beta}_{k+1} + \mathbf{m}_0. \quad (3.23)$$

$\boldsymbol{\beta}_{k+1}$  represents a basis function,

$$\boldsymbol{\beta}_{k+1} = [\lambda \mathbf{C}_d + \boldsymbol{\Gamma}_k^n]^{-1} \hat{\mathbf{d}} \quad (3.24)$$

where  $\boldsymbol{\Gamma}_k^n = \mathbf{J}_k \mathbf{C}_m \mathbf{J}_k^T$ , the “data” cross-product matrix  $\boldsymbol{\Gamma}_k^n$  is an  $N \times N$  positive semidefinite symmetric matrix. This approach is referred as the “data space” Occam’s inversion (Siripunvaraporn & Egbert, 2000).  $\mathbf{C}_m$  is impractical to construct from the inverse of equation (3.10) due to the singularity. In this case, a new  $\mathbf{C}_m$  is needed but is not directly constructed. We require  $\mathbf{C}_m \mathbf{J}_k^T$  instead. The calculation of  $\mathbf{C}_m \mathbf{J}_k^T$  will be described in the next section.

The system of model space (3.20) and data space (3.23) differs in the matter of the computational domain. The  $M \times M$  model cross-product matrix  $\boldsymbol{\Gamma}_k^m$  is reduced to a  $N \times N$  data cross-product matrix  $\boldsymbol{\Gamma}_k^n$ . Both the model space approach (equation (3.20)) and data space approach (equation (3.23)) yield identical solutions if all the parameters used are the same.

In geophysical problems, especially DCR and MT, the number of model parameters  $M$  is usually much larger than the number of data  $N$ . Transformation to the data space significantly reduces both the computational time and the memory usage (Siripunvaraporn & Egbert, 2000; Siripunvaraporn *et al.*, 2005; Boonchaisuk *et al.*, 2008).

Occam’s inversion has a method of minimization which differs from other regularized inversion algorithms. In the model space and data space approach, the inversion is divided into 2 phases. The first phase (Phase I) is designed to minimize the misfit down to the desired level  $\chi_{d*}^2$  by varying  $\lambda$  in equation (3.20) and (3.23) at each iteration. Once the target misfit is reached, Phase II searches for the minimum model norm by varying  $\lambda$  while keeping the misfit at the desired level. Phase II guarantees that the model will not contain any spurious structures (Siripunvaraporn *et al.*, 2004, 2005). Here, we apply this data space Occam’s inversion to the 2-D joint inversion of DCR and MT. Algorithm 1 illustrates an overview of the data space Occam’s inversion algorithm.

---

**Algorithm 1** Data space Occam's inversion
 

---

Assign  $\mathbf{d}$  and  $\mathbf{C}_d$

Assign  $\mathbf{m}_0$

Assign  $\mathbf{m}_{k+1} = \mathbf{m}_k$

**while**  $\chi_d^2(\mathbf{m}_{k+1}) \notin [\chi_{d^*}^2 - \varepsilon, \chi_{d^*}^2 + \varepsilon]$  **do**

(Phase I)

Form  $\mathbf{J}_k$ ,  $\mathbf{C}_m \mathbf{J}_k^T$ ,  $\mathbf{\Gamma}_k^n$  and  $\hat{\mathbf{d}}$

**while** Minimizing  $\chi_d^2(\mathbf{m}_{\lambda_k})$  **do**

Solve  $\beta_{k+1} = [\lambda_k \mathbf{C}_d + \mathbf{\Gamma}_k^m]^{-1}$

Calculate  $\Delta \mathbf{m}_{\lambda_k} = \mathbf{C}_m \mathbf{J}_k^T \beta_{k+1}$

Update  $\mathbf{m}_{\lambda_{k+1}} = \Delta \mathbf{m}_{\lambda_k} + \mathbf{m}_0$

**end while**

Assign  $\mathbf{m}_{k+1} = \mathbf{m}_{\lambda_{k+1}}$

Calculate  $\chi_d^2(\mathbf{m}_{k+1})$

**end while**

(Phase II)

**while**  $\chi_m^2(\mathbf{m}_{k+1}) < \chi_m^2(\mathbf{m}_k)$  **do**

Form  $\mathbf{J}_k$ ,  $\mathbf{C}_m \mathbf{J}_k^T$ ,  $\mathbf{\Gamma}_k^n$  and  $\hat{\mathbf{d}}$

Calculate  $\chi_m^2(\mathbf{m}_k)$

**while** Minimizing  $\chi_m^2(\mathbf{m}_{\lambda_k})$  remaining  $\chi_d^2(\mathbf{m}_{k+1}) \in [\chi_{d^*}^2 - \varepsilon, \chi_{d^*}^2 + \varepsilon]$  **do**

Solve  $\beta_{k+1} = [\lambda_k \mathbf{C}_d + \mathbf{\Gamma}_k^m]^{-1}$

Calculate  $\Delta \mathbf{m}_{\lambda_k} = \mathbf{C}_m \mathbf{J}_k^T \beta_{k+1}$

Update  $\mathbf{m}_{\lambda_{k+1}} = \Delta \mathbf{m}_{\lambda_k} + \mathbf{m}_0$

**end while**

Assign  $\mathbf{m}_{k+1} = \mathbf{m}_{\lambda_{k+1}}$

Calculate  $\chi_m^2(\mathbf{m}_{k+1})$

**end while**

---

### 3.4 Previous implementations of joint inversion of DCR & MT

The joint inversion is commonly treated as the combined inversion of two separate methods replacing the single data vector and the sensitivity matrix with the combined one. In addition, the sensitivity of each data set can be weighted in the combined inversion by replacing  $\mathbf{J}_k$  with  $\mathbf{W}_T \mathbf{J}_k$ , where  $\mathbf{W}_T$  is a diagonal matrix referred to the weighting matrix for each data set.

Previous work on a joint inversion of DCR and MT were done mostly on 1-D surveys or sounding (Vozoff & Jupp, 1975; Jupp & Vozoff, 1977; Raiche *et al.*, 1985; Harinarayana, 1999). There are a few 2-D joint inversion available in the literature (Sasaki, 1989; Candansayar, 2008).

Sasaki (1989) proposed the first 2-D joint inversion based on the smoothness-constrained least-squares algorithm (Lytle & Dines, 1980). The iterative solution can be expressed as (see Sasaki, 1989)

$$\left( \mathbf{J}_k^T \mathbf{J}_k + \lambda \mathbf{C}_m^{-1T} \mathbf{C}_m^{-1} \right)_{M \times M} \Delta \mathbf{m} = \mathbf{J}_k^T \Delta \mathbf{d}_k, \quad (3.25)$$

where  $\Delta \mathbf{d}_k = \mathbf{d} - \mathbf{F}[\mathbf{m}_k]$ . The system in equation (3.25) is  $M \times M$  in dimension and solved with the modified Gram-Schmidt method (Bjoerck, 1967). The regularized parameter  $\lambda$  is fixed throughout the inversion because it is impractical to randomly solve equation (3.25) many times at each iteration. The data weighting is set equally ( $\mathbf{W}_T = \mathbf{I}$ ) for all the data in the case of both DCR and AMT. The obtained model from the joint inversion improves the model resolution. This algorithm was also applied to field explorations e.g. Monteiro Santos *et al.* (2007).

Candansayar (2008) later proposed a new 2-D joint inversion algorithm for DCR and RMT based on the rectangular system (Haber & Oldenburg, 2000) which is a variant of the smoothness-constrained least-squares algorithm. The iterative solution can be expressed by (see Candansayar, 2008)

$$\tilde{\mathbf{J}}_k \Delta \mathbf{m} = \Delta \tilde{\mathbf{d}}_k, \quad (3.26)$$

where

$$\tilde{\mathbf{J}}_k = \begin{pmatrix} \mathbf{C}_d^{-1} \mathbf{J}_k \\ \sqrt{\lambda} \mathbf{C}_m^{-1} \end{pmatrix}_{(N+M) \times M},$$

and

$$\tilde{\mathbf{d}}_k = \begin{pmatrix} \mathbf{C}_d^{-1} \Delta \mathbf{d}_k \\ \sqrt{\lambda} \mathbf{C}_m^{-1} \mathbf{m}_k \end{pmatrix}_{(N+M) \times M}.$$

Equation (3.26) is a  $(N + M) \times M$  system which is larger than that in equation (3.25). However, he claimed a faster calculation time when using QR factorization. In this algorithm, the weighting matrix ( $\mathbf{W}_T$ ) plays an important role which is predetermined

according to the investigation depth of each method. The diagonal elements of  $\mathbf{W}_T$  vary from 0 – 1 according to the desired weighting of each data.  $\mathbf{W}_T$  is fixed throughout the inversion.

Here, we propose to develop an efficient 2-D joint inversion of DCR and MT data based on the data space Occam’s inversion (DASOCC) algorithm. With the DASOCC algorithm, the computational time and memory usage would be significantly reduced. This can be inferred from the fact that equation (3.23) is smaller than the system of equation (3.25) and (3.26), i.e.  $N \times N$  is smaller than  $M \times M$  and  $(M+N) \times M$ .

### 3.5 Implementation to 2-D joint inversion of DCR & MT

Our goal is to gain the usage of the integrated DCR and MT methods in the field by providing an efficient joint inversion for 2-D DCR and MT data. Our major implementation includes the data combining routines, 2-D forward modeling, sensitivity calculation and the model covariance. All routines have been implemented from Siripunvaraporn & Egbert (2000) and Vachiratienchai (2007) previously written in FORTRAN 77 and MATLAB, respectively, to FORTRAN 95/2003.

#### 3.5.1 Data functional

For the data functional, the data vector  $\mathbf{d}$  is implemented as the combination of the data from DCR and MT,

$$\mathbf{d} = \begin{pmatrix} \mathbf{d}_{DCR} \\ \mathbf{d}_{MT} \end{pmatrix}_{N_T \times 1}, \quad (3.27)$$

where the number of data is  $N_T = N_{DCR} + N_{MT}$ . Similarly,

$$\mathbf{F}[\mathbf{m}] = \begin{pmatrix} \mathbf{f}_{DCR} \\ \mathbf{f}_{MT} \end{pmatrix}_{N_T \times 1}, \quad (3.28)$$

can be separately calculated from the DCR and MT forward modeling routines, respectively, and then combined into a single vector.

#### 3.5.2 Forward modeling

Forward modeling is an essential part of the inversion. Numerous calls of the forward modeling in an inversion are associated with the computation for the response and the sensitivity calculation. Therefore, the forward modeling must be fast, accurate and reliable. In this thesis, we use the 2-D DCR forward modeling developed by Vachiratienchai (2007) and the 2-D MT forward modeling developed by Siripunvaraporn & Egbert (2000). A brief description of both is given here.

## DCR forward modeling

There are a number of efficient 2-D forward modeling techniques available. Many techniques, e.g. the transmission surface, finite difference and finite element methods are used to solve the electrical potential distribution in Fourier space which is expressed in the form of the Helmholtz equation (see also Vachiratienchai, 2007; Boonchaisuk, 2007),

$$\nabla \cdot \left[ \sigma(x, z) \nabla \tilde{\phi}(x, k_y, z) \right] + k_y^2 \sigma(x, z) \tilde{\phi}(x, k_y, z) = \frac{I}{2} \delta(x_s) \delta(z_s). \quad (3.29)$$

Since the resistivity distribution is 2-D and the  $y$  direction is the assumed strike direction, equation (3.29) is solved in Fourier space  $(x, k_y, z)$  instead of  $(x, y, z)$  where  $k_y$  is the wave number. In order to solve the potential distribution  $\tilde{\phi}(x, k_y, z)$  associated with an injecting current  $I$ , we use the existing 2-D DCR forward modeling from Vachiratienchai (2007) which is implemented with the finite difference (FD) method using mixed boundary conditions (Dey & Morrison, 1979). The main advantages of the FD method is its speed and easy implementation (see also Dey & Morrison, 1979; Vachiratienchai, 2007; Boonchaisuk *et al.*, 2008). After the FD approximation, equation (3.29) can be expressed in matrix form as

$$\mathbf{S}_m \tilde{\phi} = \mathbf{b}, \quad (3.30)$$

where  $\mathbf{S}_m$  is a 5-band sparse matrix of a 2-D FD discretization which depends on the model discretization and wave number,  $\mathbf{b}$  is the imposed boundary conditions and the source term. For each wavenumber  $k_y$ , the solution  $\tilde{\phi}$  is best solved by Cholesky decomposition.

To obtain the potential  $\phi$  in  $(x, y, z)$  space, the discrete inverse Fourier transform (iDFT),

$$\phi(x, y, z) \approx \sum_{p=1}^{n_{k_y}} \tilde{\phi}(x, k_{y_p}, z) g_p, \quad (3.31)$$

is applied. For an accurate result, the iDFT requires the appropriate number of  $k_{y_p}$  and its corresponding weight  $g_p$ . Xu *et al.* (2000) provides a good review of the optimization of the wave number showing that at least four of wave numbers  $k_y$  are sufficient to produce an accurate iDFT. However, to produce a more accurate result, the number of  $k_y$  should be increased.

Once the iDFT is applied, the electrical potential in  $(x, y, z)$  space is obtained. The data response, an apparent resistivity  $\rho_a$ , can then be calculated using the given equation (2.13).

The 2-D forward modeling is formed to be accurate and comparable with the commercial software RES2DMOD (Vachiratienchai, 2007; Boonchaisuk, 2007). Note that the original code of Vachiratienchai (2007) is written in MATLAB script. In this

thesis, all the MATLAB routines are transformed into FORTRAN 95/2003 modules with the LAPACK library.

### MT forward modeling

For the 2-D MT forward modeling, the second order Maxwell's equations are solved by assuming a plane wave with a time dependence  $e^{-i\omega t}$ . For the transverse electric (TE) model by assuming the electric currents flow parallel to the strike direction, we solve Maxwell's equation for electric field  $\mathbf{E}$  which can be expressed as

$$\nabla \times \nabla \times \mathbf{E} = i\omega\mu\sigma\mathbf{E}. \quad (3.32)$$

For the transverse magnetic (TM) mode by assuming the electric currents flow perpendicular to the strike direction, we solve Maxwell's equation which can be expressed as

$$\nabla \times \rho \nabla \times \mathbf{H} = i\omega\mu\mathbf{H}. \quad (3.33)$$

Here  $\sigma$  is the conductivity, inverse of the resistivity  $\rho$ .  $\mu$  is the magnetic permeability for free space and  $\omega$  is the angular frequency.

In this thesis, we use the 2-D FD method with for TE and TM modes of Siripunvaraporn & Egbert (2000). The differential equation in (3.32) and (3.33) can be rearranged and expressed in the matrix form as

$$\mathbf{S}_m \mathbf{e} = \mathbf{b}. \quad (3.34)$$

Here  $\mathbf{S}_m$  is a 5-band sparse matrix of the 2-D FD discretization which depends on the model discretization and the angular frequency  $\omega$ ,  $\mathbf{e}$  is the unknown field ( $\mathbf{E}$  for TE and  $\mathbf{H}$  for TM) and  $\mathbf{b}$  is associated with the boundary conditions (see also Siripunvaraporn & Egbert, 2000; Smith & Booker, 1991) and the source field.

For the TE mode, once the electric field  $\mathbf{E}(\omega)$  at each  $\omega$  is solved, the magnetic field  $\mathbf{H}(\omega)$  can be obtained from

$$\nabla \times \mathbf{E} = i\omega\mu\mathbf{H}, \quad (3.35)$$

using the FD approximation. For the TM mode, once the magnetic field  $\mathbf{H}(\omega)$  at each  $\omega$  is solved, the magnetic field  $\mathbf{E}(\omega)$  can also be obtained from

$$\nabla \times \mathbf{H} = \frac{1}{\rho}\mathbf{E}. \quad (3.36)$$

The data responses of MT, apparent resistivity and phase, can be calculated using equation (2.21) and (2.22),  $\rho_{xy}$  and  $\phi_{xy}$  for the TE mode, and  $\rho_{yx}$  and  $\phi_{yx}$  for the TM mode. Note that the original code is written by Siripunvaraporn & Egbert (2000) in FORTRAN 77. In this thesis, we create FORTRAN 95/2003 modules to execute the original code.

### 3.5.3 Sensitivity matrix

The sensitivity  $\mathbf{J}$  denotes the change of the forward response with respect to the change of model parameters which can be expressed by

$$\begin{aligned} \mathbf{J} &= \frac{\partial \mathbf{f}}{\partial \mathbf{m}} \\ &= \begin{pmatrix} \frac{\partial f_1}{\partial m_1} & \frac{\partial f_1}{\partial m_2} & \cdots & \frac{\partial f_1}{\partial m_M} \\ \frac{\partial f_2}{\partial m_1} & \frac{\partial f_2}{\partial m_2} & \cdots & \frac{\partial f_2}{\partial m_M} \\ \vdots & \vdots & \frac{\partial f_i}{\partial m_j} & \vdots \\ \frac{\partial f_N}{\partial m_1} & \frac{\partial f_N}{\partial m_2} & \cdots & \frac{\partial f_N}{\partial m_M} \end{pmatrix}_{N \times M} \end{aligned} \quad (3.37)$$

where  $N$  is the number of data,  $i$  is the data index,  $M$  is the number of model parameter, and  $j$  is the model index.

In general, there are two major ways to calculate the sensitivity: the direct calculation and the reciprocity calculation (Rodi, 1976). In this thesis, both MT and DCR sensitivity follow the reciprocity method which reduce the forward modeling calls from depending on  $M$  to  $N$  (McGillivray and Oldenburg, 1990). The reciprocity sensitivity calculation is sophisticatedly explained in Siripunvaraporn & Egbert (2000).

For the joint inversion, the sensitivity matrix  $\mathbf{J}$  is the combination of the sensitivity matrices calculated from DCR and MT modeling,

$$\mathbf{J} = \begin{pmatrix} \mathbf{W}_{\mathbf{T}}^{\text{DCR}} \mathbf{J}_{\text{DCR}} \\ \mathbf{W}_{\mathbf{T}}^{\text{MT}} \mathbf{J}_{\text{MT}} \end{pmatrix}_{N_T \times M}, \quad (3.38)$$

where  $\mathbf{W}_{\mathbf{T}}$  is a sensitivity weighting matrix. Here, we usually set  $\mathbf{W}_{\mathbf{T}} = \mathbf{I}$ . Note that the inappropriate value setting for  $\mathbf{W}_{\mathbf{T}}$  could lead to the slow convergence of the solution or divergence.

### 3.5.4 Model covariance matrix $\mathbf{C}_{\mathbf{m}}$

Obtaining the model covariance from the inverse of the roughness operator is impractical because of its singularity. Siripunvaraporn and Egbert (2000) applied the diffusion equation to calculate  $\mathbf{C}_{\mathbf{m}} \mathbf{J}^T$  for 2-D MT avoiding the large direct construction of  $\mathbf{C}_{\mathbf{m}}$ .

Assuming  $U = U(z, x)$ , the diffusion equation in 2-D is given by

$$\frac{\partial U}{\partial t} = \kappa \nabla^2 U. \quad (3.39)$$

where  $t$  is a pseudo-time variable,  $\kappa$  is a diffusion coefficient and  $\nabla^2 = \frac{\partial^2}{\partial x^2} + \frac{\partial^2}{\partial z^2}$ .

To avoid the computational costs of solving the 2-D diffusion equation, we instead use the operator splitting method (Press *et al.*, 1992) to solve the 1-D diffusion equation in horizontal and vertical directions separately.

The implicit finite difference scheme which provides a stable solution can be expressed in the horizontal direction as

$$\begin{aligned} \frac{U_j^{n+1} - U_j^n}{\tau} &= \frac{\kappa}{h_{j-1,j+1}} \left( \frac{U_{j+1}^{n+1} - U_j^{n+1}}{h_{j+1,j}} - \frac{U_j^{n+1} - U_{j-1}^{n+1}}{h_{j-1,j}} \right) \\ &= \kappa \left( \frac{U_{j+1}^{n+1}}{h_{j+1,j-1} \cdot h_{j+1,j}} - \frac{U_{j-1}^{n+1}}{h_{j+1,j-1} \cdot h_{j-1,j}} - \frac{U_j^{n+1}}{h_{j+1,j} \cdot h_{j-1,j}} \right). \end{aligned} \quad (3.40)$$

Equation (3.40) can be expressed in matrix form,

$$\mathbf{u}^n = (\mathbf{I} + \tau\kappa\mathbf{H})\mathbf{u}^{n+1}, \quad (3.41)$$

where  $\tau$  is the time step,  $h_{i+1,i}$  denotes the distance from the center of block  $i$  to block  $i+1$ ,  $\mathbf{H}$  is an  $M_x \times M_x$  diffusion operator in the  $x$  direction,  $\mathbf{I}$  is an one-diagonal matrix, and  $\mathbf{u}$  is an  $M_z \times M_x$  matrix.

$$\mathbf{u}^{n+1} = \mathbf{D}_\mathbf{H}^T \mathbf{u}^n \quad (3.42)$$

where  $\mathbf{D}_\mathbf{H} = (\mathbf{I} - \tau\kappa\mathbf{H})^{-1}$ . Similarly, the vertical diffusion equation can also be expressed as

$$\frac{U_i^{n+1} - U_i^n}{\tau} = \kappa \left( \frac{U_{i+1}^{n+1}}{v_{i+1,i-1}v_{i+1,i}} - \frac{U_{i-1}^{n+1}}{v_{i+1,i-1}v_{i-1,i}} - \frac{U_i^{n+1}}{v_{i+1,i}v_{i-1,i}} \right), \quad (3.43)$$

and can be written in the matrix form,

$$\mathbf{u}^n = (\mathbf{I} + \tau\kappa\mathbf{V})\mathbf{u}^{n+1}, \quad (3.44)$$

or,

$$\mathbf{u}^{n+1} = \mathbf{D}_\mathbf{V} \mathbf{u}^n \quad (3.45)$$

where  $\mathbf{D}_\mathbf{V} = (\mathbf{I} - \tau\kappa\mathbf{V})^{-1}$ .  $\mathbf{V}$  is an  $M_z \times M_z$  diffusion operator in the  $z$  direction.

The model covariance matrix can then be expressed as

$$\mathbf{C}_\mathbf{m} = \left[ \mathbf{D}_\mathbf{H}^{\frac{1}{2}} \mathbf{D}_\mathbf{V} \mathbf{D}_\mathbf{H}^{\frac{1}{2}} \right]^{n_\tau}, \quad (3.46)$$

where  $n_\tau$  is an appropriate number of time steps to solve the diffusion equation. The smoothness of the obtained model depends significantly on  $\mathbf{C}_\mathbf{m}$ . It is controlled by the diffusion length scale ( $l_m$ ) which can be obtained from

$$l_m = \sqrt{4\tau\kappa}. \quad (3.47)$$

A smoother model corresponds to a larger  $l_m$ . Therefore,  $l_m$  is one of the important parameters in the inversion and should be carefully determined.

### 3.6 Inversion process

In order to perform the inversion (see also Algorithm 1), we start the first iteration  $k = 1$  with the initial model  $\mathbf{m}_{k=1}$  which is usually the homogeneous halfspace. Its average resistivity  $\bar{\rho}_a$  can be calculated by the geometric mean of the apparent resistivity data (see also Boonchaisuk *et al.*, 2008),

$$\bar{\rho}_a = \sqrt{\rho_a^1 \cdot \rho_a^2 \cdot \rho_a^3 \cdots \rho_a^N}, \quad (3.48)$$

where  $N$  is the total number of apparent resistivity data. However,  $\bar{\rho}_a$  can be given by any appropriate value. The prior geology information can be included in the reference model  $\mathbf{m}_0$ , otherwise, the starting model will be used as the reference model. Note that an inappropriate starting model and reference model could lead to divergence of the solution.

To quantify the data misfit  $\chi_d^2$  between the observed data and the generated data from the inversion model, we use the root mean square (RMS) misfit which can be obtained by

$$\text{RMS} = \sqrt{\frac{\chi_d^2}{N}}, \quad (3.49)$$

where  $N$  is number of data. A RMS misfit of 1 implies that the calculated data from the inverted model fits the observed data within the data variance or error given by  $\epsilon_i$  in equation (3.2). Note that a RMS of less than 1 indicates that noises could be modeled and produce spurious features in the inverted model (Sasaki, 1989; Candansayar, 2008). Therefore, we do not allow the RMS misfit to be reduced to less than 1 in our inversion.

#### 3.6.1 Line search for $\lambda$

At every iteration, we search for the optimal  $\lambda$  value that gives the minimum RMS misfit at the desired level in Phase I or minimizes model norm  $\chi_m^2$  in Phase II. We apply the 1-D line searching method by using the fact that, within the range of  $\log_{10} \lambda \in [0, 6]$ , the misfit is a smooth function of  $\lambda$  which is also a unimodal curve, i.e. only one minimum exists. Here, we use a “golden section” search which is simple but efficient, moderately fast and robust (see also Kiefer, 1953; Avriel & Wilde, 1966; Press *et al.*, 1992; Vachirastienchai, 2007).

Note that, in some cases, the desired RMS misfit may not be reached and Phase II would not be performed. The model with the minimum misfit which higher than the desire level might contain some spurious features. An additional smoother iteration is preferred to find the minimum model norm with the achieved RMS misfit.

## CHAPTER IV

### NUMERICAL AND REAL EXPERIMENTS

In this chapter, we apply our developed joint inversion to synthetic and real data. All experiments are run on a personal computer using Intel Core 2<sup>TM</sup> Quad with 4 GB of RAM. After validation, the usefulness of the joint inversion is demonstrated.

#### 4.1 Synthetic experiments

Sets of the synthetic data are generated from synthetic models using the 2-D DCR and 2-D MT forward modeling techniques as described in section 3.5.2. The calculated data are then treated as the observed data. We start with the synthetic case I of the famous simple two boxes in the shallow case. Then we will extend the test to the more complex model in the synthetic case II. From case I and case II, the accuracy and efficiency of the codes will be demonstrated from individual data inversions. In addition, these cases are designed to demonstrate that the resolution of the inverted model from the joint inversion would be improved. The synthetic case III is purposely created to demonstrate the reliability of the joint inversion for the situation that the MT data are distorted by the static shift effect.

##### 4.1.1 Synthetic case I: The two buried boxes

In case I, two  $50\text{ m} \times 50\text{ m}$  boxes of  $1000\ \Omega\text{ m}$  and  $10\ \Omega\text{ m}$  are buried 5 m beneath the surface in the  $100\ \Omega\text{ m}$  host as illustrated in Figure 4.1.

To obtain accurate synthetic data, the model is discretized into a fine  $110 \times 50$  grid. The horizontal grids are equally discretized in the interesting area. The vertical grids are more coarsely divided with increasing depth. Note that the actual model domain is further extended to the left, right and bottom directions to reduce the boundary effect (see also Siripunvaraporn & Egbert, 2000; Vachiratienchai, 2007).

#### Synthetic data and model setup

We set up the DCR and the radiomagnetotelluric (RMT) surveys on the surface of this model with a 200 m-long profile. For the RMT configuration, there are 9

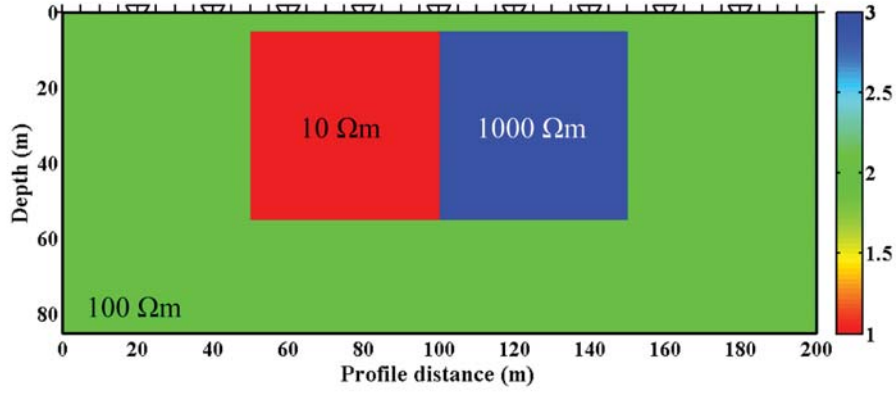


Figure 4.1: Synthetic model of the two boxes case

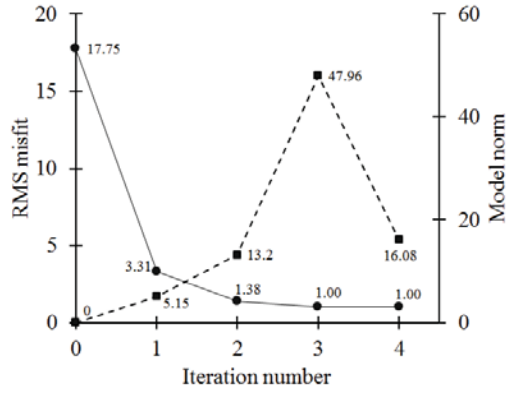
stations which are equally separated by 20 m as shown by the triangular markers in Figure 4.1. 20 frequencies ranging from 1000 kHz to 1 kHz are used for apparent resistivity and phase from both TE and TM modes. For the DCR configuration, the electrode positions are placed coincident with the MT profile as shown by the bar markers. There are a total of 41 electrodes with 5 m of electrode spacing. The synthetic apparent resistivity responses of the Schlumberger array are generated with a pseudodepth of up to 20 levels,  $n = 1, 2, 3, \dots, 20$  (Figure 4.4a).

There are 720 data points for RMT (360 points for the TE mode and 360 points for the TM mode) and 381 data point for DCR. Therefore, the total number of data points is  $N = 1101$ . In this case, no noises are added. The target RMS misfit is set to 1.00 with the given 5% data error.

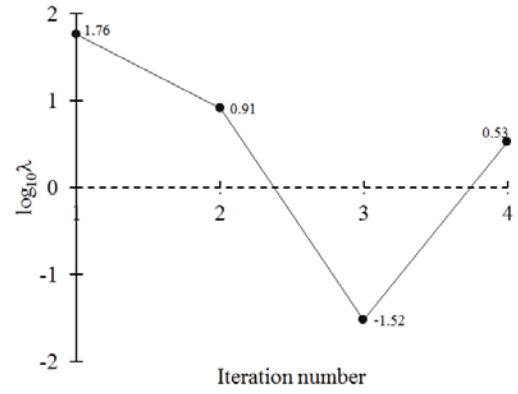
The grid discretization used for the inversion is coarser than the forward modeling mesh to reduce the computational cost. The starting model and reference model is a homogeneous halfspace discretized in a  $54 \times 40$  mesh with the given resistivity of  $110 \Omega \text{ m}$ . The number of model parameters is then  $M = 2160$ . Single data inversions and the joint inversion are performed using the same starting and reference models.

## Inversion result

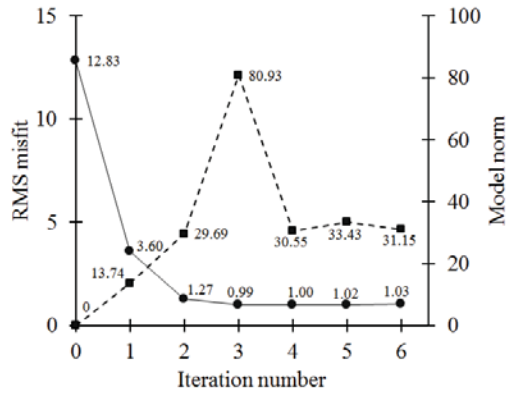
Figure 4.2 shows the RMS misfit and the model norm of each inversion. For Phase I of the inversion, the early iterations are devoted to decrease the RMS misfit to the desired level. The RMS misfits of all inversions reach the desired level  $\text{RMS} = 1.00$  within a few iterations. Note that in Phase I the model norm is increasing from 0 (of the halfspace) according to the features added to the inverted model. Once the desired



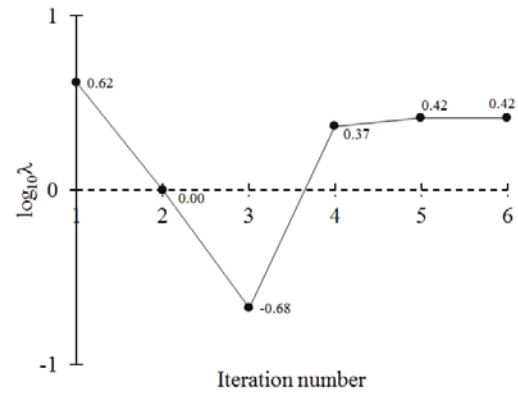
(a) DCR inversion



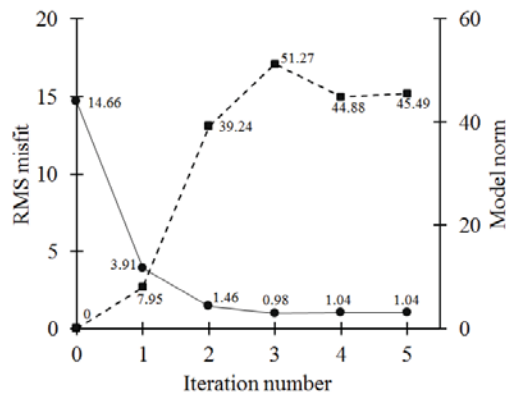
(b) DCR inversion



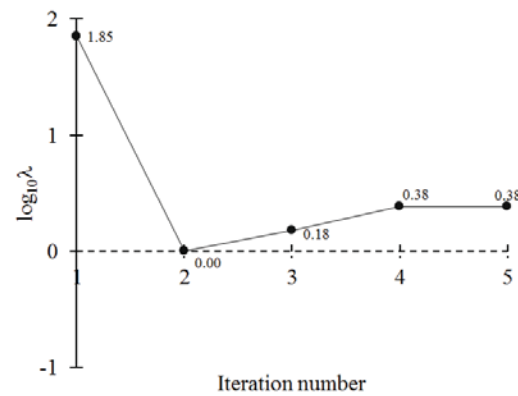
(c) MT inversion



(d) MT inversion



(e) Joint inversion



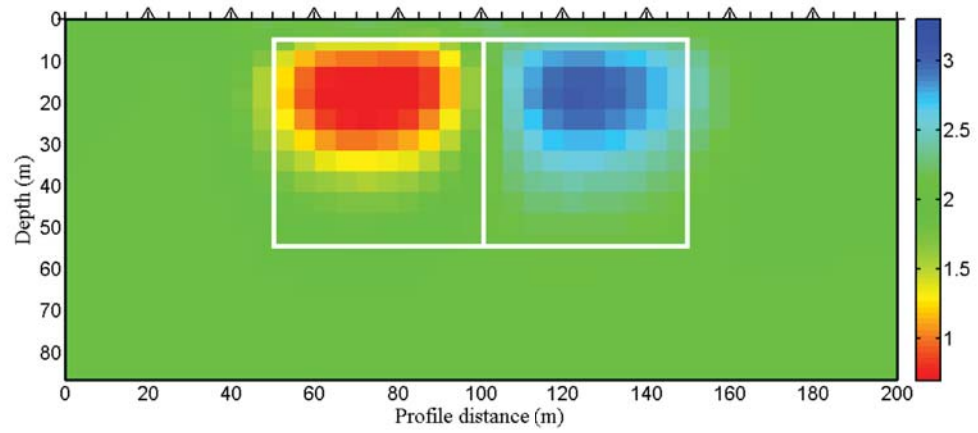
(f) Joint inversion

Figure 4.2: RMS misfits and model norms for each iteration from (a) single DCR inversion, (c) single MT inversion and (e) joint inversion of DCR & MT. The solid line with the circles represent the RMS misfit. The dashed line with the squares represent the model norm.  $\log_{10} \lambda$  for each iteration are also shown (b), (d) and (f) for DCR, MT and joint inversion, respectively.

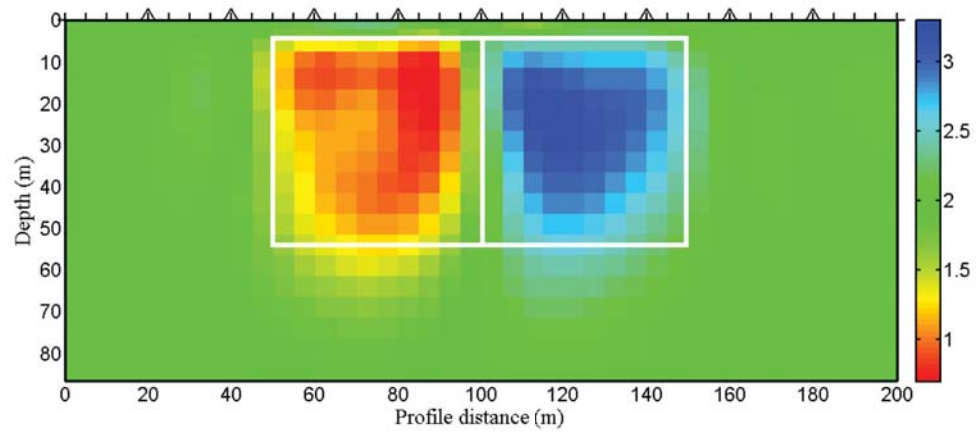
RMS is reached, further smooth iterations of Phase II are performed to minimize the model norm. The program will stop when the model norm cannot be decreased or slightly changed.

The inverted model of the single DCR inversion is presented in Figure 4.3a. Vertical and horizontal axis represents the vertical and horizontal spatial position respectively. The colorbar indicates the resistivity in a  $\log_{10}$  scale. The triangular markers placed along the horizontal axis are the locations of the RMT stations while the bar markers present the DCR electrode positions. The RMS misfit of the DCR inversion is reduced from 17.75 to 1.00 within 3 iterations. The model of the 4<sup>th</sup> iteration is used as the inverted model of the DCR inversion because the model norm does not decrease after the 4<sup>th</sup> iteration as shown in Figure 4.2a. In Figure 4.3a the two boxes can be recovered. The distance between the top boundary of the boxes and the surface is accurately resolved. However, the true bottom boundary of the two boxes cannot be well recovered because of the shorter investigation depth of the DCR survey. For a typical Schlumberger array with 5 m electrode spacing, the investigation of the deepest pseudodepth of  $n = 20$  is about 30 m (Oldenburg & Li, 1999) shorter than the 50 m bottom of the anomalies. Interpretation from a single DCR inversion may lead to the wrong estimation of the size of the two anomalies. The calculated data from the inverted model matches well with the observed data within the data variance as shown in Figure 4.4.

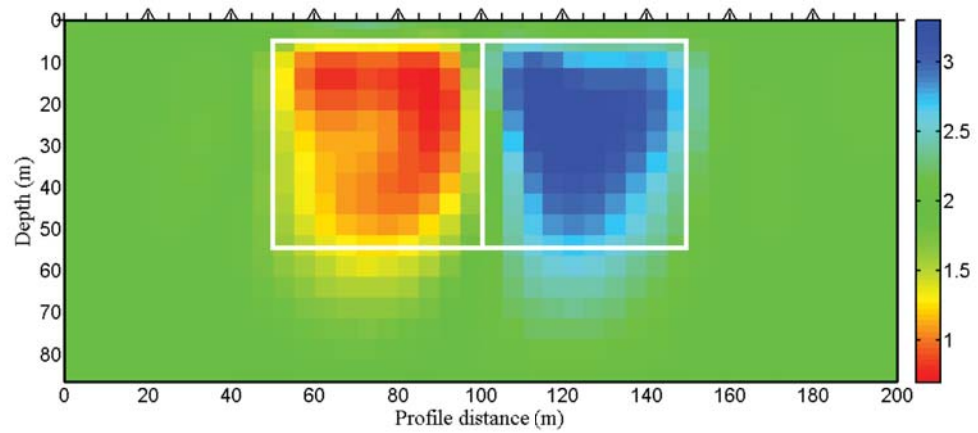
The result from the single MT inversion is shown in Figure 4.3b. We use the same color scale as with the DCR model. The RMS misfit is reduced from 12.83 to 1.00 within 3 iterations. The 4<sup>th</sup>, 5<sup>th</sup> and 6<sup>th</sup> are the Phase II inversion. We select the model from the 6<sup>th</sup> iteration as the inverted model of the MT inversion (Figure 4.3b). Although the model norm of the 4<sup>th</sup> iteration is slightly less than that of the 6<sup>th</sup> iteration, we prefer the inverted model generated from more than one smooth iteration of Phase II. In addition, the  $\lambda$  value is stable at this iteration as shown in Figure 4.2c and 4.2d. The model obtained from the MT survey can resolve both anomalies in a similar way to the DCR inversion as shown in Figure 4.3a. The calculated response from the inverted model also matches the synthetic data as shown in Figure 4.5 for TE and 4.6 for TM. One significant difference is that MT accurately resolves the bottom boundary of the two boxes. This is because the investigating frequencies of  $10^6$  to  $10^3$  Hz can cover the structure from 5 m up to 160 m calculated from the skin depth of the 100  $\Omega$  m halfspace (see also equation (2.15)). For this reason, MT is better at resolving the two boxes from the top to the bottom. The resistivity value of the two boxes obtained from the MT model is closed to that of the DCR model. However, the resistivity model from the DCR model is smoother. This occurs because the MT station locations are placed further



(a) DCR inversion

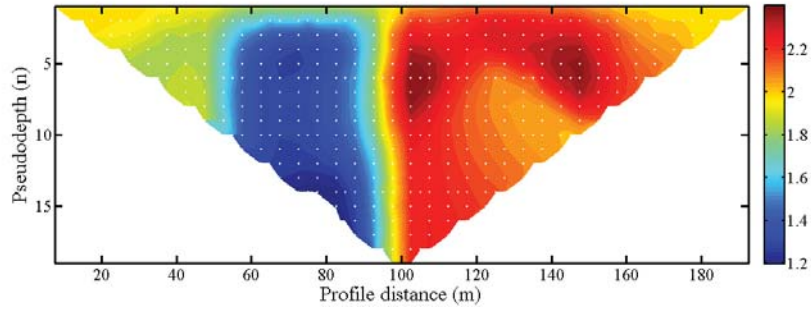


(b) MT inversion

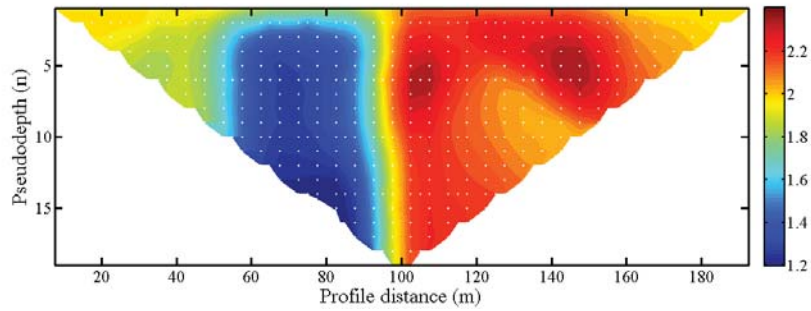


(c) Joint inversion

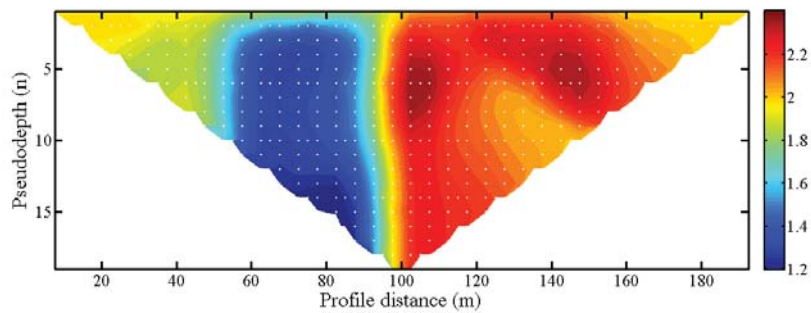
Figure 4.3: Inverted models from (a) the single DCR inversion, (b) the single MT inversion and (c) the joint inversion of DCR & MT. The white squares show the boundary of the boxes from the synthetic model.



(a) DCR observed data: Schlumberger array.

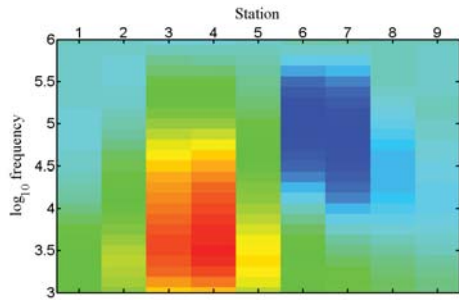


(b) The calculated DCR response from the inverted model from a single DCR inversion.

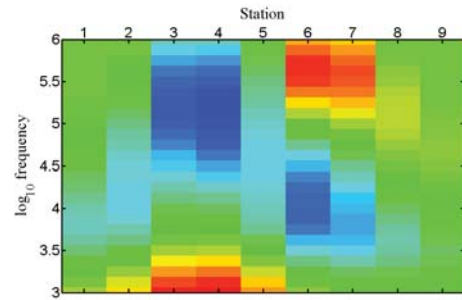


(c) The calculated DCR response from a joint inversion of DCR and MT.

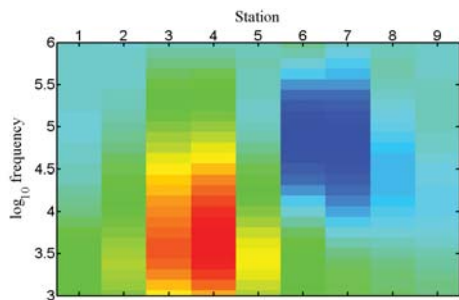
Figure 4.4: Schlumberger array data. All use the same color scale.



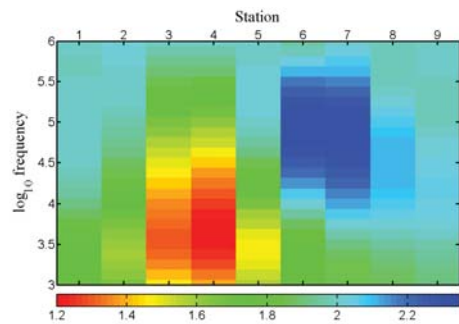
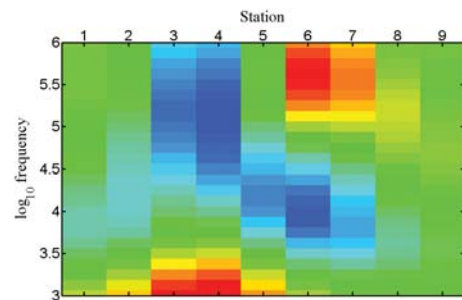
(a) Observed apparent resistivity for TE.



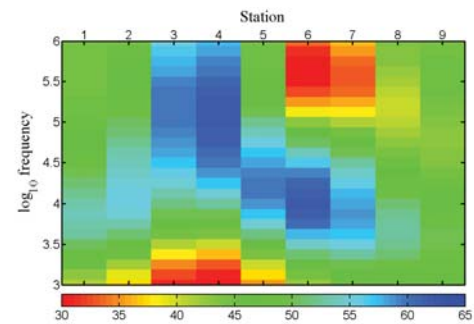
(b) Observed phase for TE.



(c) Calculated apparent resistivity for TE from a (d) Calculated phase for TE from a single MT inversion.

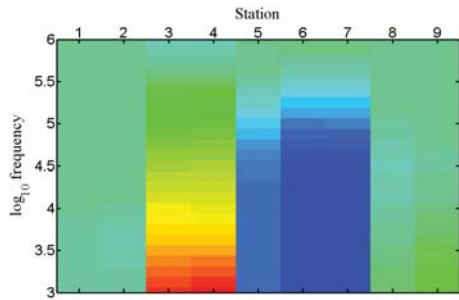


(e) Calculated apparent resistivity for TE from the

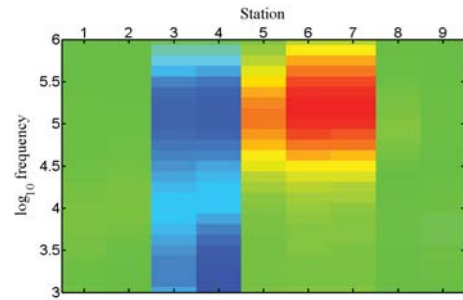


(f) Calculated phase for TE from the DCR+MT joint inversion.

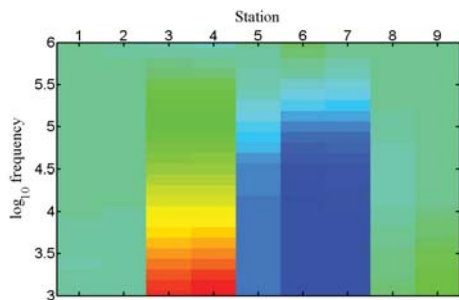
Figure 4.5: Apparent resistivity and phase responses in TE mode.



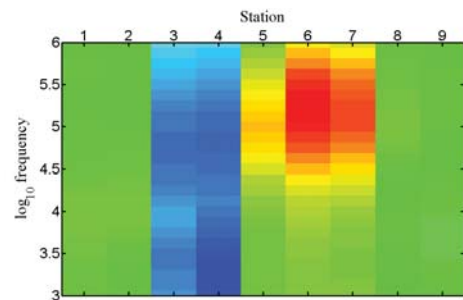
(a) Observed apparent resistivity for TM.



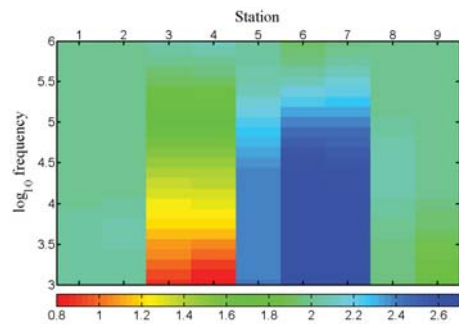
(b) Observed phase for TM.



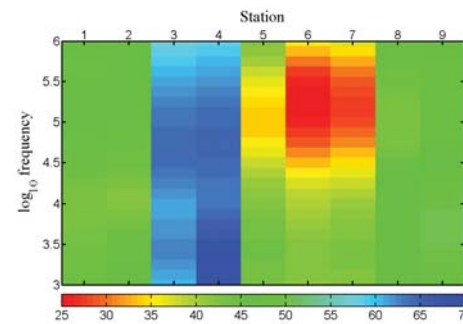
(c) Calculated apparent resistivity for TM from a single MT inversion.



(d) Calculated phase for TM from a single MT inversion.

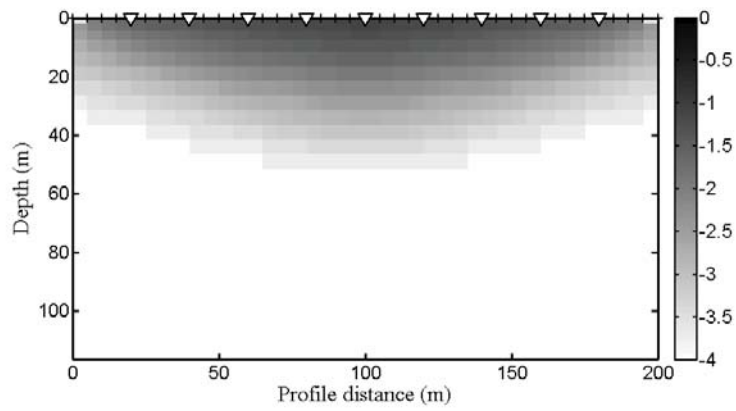


(e) Calculated apparent resistivity for TM from the DCR+MT joint inversion.

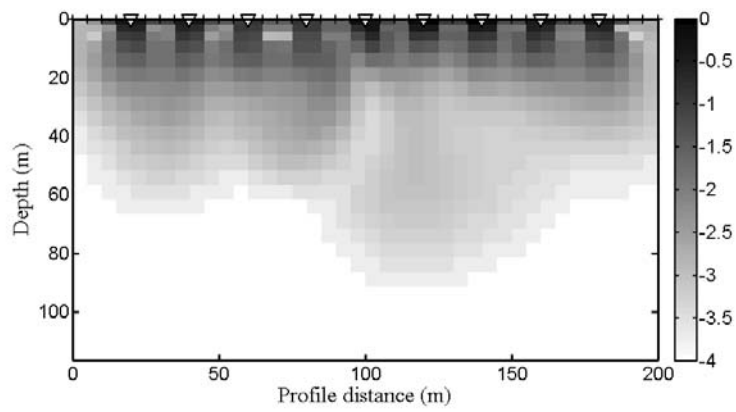


(f) Calculated phase for TM from the DCR+MT joint inversion.

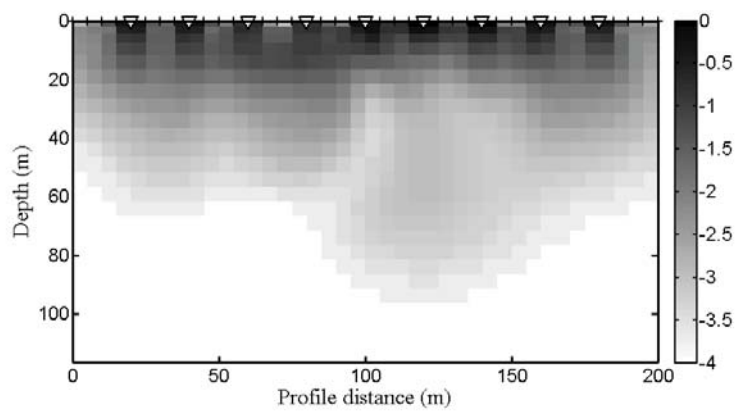
Figure 4.6: Apparent resistivity and phase responses in TM mode.



(a) Model resolution matrix of the DCR inversion.



(b) Model resolution matrix of the TE&TM inversion.



(c) Model resolution matrix of the joint the TE&TM+DCR inversion.

Figure 4.7: The model resolution matrix (a) DCR, (b) TE & TM and (c) TE & TM + DCR.

apart. Note that for both DCR and MT models, there are no spurious features. This is due to the smoothness constraint of the inversion.

Next, we run the joint inversion of DCR and MT using the same starting and reference model of both DCR and MT inversions. The RMS misfit is started at 14.66 as expected between the starting DCR and MT RMS misfit before being reduced to the desired level of 1.00 within the first 3 iterations. We select the model from the 5<sup>th</sup> iteration as the final inverted model from the joint inversion. The calculated data from the inverted model is also close to the observed data as shown in 4.4, 4.5 and 4.6. As shown in Figure 4.3c, the inverted model is significantly improved and matches better with the true model than the DCR inversion. The recovery of the bottom of the two boxes are improved from the MT data. On the other hand, comparing to that of the MT model, the resistivity distribution of the joint inversion model is smoother due to the incorporation of the DCR data.

In addition, we use the model resolution matrix (MRM) described in Alumbaugh & Newman (2000) to confirm the resolution improvement of the obtained model from the joint inversion as shown in Figure 4.7. The MRM is presented in a model plot using a gray color scale giving the sensitivity of the model at each element contributed by the data. The darker (black) color shows a higher value of MRM indicating a more reliable area. For the DCR inversion, the MRM is decreased from the top to the deeper part and starts to vanish beyond 30 m which is shallower than the bottom of the boxes. For this reason, the bottom of the boxes cannot be certainly recovered by the single DCR inversion. On the other hand, the MRM of the MT exhibits deeper sensitivity which covers the whole boxes. The MRM of the joint inversion is therefore higher than the single inversions of both methods which can explain the improvement of the model.

## Discussion

From the results of the single inversions and the joint inversion, we could summarize the nature of both methods. The DCR survey provides good lateral and vertical resolutions within its investigation depth because the electrodes are close together and continue throughout the investigation profile. However, in many cases, the target structures may be located deeper than the investigation depth of the typical DCR survey. This can be solved by combining with the RMT survey to improve the vertical resolution as mentioned. Another remarkable issue is the increased lateral resolution of the MT survey. The MT stations are usually separated by some distance which is usually larger than the horizontal discretized grid. This may yield the discontinuity in the lateral direction in the MT model as mentioned. However, the lacking of the lateral resolution of the MT method can be resolved by combining with the DCR data which

resulted in the joint inversion model.

### 4.1.2 Synthetic case II: Complex structure

As illustrated in Figure 4.8, the model in this case is the two layers model with the step interface. The top layer of  $100\ \Omega\text{m}$  lies above the base layer of  $1000\ \Omega\text{m}$ . The interfaces of the two layers are 30 m and 15 m respectively from left to right terminated at the center of the model. In the deeper part of the top layer, there is the 10 m sill with  $10\ \Omega\text{m}$  thick and lies at a depth of 10 m. We add the surface resistive sheet of 5 m thickness under the 1<sup>st</sup>, 2<sup>nd</sup> and 3<sup>rd</sup> RMT stations. We also add the surface conductive sheet of 7.5 m thickness under the 7<sup>th</sup>, 8<sup>th</sup> and 9<sup>th</sup> RMT stations. We also divide the model into a fine  $110 \times 50$  grid as in Case I.

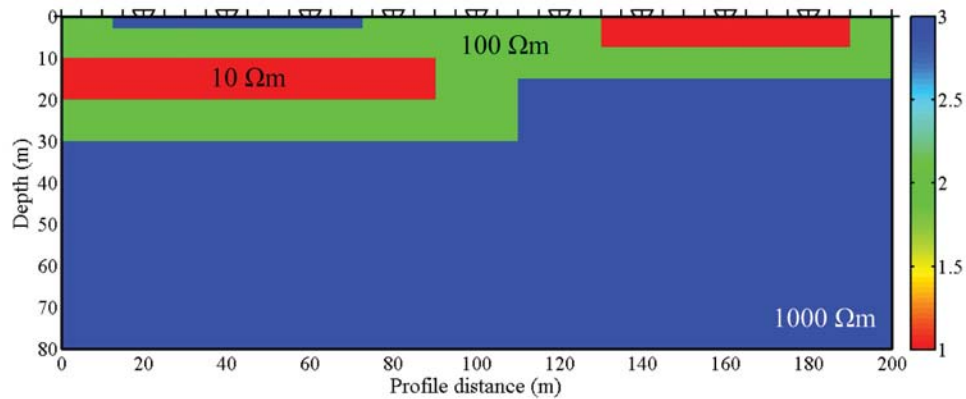


Figure 4.8: Synthetic model of case II.

### Synthetic data and model setup

We set up the synthetic DCR and RMT survey across this model with a 200 m-long profile as in Case I. For the RMT data, there are 9 station which are equally separated by 20 m of spacing. We also use 20 frequencies. The frequencies are equally varied logarithmically from 250 kHz to 1 kHz. We inherit this configuration from the real RMT survey which limits the highest frequency to 250 kHz according to noise and equipment limitations (see Monteiro Santos *et al.*, 2007; Candansayar, 2008). The synthetic data including apparent resistivity and phase are generated in both the TE and TM modes with the 2-D MT forward modeling routine as illustrated in Figure 4.11a for the TE mode and 4.12a for the TM mode. For the DCR data, we also set the electrode positions along with the MT profile. There are 41 electrodes with 5 m electrode spacing. The synthetic apparent resistivity responses are generated for the Schlumberger array

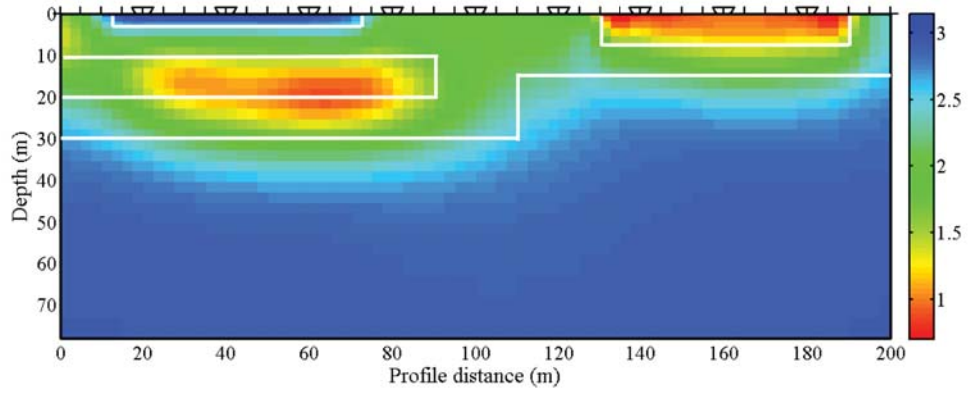
with pseudodepth at 20 levels,  $n = 1, 2, 3, \dots, 20$ . In this case II, we add the additional data of 10 m electrode spacing with 5 pseudodepths ( $n = 1, 3, 5, 7$  and 9) and 15 m electrode spacing with 3 pseudodepth ( $n = 1, 3$ , and 5) (Figure 4.10a). The additional data with wider potential electrode spacing can help to improve the lateral resolution (Loke & Barker, 1996). This extended data can be acquired using the same configuration without moving or extending the profile which is available on modern multi-electrode equipment such as SYSCAL R1 Plus Switch-48 (see also Boonchaisuk *et al.*, 2008) and our code also supports this feature.

There are 720 data points for RMT (360 points for the TE mode and 360 points for the TM mode) and 451 data points for DCR. Therefore, the total number of data points is  $N = 1171$ . In this case, no noises are added. The target RMS misfit is set to 1.00 with the given 5% data error.

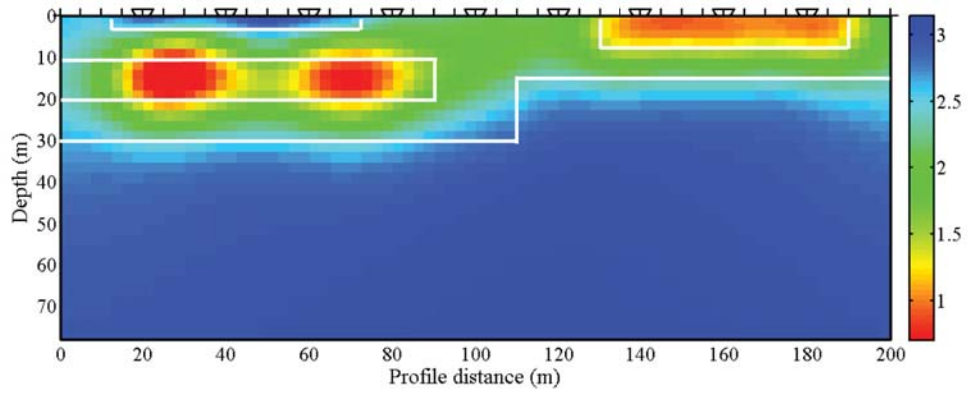
The starting model and reference model is a homogeneous halfspace discretized in a  $108 \times 50$  mesh with the given resistivity of  $900 \Omega \text{ m}$ . The number of model parameters is  $M = 5400$  which is 5 times larger than  $N$ . Both single inversions and joint inversion are performed using the same starting and reference models.

The RMS misfit of the DCR inversion is reduced from 23.21 to 1.00 within 3 iterations. We use the model of the 4<sup>th</sup> iteration as the inverted model of the DCR inversion. In the inverted model, all structures can be recovered. The calculated data from the inverted model is close to the synthetic data (within the data variance) as shown in Figure 4.10. The resistivity of the two sheets is resolved close to the true resistivity of the synthetic model. The size of the sheets are accurately resolved in both the conductive and resistive sheets. The conductive sill is also recovered. However, only the right part of the sill is resolved. This is because the horizontal coverage of the Schlumberger array does not cover the left part of the sill. This could be solved by adding more electrodes over the investigation area in both the left and right side to get the full data coverage throughout the investigation area. In addition, the depth and the thickness of the sill is fairly well recovered. This is because of the investigation depth of the DCR configuration. This could be poorly resolved if we use a Schlumberger array with only 5 m electrode spacing. The sharp step of the interface is not clearly revealed. This is the same as the synthetic model and is true in general when we use a smoothness-constraint inversion. However, the depth of the interface on the right part is close to the true depth of 15 m. The left part of the recovered interface is extended further to 40 m which is also due to the short investigation depth. We expect the improvement in these issues by using the joint inversion.

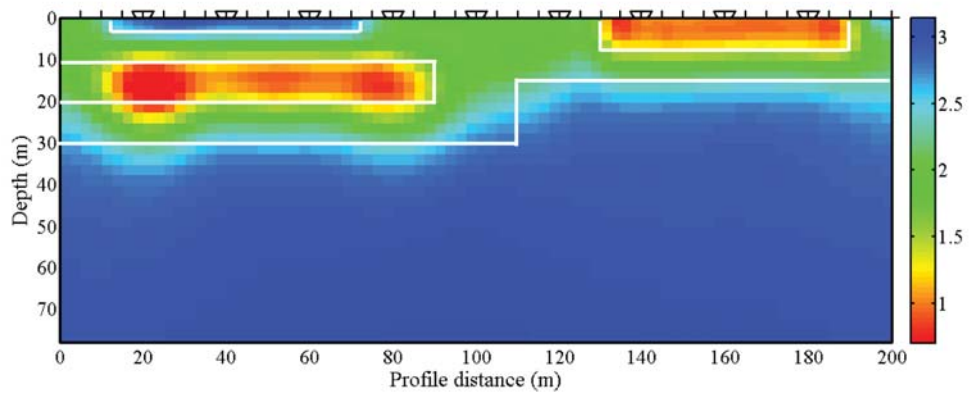
The result from the single MT inversion is shown in Figure 4.9b. The RMS misfit is reduced from 15.82 to 1.00 within 3 iterations. We select the model from the



(a) DCR inversion

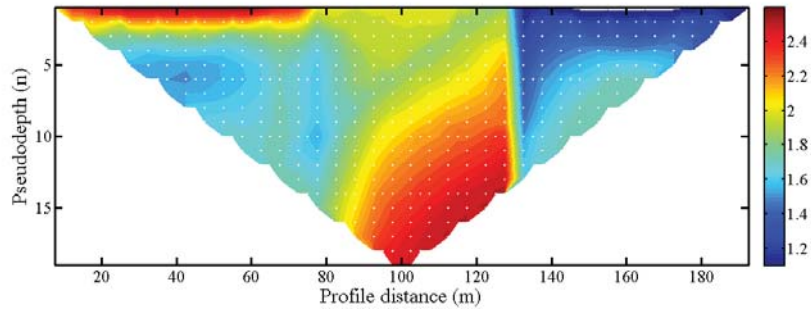


(b) MT inversion

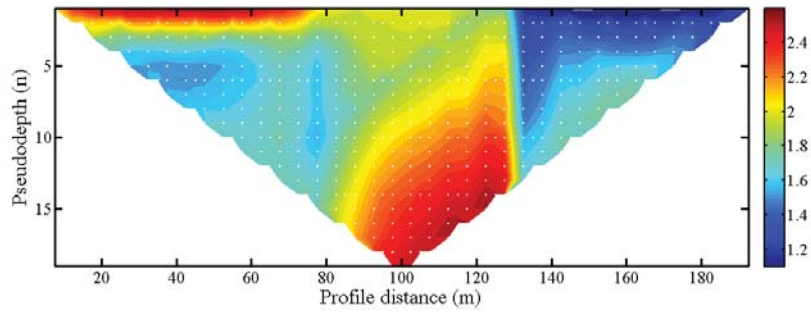


(c) Joint inversion

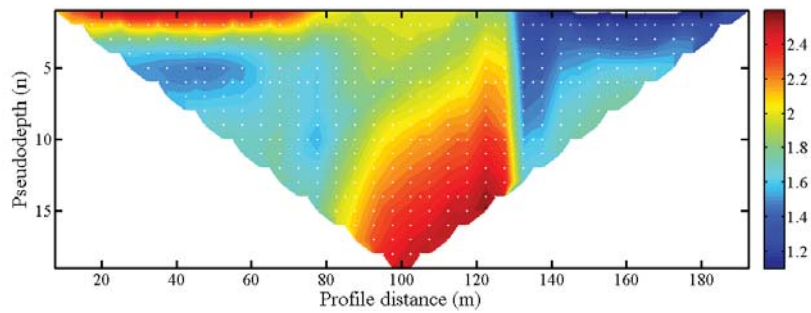
Figure 4.9: Inverted models of the inversions (a) single DCR inversion, (b) single MT inversion and (c) joint inversion of DCR & MT. The white squares show the boundary of the features from the synthetic model.



(a) DCR synthetic data: Schlumberger array.

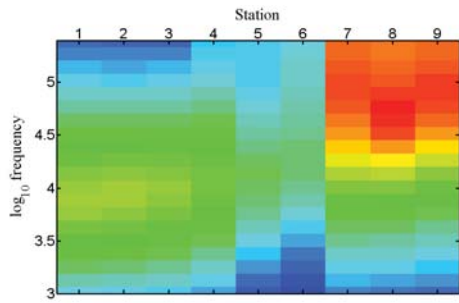


(b) The generated DCR data of the inverted model from a single DCR inversion.

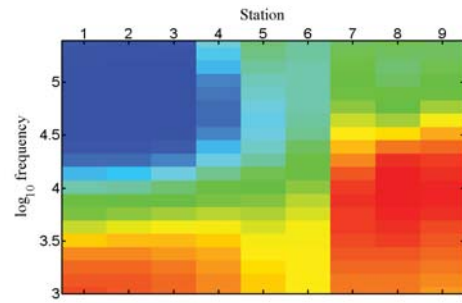


(c) The generated DCR data of the inverted model from a joint inversion of DCR and MT.

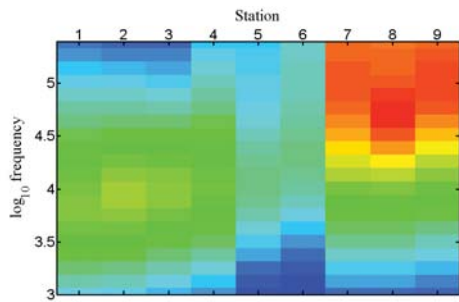
Figure 4.10: DCR data of Schlumberger array from the inversions. All use the same color scale.



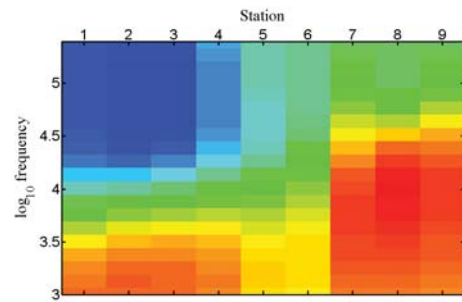
(a) Observed apparent resistivity for TE.



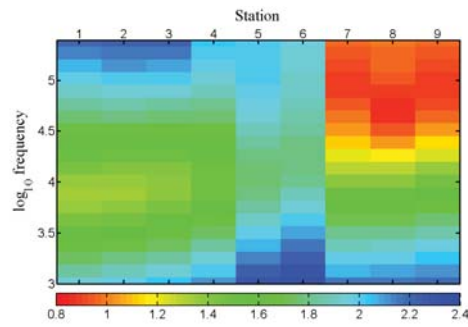
(b) Observed phase for TE.



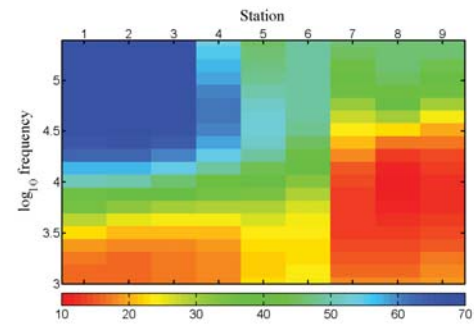
(c) Calculated apparent resistivity for TE from a single MT inversion.



(d) Calculated phase for TE from a single MT inversion.

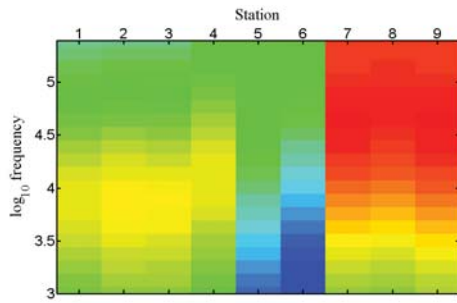


(e) Calculated apparent resistivity for TE from the DCR+MT joint inversion.

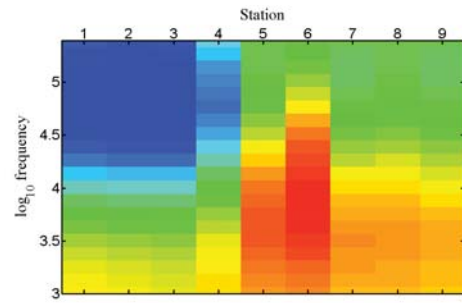


(f) Calculated phase for TE from the DCR+MT joint inversion.

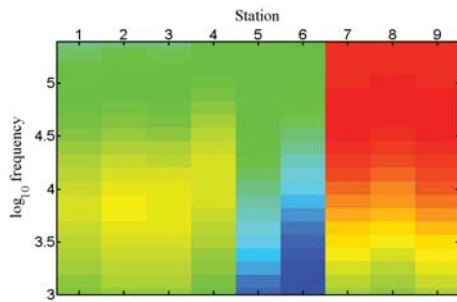
Figure 4.11: Apparent resistivity and phase responses in TE mode from the MT inversions.



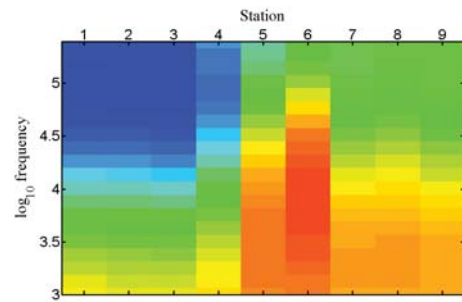
(a) Observed apparent resistivity for TM.



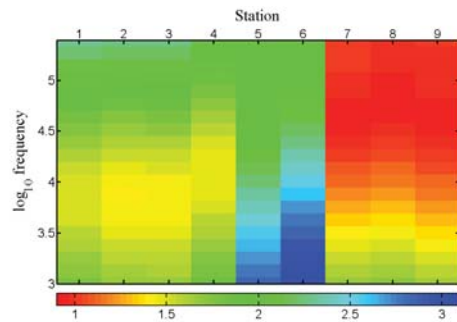
(b) Observed phase for TM.



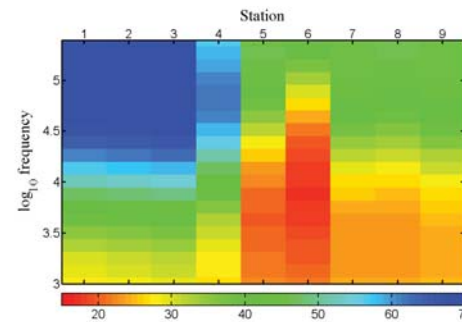
(c) Calculated apparent resistivity for TM from a single MT inversion.



(d) Calculated phase for TM from a single MT inversion.

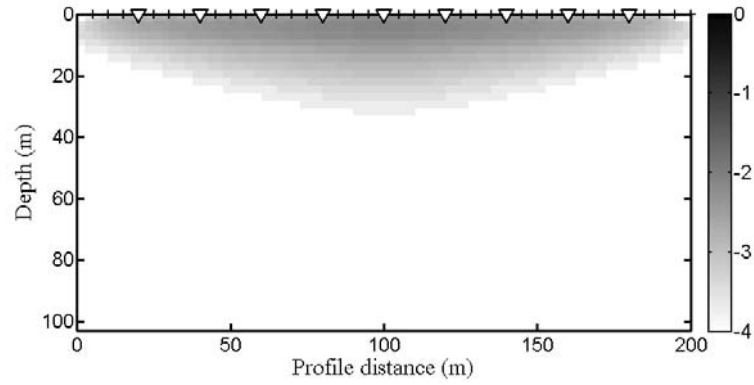


(e) Calculated apparent resistivity for TM from the DCR+MT joint inversion.

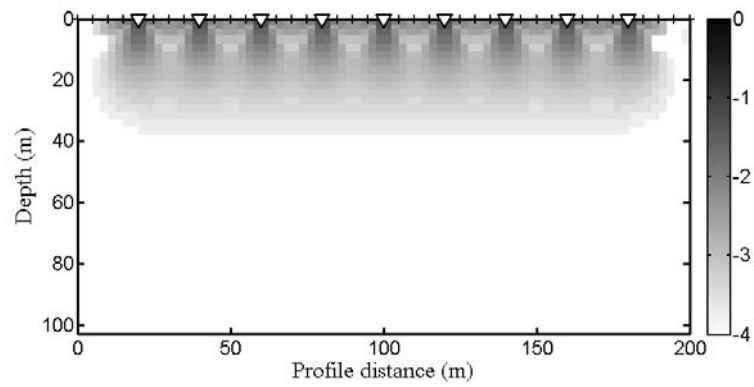


(f) Calculated phase for TM from the DCR+MT joint inversion.

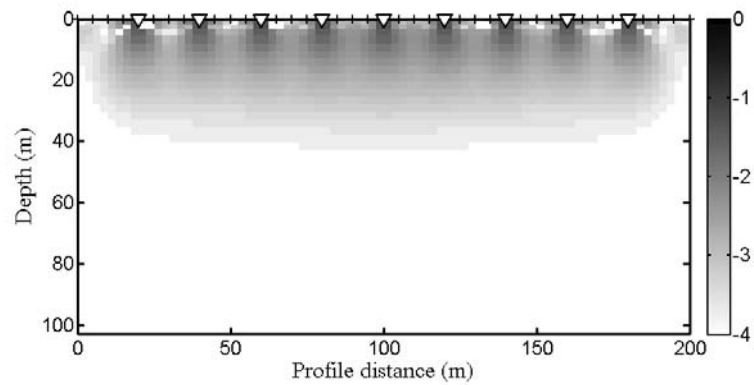
Figure 4.12: Apparent resistivity and phase responses in TM mode from the MT inversions.



(a) Model resolution matrix of the DCR inversion.



(b) Model resolution matrix of the TE&TM inversion.



(c) Model resolution matrix of the joint the TE&TM+DCR inversion.

Figure 4.13: The model resolution matrix (a) DCR, (b) TE&TM (c) TE&TM+DCR.

7<sup>th</sup> iteration as the inverted model of the MT inversion. The calculated data from the inverted model is close to the synthetic data as shown in Figure 4.11 and 4.12. From the result, there are remarkable issues in the model features. The MT survey cannot recover the resistive sheet because the resistive sheet is too thin (5 m thick) and too shallow compared to the highest investigating frequency. 250 kHz yields the skin depth of 10 m. When the shallowest investigation frequency is deeper than the structures, the inverted model usually produced the blurred image as shown in Figure 4.9b at the top left part. However, MT can recover the conductive sheet accurately in both size and resistivity. The interface of the two layers is resolved at the true depth of 30 m and 15 m. One significant issue of the MT model is the recovery of the sill. In Figure 4.9b, we can see that MT inversion divides the lateral sill into two conductive zones. This occurs because the inversion tries to fit the high resistive value at the 2<sup>nd</sup> and 3<sup>rd</sup> stations. The lacking of the lateral resolution is one of the limitations of the MT survey associated with station configurations. We also expect to improve these issues using the joint inversion.

We run the joint inversion of DCR and MT with the assumption that the model from the joint inversion would be improved and could preserve the benefit of both inversions. The joint inversion is performed by using the same starting and reference model of both DCR and MT inversions. The RMS misfit is started at 14.66 and reduced to the desired level of 1.00 within the first 3 iterations. We select the model from the 6<sup>th</sup> iteration as the inverted model from the joint inversion as shown in Figure 4.9. The calculated data from the inverted model is also close to the synthetic data as shown in Figure 4.10, 4.11 and 4.12. As mentioned in the DCR and MT inversion results, there are three issues that we will use as accuracy and efficiency gauges, including, recovery of the surface resistive and conductive sheets, lateral resolution of the sill, and depth of the two layer interface. The inverted model obtained from the joint inversion is significantly improved and better matched with the true synthetic model. The inversion can accurately recover both resistive and conductive sheets in both size and resistivity. The sill is better resolved than with the single inversions. Depth and thickness are close to the true model. In addition, if we extend the DCR electrodes and MT sites in both the left and right sides the coverage of the model would be improved. Moreover, the depth of the two layers is resolved at the true depth of 30 m and 15 m inherited from the MT model. As in Figure 4.13, the MRM also illustrates the superior resolution for the joint inversion when compared to the single inversions.

## Discussion

The joint inversion definitely improves the accuracy of the inverted model. The resolution in both horizontal and vertical direction are better than with the single inversions.

### 4.1.3 Synthetic case III: MT static shift correction

The typical problem of all variant MT explorations occurs when surface inhomogeneity is present under or near the stations. This surface inhomogeneity could be an air cavity or water-filled cavity and can distort the MT data. Electrical current would tend to flow into a conductive inhomogeneity while flowing away from a resistive one. This causes a frequency-independent parallel shift in one or both the TE and TM apparent resistivity curves. The curve is shifted by some real factor. However, the phase remains the same. This phenomenon is called the MT static shift effect. If one or more stations are distorted, it can produce a large error of the model that can severely mislead an interpretation. The static shift correction has been a long challenge for geophysicists. It is hard to determine the level of the shifted apparent resistivity curve. Even two experts could give totally different corrections. There are many traditional ways to correct this effect using MT data alone, but it has some limitations (Sasaki & Meju, 2006).

In this case, we demonstrate another benefit of using our developed joint inversion of DCR and MT to solve the MT static shift problem when MT data is distorted or less reliable.

### Synthetic data and model setup

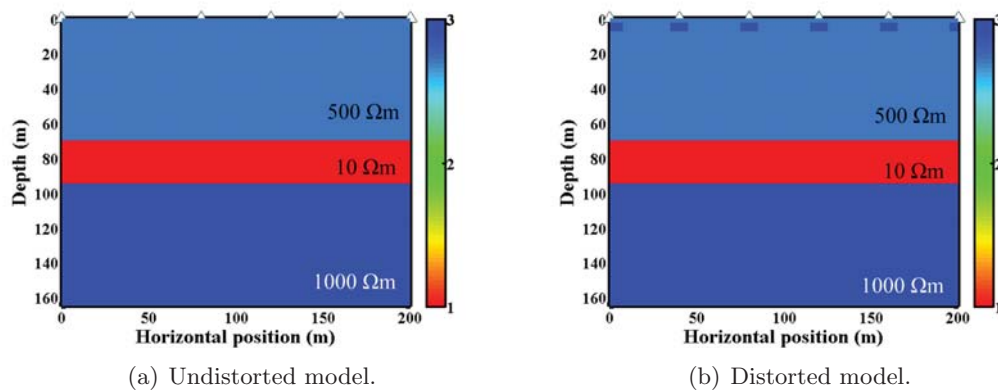


Figure 4.14: An example three-layer model, (a) is an example model without surface inhomogeneity. (b) is an example model with surface inhomogeneity.

The synthetic model consists of three layers. The 20 m-thick conductive

target layer of  $10 \Omega \text{ m}$  lies between the resistive layer of  $500 \Omega \text{ m}$  and  $1000 \Omega \text{ m}$  from the depth of 70 m to 90 m as shown in Figure 4.14. In this case, there are two demonstration models. The undistorted model in Figure 4.14a is the model without the surface inhomogeneity. The distorted model includes the near surface small resistivity boxes as shown in Figure 4.14. Six MT stations are placed with 40 meters spacing between each station. The frequencies used are between 100 and 0.1 kHz. The AMT synthetic data is calculated from the two given models. One is from the undistorted AMT data. Another one is the distorted AMT data. At all station where the resistive inhomogeneity is added, there is a parallel shift in the  $\log_{10}$  apparent resistivity curve as shown in Figure 4.15a and 4.15b.

For the DCR data, there is a total of 41 electrodes with 5 m of electrode spacing as used in the synthetic Case II. The synthetic apparent resistivity responses are generated for the Schlumberger array with pseudodepth at 20 levels,  $n = 1, 2, 3, \dots, 20$ .

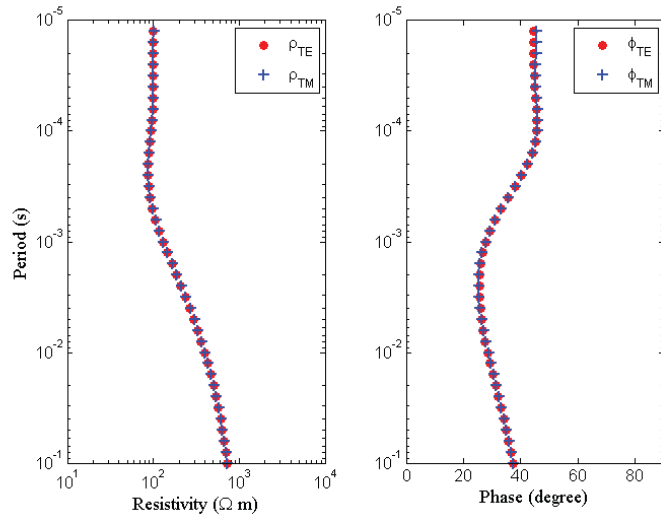
### Inversion result

After running a single MT inversion, the undistorted data inversion produces an accurate model (Figure 4.16a) when compared to the true model (Figure 4.14a). The depth and the thickness of the target were correctly recovered. The resistivity is also close to that of the example model as shown in Figure 4.16a. But for the distorted data inversion, it generates an extremely inaccurate model. The depth of the target layer cannot be recovered which drops further down to 100 m. The layer becomes a finite size reservoir. The resistivity is also inaccurate as shown in Figure 4.16b. Therefore, using distorted AMT data without correction can result in an inaccurate model and also severely mislead an interpretation.

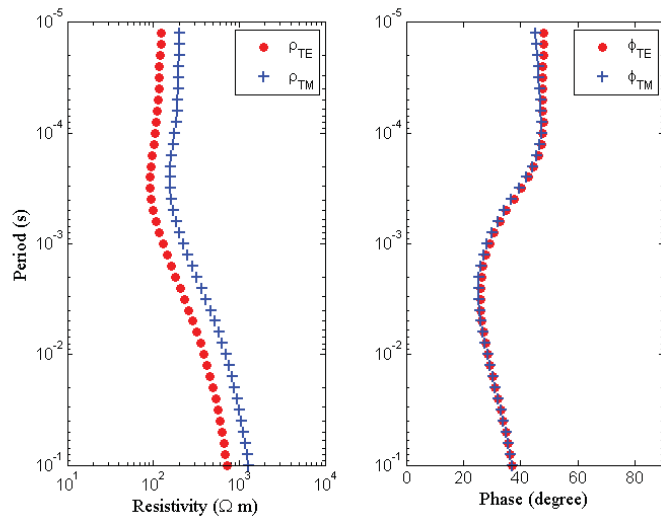
For a single DCR inversion from the DCR data, we can see that all the surface resistive boxes have been mapped which is a common capability of the DCR method (Figure 4.17).

After performing the joint inversion of distorted AMT data and the DCR data, the accuracy of the inverted model is clearly improved. The depth and the thickness of the target layer are exactly recovered. The resistivity is very close to the example model. Moreover the surface inhomogeneity is mapped and included within the same model of MT data as shown in Figure 4.18.

Figure 4.19 shows the calculated data from the joint inversion model with the synthetic data. The red dot and the blue plus sign are the distorted MT data, while the solid red and blue lines are the response calculated from the inverted model. We can see that the response fits well in both apparent resistivity and phase. This indicates that the joint inversion automatically solves the static shift problem within its process.



(a) MT data generated from the undistorted model.



(b) MT data generated from the distorted model.

Figure 4.15: Synthetic data, (a) generated from an example model without surface inhomogeneity. (b) generated from an example model with surface inhomogeneity.

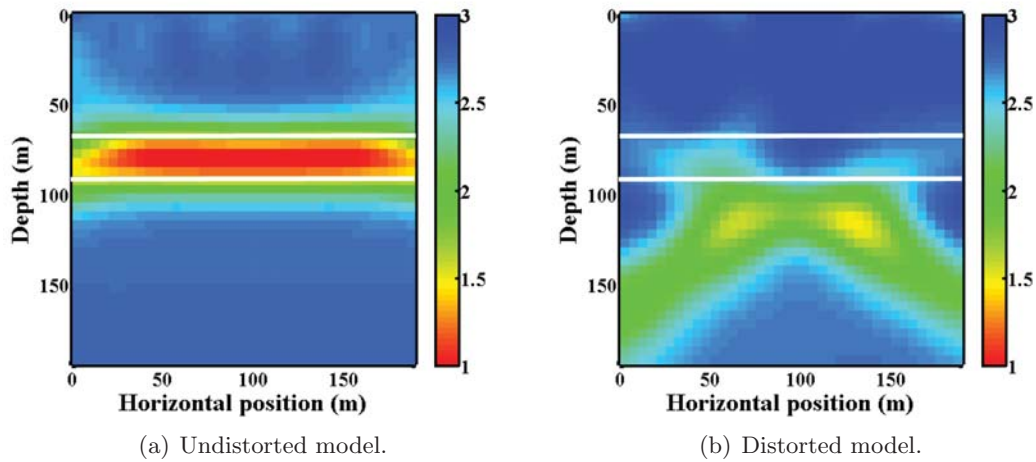


Figure 4.16: The inverted model from a single MT inversion, (a) from the data without surface inhomogeneity. (b) from the data with surface inhomogeneity.

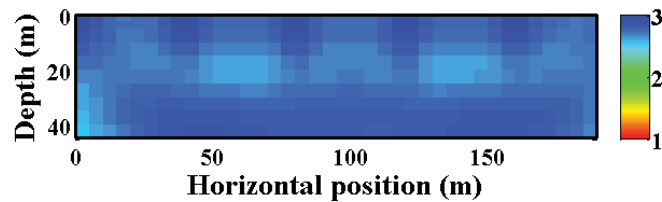


Figure 4.17: Inverted model from a single DCR inversion. The data is generated including the near-surface inhomogeneity

Therefore, it does not need the determination of the level of the shift. It is automatically managed within the joint inversion of MT and DCR. The additional constraint from the DCR survey helps the joint inversion to produce a more reliable model.

### Discussion

In this section, the results show the remarkable benefit of using the joint inversion. The MT static shift removal is confirmed with numerical experiments from synthetic data generated from known models with distorted surface inhomogeneity. The joint inverted results from 2-D profiles can help with constraining the level of static shift in apparent resistivity. The correction is automatically done in the joint inversion process, and so there is no need for a pre-remove shifted curve.

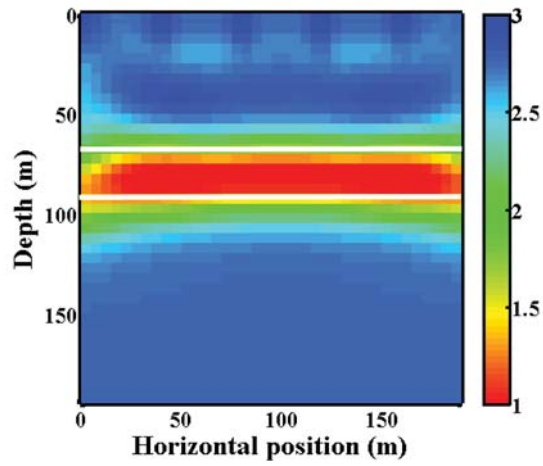


Figure 4.18: Inverted model from joint inversion of DCR & MT.

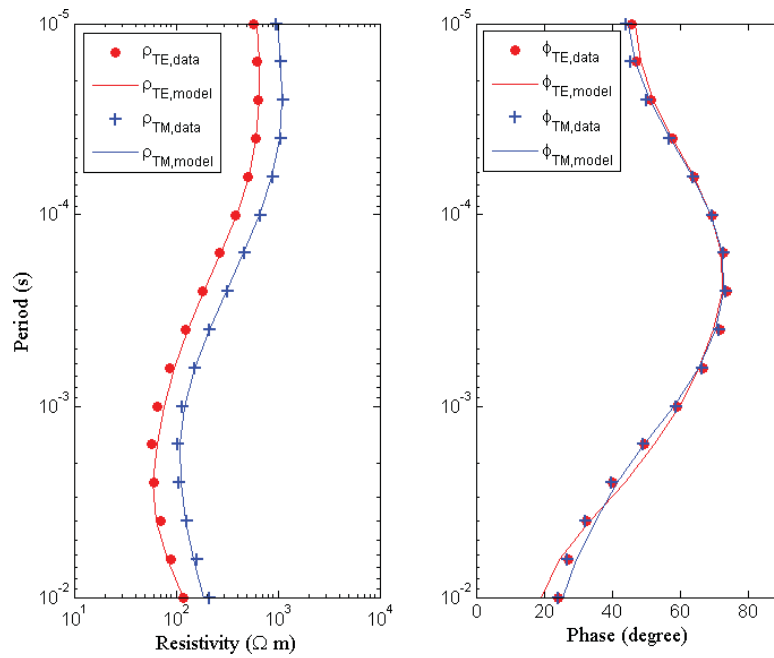


Figure 4.19: The data generated from the inverted model of the joint inversion of DCR & MT.

## 4.2 Real experiment

In this section, we will show the applicability of our codes by applying them to the real observed data from the Cree Extension-Millennium (CreeX) mineralization operated by Cameco Inc. The CreeX project is located in the southeastern portion of the Athabasca Basin, Saskatchewan, Canada which holds the world’s largest uranium deposits. Many geophysical explorations have been performed over this area including the electric and electromagnetic surveys. The goal of the surveys is to map the low resistivity zone of graphite which indicates the unconformity-type uranium deposits. We are authorized to use the AMT and pole-pole DCR data.

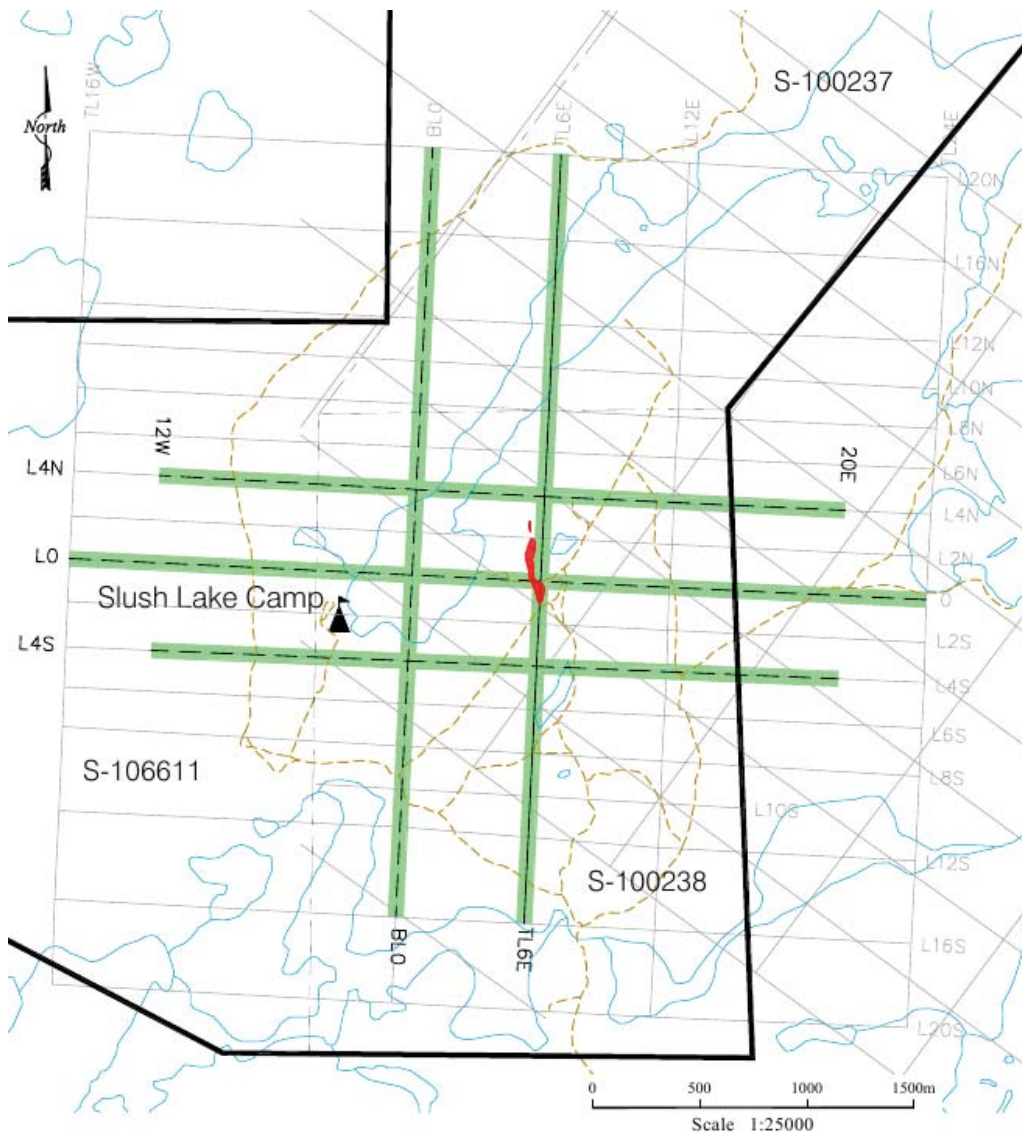


Figure 4.20: The exploration plan at the Cree Extension (CreeX) project (After Cameco Corporation). The established survey grid is used in both AMT and pole-pole DCR surveys. We are authorized to access the data of the profile L0 which passes through the ore mining site.

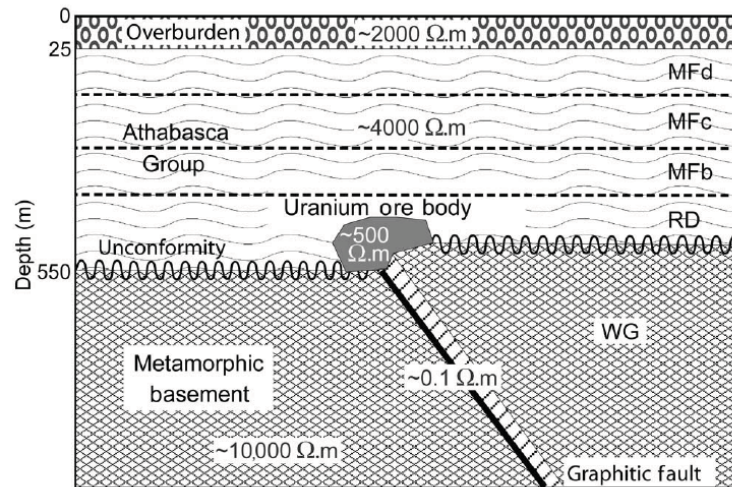


Figure 4.21: The generic model of an unconformity-type uranium deposition in the Athabasca Basin (after Tuncer *et al.*, 2006). There are four major groups of Manitou Falls formation (MF). MFd is the medium-fine sandstone with mudstone intraclasts; MFc is the granule sandstone; MFb is the interbedded conglomerate and pebbly sandstone; and MFa is the discontinuous basal conglomerate, intercalated coarse sandstone, conglomerate and red mudstone. The metamorphic basement consists of the hanging wall of Wollaston Group (WG) and Mudjatik Domain (MD) footwall (see also Mwenifumbo, 2004).

The generic deposition model of the Athabasca Basin is illustrated in Figure 4.21. The investigating area of Athabasca Basin is underlain by the overburden and the altered sandstone and conglomerate sediment. The overburden is about 25 m from the surface. The sandstone-conglomerate sediment thickness is approximately 500 m and consists of four major Manitou Falls formation (MF) group as illustrated in Figure 4.21. The metamorphic basement underlying the sediment is a member of the Wollaston Group (WG). There is a major reverse fault associated with the uranium deposit. The overall resistivity of the area is relatively high. The resistivity of the overburden, sediment and basement are approximately 2000  $\Omega$  m, 4000  $\Omega$  m and 10000  $\Omega$  m. However, the fault is known to be a graphitic fault which exhibits a low resistivity of approximately 0.1 – 10  $\Omega$  m. The uranium ore body is located between the sediment and basement unconformity at the top of the fault. The dimensionality of the data is relatively 2-D with the North-South strike direction under the profile L0 (reported by Cameco Cooperation).

This geological settlement which exhibits the resistivity contrast is suitable for AMT and deep polo-pole DCR surveys. There have been numerous AMT and DCR surveys over this area of Athabasca Basin. However, the results from AMT and DCR are used in the interpretation as separate methods. The deep pole-pole DCR survey

yields the good resolution resistivity model up to 500 m depth suitable to identify the alteration and the conductive basement. However, DCR is less effective when the target depth exceeds 500 m (Tuncer *et al.*, 2006). To map the deeper structure, the AMT survey is introduced. AMT is able to locate the depth of the basement conductor and the fault accurately. However, in some areas, the shallow effect from inhomogeneities could severely distorted AMT data. Here, we expect to apply our developed codes with AMT and DCR data which should improve the accuracy and reliability of the obtained resistivity model.

### Real data configurations and model setup

The AMT data were recorded in 2001–2002 using GEOTRAN-MT operated by EMPulse Geophysics Ltd. There are 18 AMT stations located along the L0 profile at the established grid points labeled as 8W, 6W, 4W, 4E, 5E, 6E, 7E, 8E, 9E, 10E, 11E, 12E, 14E, 16E, 18E, 20E, 22E and 24E. “W” and “E” denotes *West* and *East* respectively according to the reference of the profile origin. For example, 8W indicates that the station is located 800 m to the west of the profile origin. For the L0 profile, the stations are separated by 100 m and 200 m spacing. The denser spacing from station 4E to 12E is associated with the target. There is a large gap between station 4W to 4E due to Slush Lake. The total profile length of the AMT survey is 3200 m. There are 55 frequencies collected in the 8 Hz – 32 kHz bandwidth logarithmically. Note that we selected 28 frequencies for our inversion because the MT data is redundant (Siripunvaraporn & Egbert, 2000). Therefore, there are 2016 of AMT data points (1008 point each from the TE and TM modes) as shown in Figure 4.25.

The pole-pole configuration is selected in this case because its investigation depth is more than other DCR arrays. The electrode positions with 75 m spacing are set along the L0 profile from 15W to 24E which gives the total profile length of 3900 m. The current and the potential electrode are separated from each other. There are 12 pseudodepths because of the repeating of the 75 m electrode spacing, i.e. 75, 150, 225, 300, 375, 450, 525, 600, 675, 750, 825 and 900 m. We eliminate the extreme value points in the DCR data before applying our inversion. There are 718 of DCR data points in total.

We use a homogeneous halfspace as the starting and reference model. The model is discretized into a  $180 \times 48$  mesh with the given resistivity of  $6000 \Omega \text{ m}$  determined from prior geology information. The number of model parameters  $M = 8640$  which is much larger than the number of data points. Both single and joint inversions are performed using the same starting and reference models. We will validate the results by comparing with the geology information and previous geophysical studies.

## Inversion results

For the single inversion of DCR, the obtained model is shown in Figure 4.22. The RMS misfit is reduced from 10.65 to 3.12 which indicates that the total error is 31%. This error value of 31% is higher than the simple synthetic result in section 4.1 whose data is fitted within 5% error. However, the relatively high error could occur in the real experiments especially in this complex geology case. Therefore, 31% is satisfactory in this case. The resistivity model obtained from the DCR inversion moderately recovers remarkable geology targets including sandstone alteration, the basement and the conductive target. Due to the limitation of the DCR investigation depth, the sandstone alteration in the sedimentary layer ( $\approx 50\text{ m} - 500\text{ m}$  depth) can be resolved. The basement is indistinctly recovered. However, it can be identified from the transition from the sediment alteration to the smooth basement at approximately 500 m which follows the geological backgrounds. The conductive package can be found at a depth of 500 m – 600 m. The horizontal location of the conductive target corresponds to the ore body (the mineralization is located at the AMT station 6E). However, the conductor package could be a feature added by the inversion because it is deeper than the investigation depth. The low resistivity ( $\approx 500\ \Omega\text{ m}$ ) “halo” located around the conductive target could be the silicification above the ore-body or the inversion halo from the smoothness constraint (as mentioned in Section 3.5.4). The resistivity of the obtained model at the overburden and sediment layer is relatively high (higher than the expected values of  $200\ \Omega\text{ m}$  and  $4000\ \Omega\text{ m}$  from the geological model) which could be due to the fitting criteria of the inversion associated with the high resistivity basement. Note that there is no fault track presented in the model.

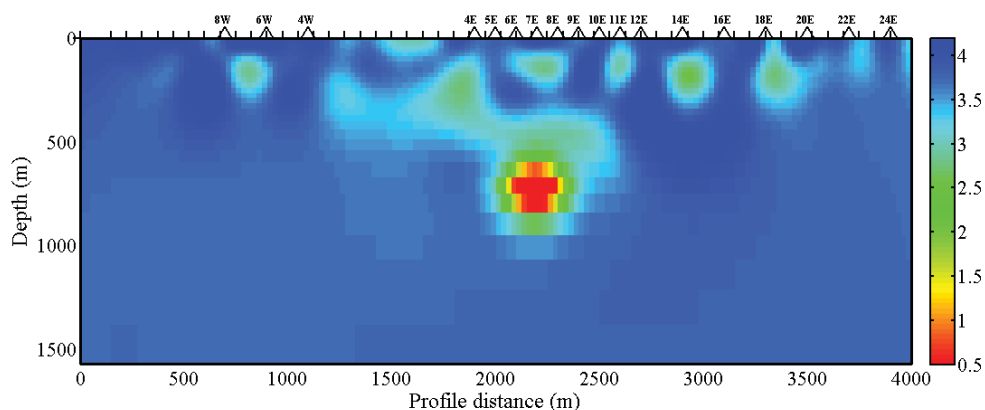


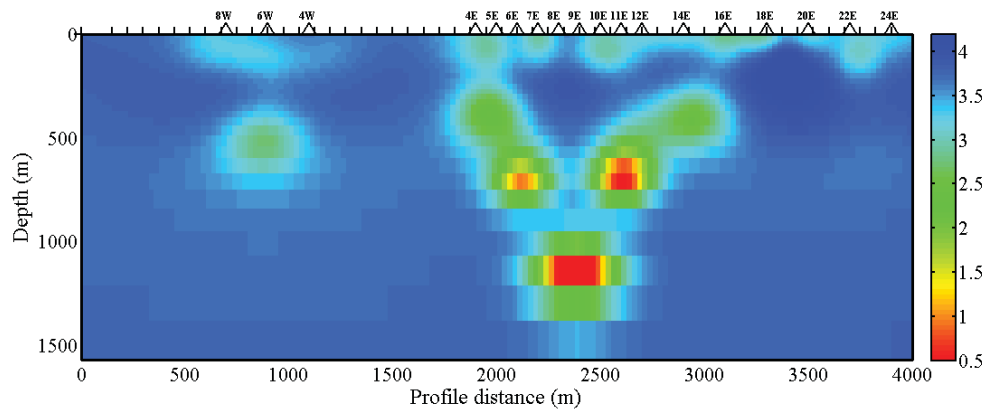
Figure 4.22: The resistivity model from a single DCR inversion.

For the AMT data, we apply the inversion for TE mode only (TE inversion), TM mode only (TM inversion) and TE&TM mode (TE&TM inversion) as shown

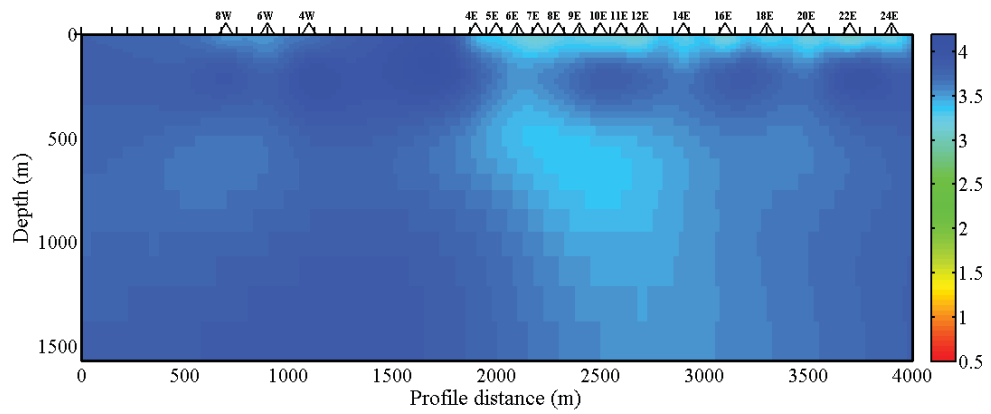
in Figure 4.23. As discussed in Berdichevsky (1999), the TE mode senses the inductive features of the subsurface, especially when there is an along-strike conductive structure. The TM mode usually maps the lateral resistivity variation with a better resolution. However, for this case, the vertical conductive graphitic fault causes the TE mode data to exhibit a very strong response as shown in Figure 4.26 while the TM mode shows a low single-site variation of the apparent resistivity response as shown in Figure 4.27. The resistivity model of the TE mode only and the TM mode only are shown in Figure 4.23a and 4.23b respectively. As expected, the model obtained from the TE mode is superior in mapping the conductive structure than the model obtained from the TM mode in this case. The TM mode does not image the conductor at all. However, the TM mode provides information about the lateral resistivity layer including the overburden layer and transition zone between the sediment of the basement layer. The resistivity model from the TE inversion presents the three packages of the conductor. The shallow conductor packages are located approximately 600 m under the 7E and 10E stations. The conductor under the 7E station is thus interpreted as the ore-body target. The conductor under the station 10E could be an artifact associated with the surface distortion at 10E and 11E as reported by EMPulse Geophysics Ltd. The deeper conductor package is due to the graphitic fault. However, the TE mode does not clearly indicate the fault track and the sediment alteration. The TE&TM inversion gives a more reasonable model than the individual TE and TM inversions. The fault track clearly appears in the model which extends a further 2–3 km as expected from the geological model. The overburden, the sediment and the basement layer are separated corresponding to the geological model. The conductor packages are correctly resolved into two separated packages along the fault. However, the continuity of the conductive target and the sediment layer are expected to be improved by the joint inversion.

For the joint inversion of the DCR and AMT data, we apply the joint inversion to TE+DCR, TM+DCR and TE&TM+DCR data. The resistivity models from the inversions are shown in Figure 4.24. For the TE+DCR and TM+DCR inversion, the obtained models are superior to the single TE and TM inversion. The TE+DCR model is not much better than the TE inversion model. Only the conductive base is better resolved. The fault track is still not recovered. However, for the TM+DCR inversion, we see a significant improvement. The DCR data helps with locating the conductive target. The fault track is clearly identified in this model. The conductive basement is also recovered. However, some vertical discontinuity in the sediment layer is expected to be improved.

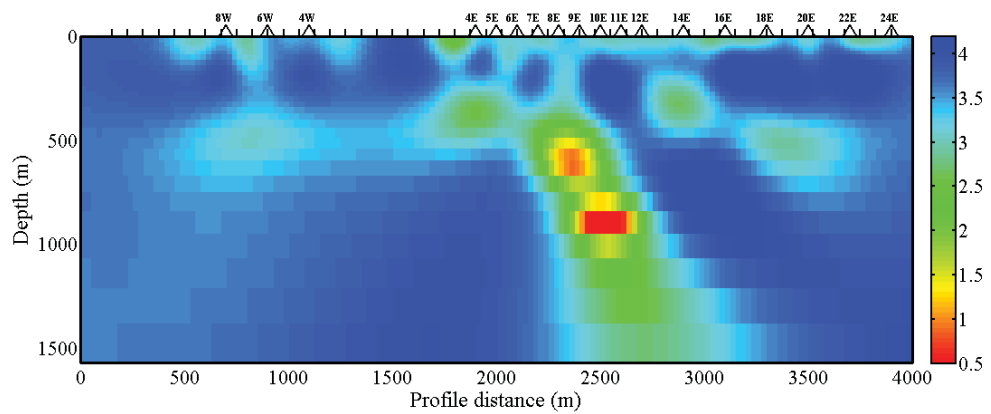
The joint inversion of TE&TM+DCR seems to give the best estimation of the geological model. The joint inversion inherits the remarkable features from all the



(a) Resistivity model obtained from the TE mode only inversion.

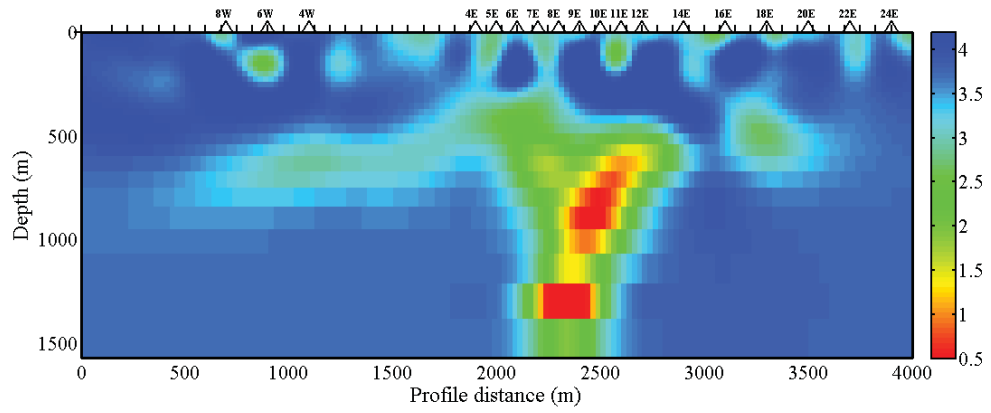


(b) Resistivity model obtained from the TM mode only inversion.

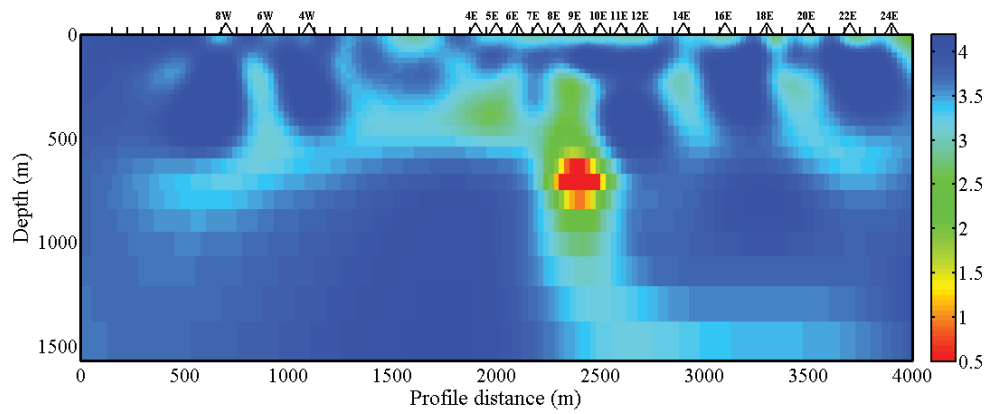


(c) Resistivity model obtained from the TE&TM modes inversion.

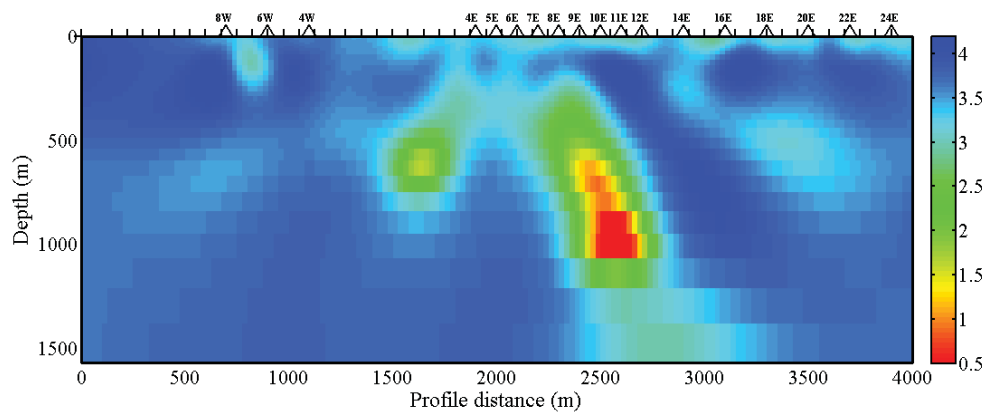
Figure 4.23: The resistivity models obtained from a single MT inversion. (a) TE mode only, (b) TM model only and (c) TE&TM modes.



(a) Resistivity model obtained from the TE+DCR inversion.

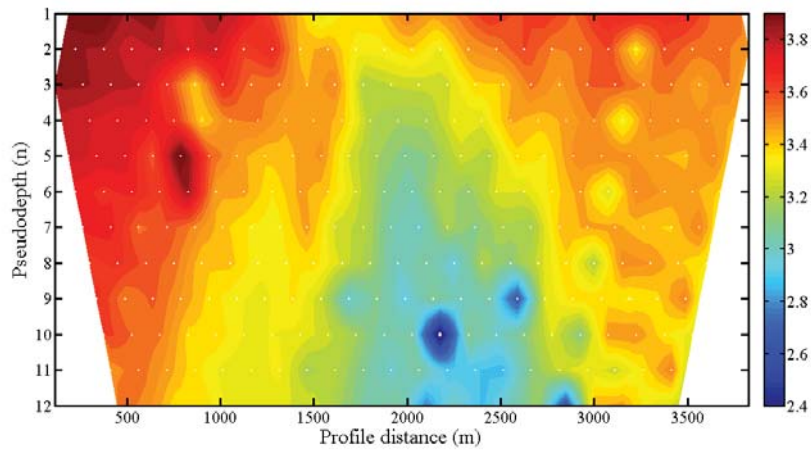


(b) Resistivity model obtained from the TM+DCR inversion.

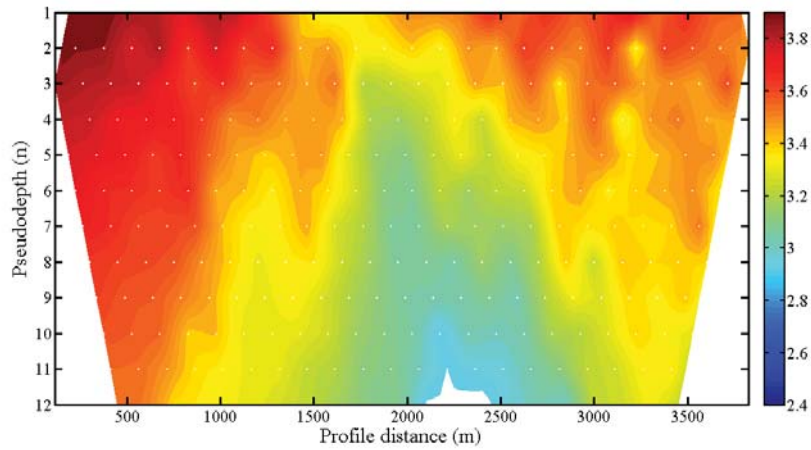


(c) Resistivity model obtained from the TE&TM + DCR inversion.

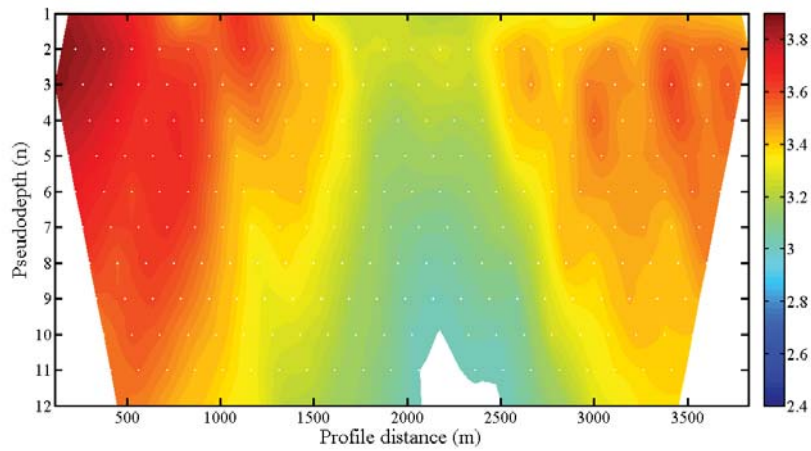
Figure 4.24: The resistivity models obtained from a joint inversion. (a) TE+DCR, (b) TM+DCR (c) TE&TM+DCR.



(a) DCR synthetic data: Schlumberger array.

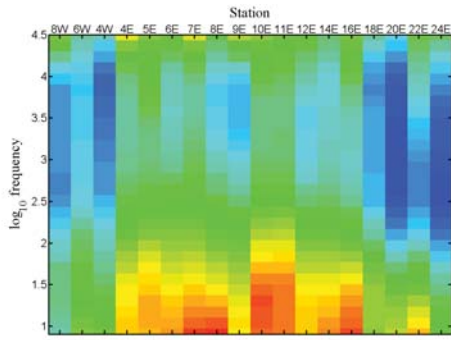


(b) The generated DCR data of the inverted model from a single DCR inversion.

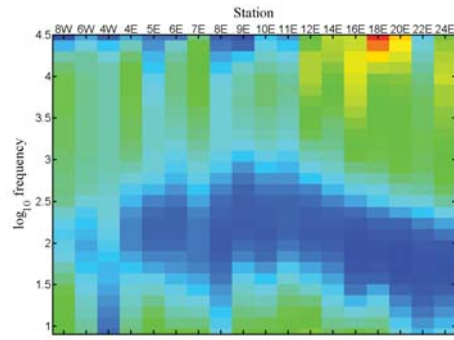


(c) The generated DCR data of the inverted model from a joint inversion of DCR and MT.

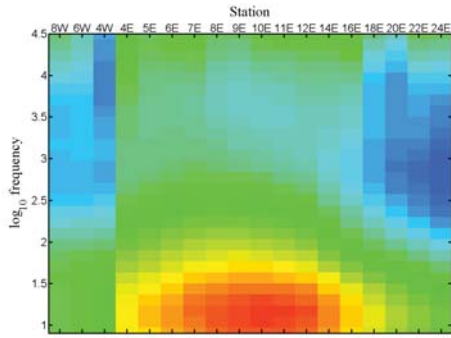
Figure 4.25: DCR data of Schlumberger array from the inversions. All use the same color scale



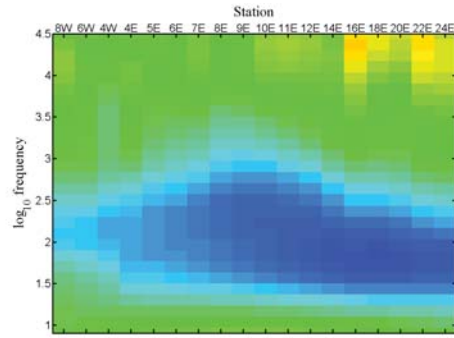
(a) Observed apparent resistivity for TE.



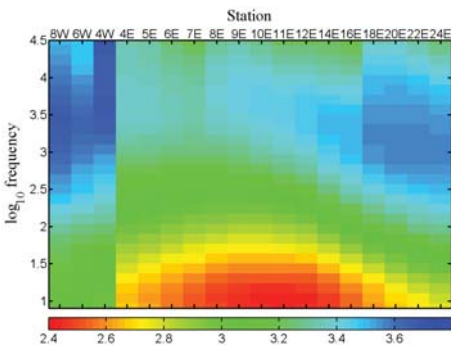
(b) Observed phase for TE.



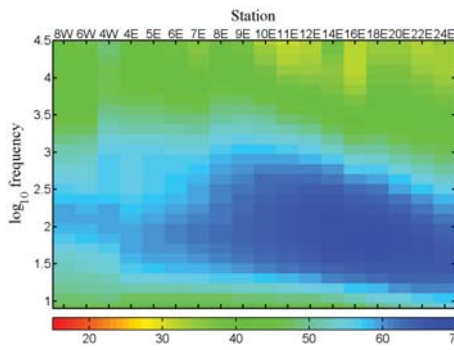
(c) Calculated apparent resistivity for TE from a single MT inversion.



(d) Calculated phase for TE from a single MT inversion.

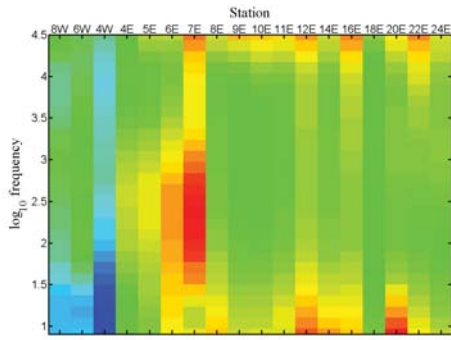


(e) Calculated apparent resistivity for TE from the DCR+MT joint inversion.

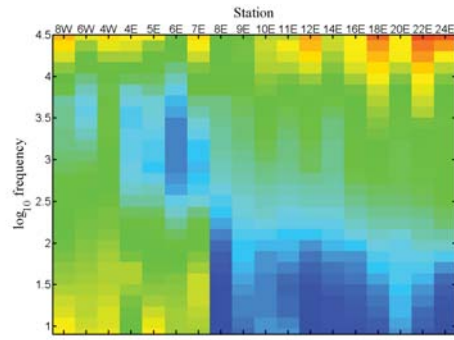


(f) Calculated phase for TE from the DCR+MT joint inversion.

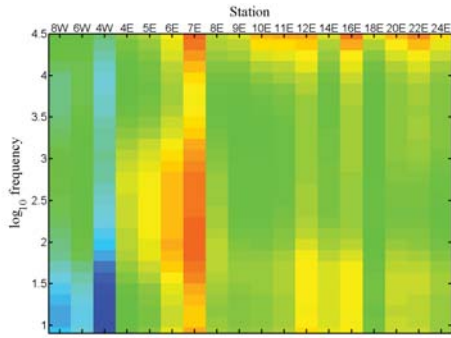
Figure 4.26: Apparent resistivity and phase responses in TE mode from the MT inversions.



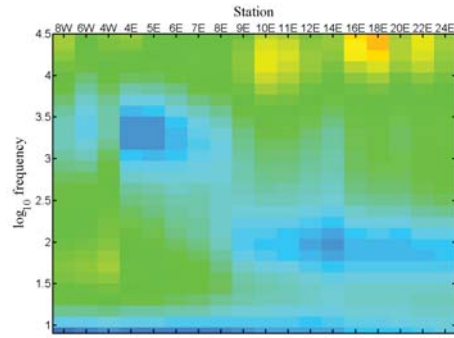
(a) Observed apparent resistivity for TM.



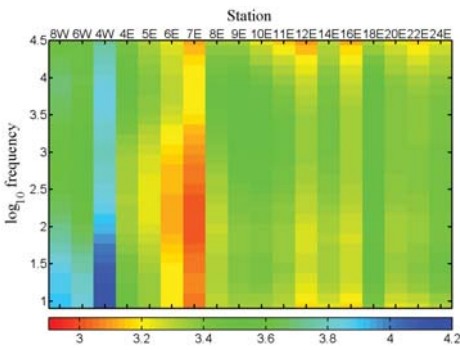
(b) Observed phase for TM.



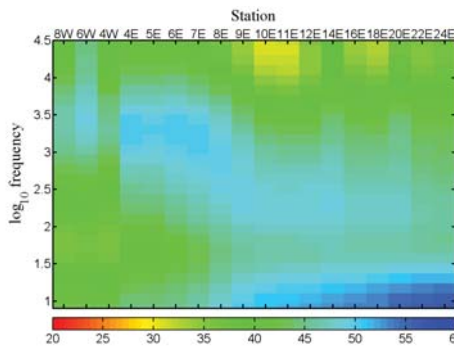
(c) Calculated apparent resistivity for TM from a single MT inversion.



(d) Calculated phase for TM from a single MT inversion.

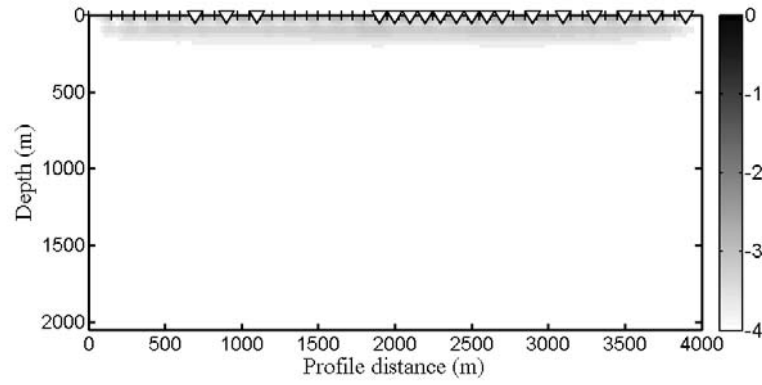


(e) Calculated apparent resistivity for TM from the DCR+MT joint inversion.

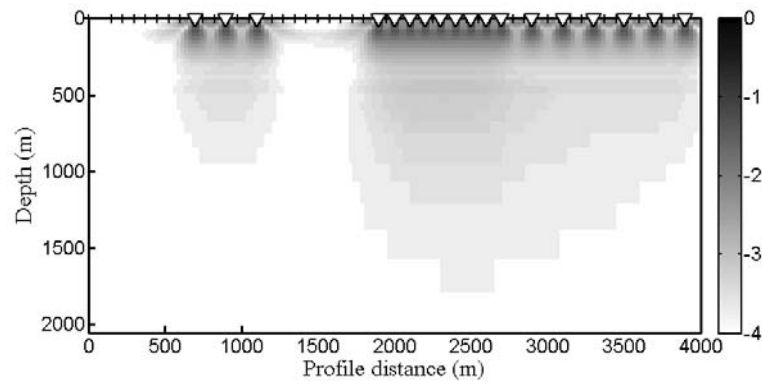


(f) Calculated phase for TM from the DCR+MT joint inversion.

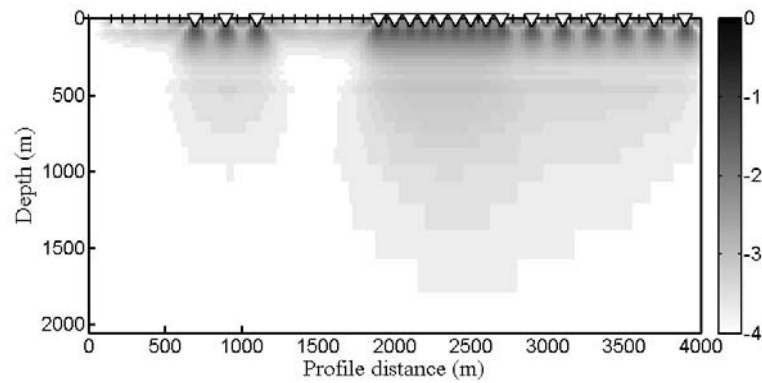
Figure 4.27: Apparent resistivity and phase responses in TM mode from the MT inversions.



(a) Model resolution matrix of the DCR inversion.



(b) Model resolution matrix of the TE&TM inversion.



(c) Model resolution matrix of the joint the TE&TM+DCR inversion.

Figure 4.28: The model resolution matrix (a) DCR, (b) TE&TM (c) TE&TM+DCR.

data sets. Here, the overburden is clearly identified by the close value to the geological model ( $\approx 2000 \Omega \text{ m}$ ) at the reasonable depth of  $< 100 \text{ m}$ . The sediment layer is recovered. The conductive graphitic fault is also recovered. The conductor continuing along the fault is dedicated to the graphite as shown in Figure 4.21. It is better illustrated in the TE&TM+DCR joint inversion. As mentioned, the low resistivity of approximately  $500 \Omega \text{ m}$  could be the silicification or the clay alteration or the smoothness constraint halo. The footwall and the hanging wall are reasonably recovered. The hanging wall (right side of the fault) is expected to have more resistivity than the footwall. Note that the WG have larger resistivity value than MD. As in Figure 4.28, the MRM also illustrates the better resolution for the joint inversion.

## Discussion

The joint inversion of DCR and AMT has proved to be an efficient tool for mapping the ore-body. The resolution and the reliability of the model obtained from the joint inversion are superior to those from the individual inversions. The geological structures including the overburden, the sandstone sediment, the basement, the conductive graphitic fault and the ore-body are reasonably resolved with the joint inversion from the surface to 2–3 km depth.

Therefore, we have verified that our developed joint inversion works for both synthetic tests and for real experiments. The obtained model from the joint inversion is more accurate and reliable than the single inversions.

## CHAPTER V

### CONCLUSION

The goal of this thesis is to develop the efficient 2-D joint inversion of DCR data and MT data and demonstrate the benefit of the integrated DCR and MT survey.

In order to develop the efficient joint inversion of DCR and MT data, we follow the data space Occam's inversion (DASOCC) proposed by Siripunvaraporn & Egbert (2000). The DASOCC algorithm is a variant of the original Occam's inversion proposed by Constable *et al.* (1987) which is formerly associated with the model space calculation including the  $M \times M$  system. The DASOCC algorithm reduces the computational domain from  $M \times M$  of the original model space to  $N \times N$  of the data space. The number of data point  $N$  is usually less than the number of model parameters  $M$ . Therefore, DASOCC significantly decreases the computational time and the memory usage while preserving the stability and robustness of the original Occam's algorithm. The 2-D forward modeling and the sensitivity calculation routines of the DCR and MT methods are implemented based on the original 2-D DCR inversion of Vachirastienchai (2007) and the 2-D MT inversion of Siripunvaraporn & Egbert (2000).

The developed joint inversion codes are written in 8500 lines of FORTRAN 95/2003 script based on the GNU gfortran 4.4 compiler with LAPACK library version 3. All the codes are run and tested on the Linux (Ubuntu 10.04) system. The flexibility, robustness, accuracy and reliability of the codes are verified with both synthetic and real experiments.

We firstly validate our code with the synthetic experiments. The synthetic case I shows that our developed code is working and also stable and robust. The superior accuracy of the joint inversion is demonstrated with the complex model in the synthetic case II. The reliability of the joint inversion is illustrated in the synthetic case III. With the joint inversion, the MT static shift effect is corrected. Our developed code is also applied to the real data from CreeX project in Canada and give remarkable benefits of using the joint inversion to the real explorations. The results from both synthetic and real experiments demonstrate that the obtained model from the joint inversion is superior to those from the single DCR or MT inversion in terms of the accuracy and reliability. In addition, our developed codes are more efficient in both computational time and memory usage than to the existing joint inversion.

With the fact that the DCR survey is usually easier and faster, researchers and surveyors should conduct the DCR survey along the RMT and AMT survey to increase the accuracy and reliability of the subsurface model. However, the integration of the DCR with the typical MT survey which is usually conducted for very deep exploration (up to 100 km) has not yet been demonstrated due to the very large difference in investigating area. The typical MT survey can occupy the investigation profile of up to several hundreds of kilometers while the largest profile of the deep DCR survey is only a few kilometers. This difference means that it is impractical to implement both surveys into the same computational model. A further separated domain scheme such as the domain decomposition and the Chimera methods can be applied to this problem.

From our demonstrations, we conclude that the integrated DCR and MT survey can be pushed to be the standard of future electric and electromagnetic surveys with our efficient joint inversion program.

## REFERENCES

- ALUMBAUGH, D. & NEWMAN, A., 2000 “Image appraisal for 2-D and 3-D electromagnetic inversion,” *Geophysics* **65**, 1455–1467.
- AUKEN, E. & CHRISTIANSEN, A., 2004 “Layered and laterally constrained 2D inversion of resistivity data,” *Geophysics* **69**, 752–761.
- AVDEEV, D. & AVDEEVA, A., 2009 “3D magnetotelluric inversion using a limited-memory quasi-Newton optimization,” *Geophysics* **74**, F45–F57.
- AVRIEL, M. & WILDE, D. J., 1966 “Optimality proof for the symmetric Fibonacci search technique,” *Fibonacci Quart.* **4**, 265–269.
- BERDICHEVSKY, M., 1999 “Marginal notes on magnetotellurics,” *Surveys in Geophysics* **20**, 341–375.
- BJOERCK, A., 1967 “Solving linear least squares problems by Gram-Schmidt orthogonalization,” *BIT* **7**, 1–21.
- BOONCHAIKUL, S., 2007 “Two-dimensional direct current resistivity inversion: finite element method,” *Mahidol University* .
- BOONCHAIKUL, S., VACHIRATIENCHAI, C. & SIRIPUNVARAPORN, W., 2008 “Two-dimensional direct current (DC) resistivity inversion: Data space Occam’s approach,” *Physics of the Earth and Planetary Interiors* **168**, 204 – 211.
- BUSELLI, G. & LU, K., 2001 “Groundwater contamination monitoring with multichannel electrical and electromagnetic methods,” *Journal of Applied Geophysics* **48**, 11–23.
- CANDANSAYAR, T. B., M.E., 2008 “Two-dimensional joint inversion of radiomagnetotelluric and direct current resistivity data,” *Geophysical Prospecting* **56**, 737–749.
- CHUNDURU, R., SEN, M. & STOFFA, P., 1997 “Hybrid optimization methods for geophysical inversion,” *Geophysics* **62**, 1196–1207.
- CONSTABLE, S., ORANGE, A., HOVERSTEN, G. & MORRISON, F., 1998 “Marine magnetotellurics for petroleum exploration: Part I: a sea-floor equipment system,” *Geophysics* **63**, 816–825.

- CONSTABLE, S., PARKER, R. & CONSTABLE, C., 1987 "Occam's inversion: a practical algorithm for generating smooth models from electromagnetic sounding data." *Geophysics* **52**, 289–300.
- CORWIN, D. & LESCH, S., 2005 "Apparent soil electrical conductivity measurements in agriculture," *Computers and Electronics in Agriculture* **46**, 11–43.
- DEGROOT-HEDLIN, C. & CONSTABLE, S., 1990 "Occam's inversion to generate smooth, two-dimensional models from magnetotelluric data," *Geophysics* **55**, 1613–1624.
- DEGROOT-HEDLIN, C. & CONSTABLE, S., 2004 "Inversion of magnetotelluric data for 2D structure with sharp resistivity contrasts," *Geophysics* **69**, 78–86.
- DEY, A. & MORRISON, F., 1979 "Resistivity modelling for arbitrarily shaped two-dimensional structures," *Geophysical Prospecting* **27**, 106–136.
- ELLIS, R. & OLDENBURG, D., 1994 "Applied geophysical inversion," *Geophysical Journal International* **116**, 5–11.
- FARQUHARSON, C. & CRAVEN, J., 2009 "Three-dimensional inversion of magnetotelluric data for mineral exploration: An example from the McArthur River uranium deposit, Saskatchewan, Canada," *Journal of Applied Geophysics* **68**, 450–458.
- GUNTHER, T., RUCKER, C. & SPITZER, K., 2006 "Three-dimensional modelling and inversion of dc resistivity data incorporating topography - II. Inversion," *Geophysical Journal International* **166**, 506–517.
- HABER, E. & OLDENBURG, D., 2000 "A gcv based method for nonlinear ill-posed problems," *Computational Geosciences* **4**, 41–63.
- HARINARAYANA, T., 1999 "Combination of EM and DC measurements for upper crustal studies," *Surveys in Geophysics* **20**, 257–278.
- INGHAM, M. & BROWN, C., 1998 "A magnetotelluric study of the Alpine Fault, New Zealand," *Geophysical Journal International* **135**, 542–552.
- JUPP, D. & VOZOFF, K., 1977 "Resolving anisotropy in layered media by joint inversion," *Geophysical Prospecting* **25**, 460–470.
- KARLIK, G. & KAYA, M., 2001 "Investigation of groundwater contamination using electric and electromagnetic methods at an open waste-disposal site: A case study from Isparta, Turkey," *Environmental Geology* **40**, 725–731.

- KIEFER, J., 1953 "Sequential minimax search for a maximum," *Proceedings of the American Mathematical Society* **4**, 502–506.
- LOKE, M. & BARKER, R., 1996 "Rapid least-squares inversion of apparent resistivity pseudosections by a quasi-Newton method," *Geophysical Prospecting* **44**, 131–152.
- LYTLE, J. & DINES, K., 1980 "Iterative ray tracing between boreholes for underground image reconstruction." *IEEE Transactions on Geoscience and Remote Sensing* **GE-18**, 234–240.
- MITSUHATA, Y., MATSUO, K. & MINEGISHI, M., 1999 "Magnetotelluric survey for exploration of a volcanic-rock reservoir in the Yurihara oil and gas field, Japan," *Geophysical Prospecting* **47**, 195–218.
- MONTEIRO SANTOS, F., ANDRADE AFONSO, A. & DUPIS, A., 2007 "2D joint inversion of dc and scalar audio-magnetotelluric data in the evaluation of low enthalpy geothermal fields," *Journal of Geophysics and Engineering* **4**, 53–62.
- MWENIFUMBO, E. B. J. C. B. G. P. K., C.J., 2004 "Physical rock properties from the athabasca group: Designing geophysical exploration models for unconformity uranium deposits," *Journal of Applied Geophysics* **55**, 117–135.
- OGAWA, Y., MATSUSHIMA, N., OSHIMA, H., TAKAKURA, S., UTSUGI, M., HIRANO, K., IGARASHI, M. & DOI, T., 1998 "A resistivity cross-section of Usu volcano, Hokkaido, Japan, by audiomagnetotelluric soundings," *Earth, Planets and Space* **50**, 339–346.
- OLDENBURG, D. & LI, Y., 1999 "Estimating depth of investigation in dc resistivity and IP surveys," *Geophysics* **64**, 403–416.
- PEDERSEN, L., BASTANI, M. & DYNESIUS, L., 2005 "Groundwater exploration using combined controlled-source and radiomagnetotelluric techniques," *Geophysics* **70**, G8–G15.
- PRESS, W. H., FLANNERY, B. P., TEUKOLSKY, S. A. & VETTERLING, W. T., 1992 *Numerical Recipes in FORTRAN 77: The Art of Scientific Computing (v. 1)*, 2 edn. (Cambridge University Press).
- RAICHE, A., JUPP, D., RUTTER, H. & VOZOFF, K., 1985 "The joint use of coincident loop transient electromagnetic and Schlumberger sounding to resolve layered structures," *Geophysics* **50**, 1618–1627.

- RODI, W. & MACKIE, R., 2001 “Nonlinear conjugate gradients algorithm for 2-D magnetotelluric inversion,” *Geophysics* **66**, 174–187.
- SASAKI, Y., 1989 “Two-dimensional joint inversion of magnetotelluric and dipole-dipole resistivity data,” *Geophysics* **54**, 254–262.
- SASAKI, Y. & MEJU, M., 2006 “Three-dimensional joint inversion for magnetotelluric resistivity and static shift distributions in complex media,” *Journal of Geophysical Research B: Solid Earth* **111**.
- SCHWARZBACH, C., BORNER, R. & SPITZER, K., 2005 “Two-dimensional inversion of direct current resistivity data using a parallel, multi-objective genetic algorithm,” *Geophysical Journal International* **162**, 685–695.
- SIRIPUNVARAPORN, W. & EGBERT, G., 2000 “An efficient data-subspace inversion method for 2-D magnetotelluric data,” *Geophysics* **65**, 791–803.
- SIRIPUNVARAPORN, W., EGBERT, G., LENBURY, Y. & UYESHIMA, M., 2005 “Three-dimensional magnetotelluric inversion: data-space method,” *Physics of The Earth and Planetary Interiors* **150**, 3 – 14.
- SIRIPUNVARAPORN, W., UYESHIMA, M. & EGBERT, G., 2004 “Three-dimensional inversion for Network-Magnetotelluric data,” *Earth, Planets and Space* **56**, 893–902.
- SMITH, J. & BOOKER, J., 1991 “Rapid inversion of two- and three-dimensional magnetotelluric data,” *Journal of Geophysical Research* **96**, 3905–3922.
- TEZKAN, B., 1999 “A review of environmental applications of quasi-stationary electromagnetic techniques,” *Surveys in Geophysics* **20**, 279–308.
- TEZKAN, B., GEORGESCU, P. & FAUZI, U., 2005 “A radiomagnetotelluric survey on an oil-contaminated area near the Brazi Refinery, Romania,” *Geophysical Prospecting* **53**, 311–323.
- TRIPP, A., WARD, S., STILL, W., SWIFT JR., C. & PETRICK, W., 1978 “Electromagnetic and schlumberger resistivity sounding in the roosevelt hot springs kgra.” *Geophysics* **43**, 1450–1469.
- TUNCER, V., UNSWORTH, J., M., SIRIPUNVARAPORN, W. & , J. A., CRAVEN, 2006 “Exploration for unconformity-type uranium deposits with audiomagnetotelluric data: A case study from the McArthur River mine, Saskatchewan, Canada,” *Geophysics* **71**, B201–B209.

- VACHIRATIENCHAI, C., 2007 “Two-dimensional direct current resistivity inversion: finite difference method,” *Mahidol University* .
- VOZOFF, K. & JUPP, D., 1975 “Joint inversion of geophysical data,” *Geophys. J. Roy. Astr. Soc.* **42**, 977–991.
- XU, S., DUAN, B. & ZHANG, D., 2000 “Selection of the wavenumbers k using an optimization method for the inverse fourier transform in 2.5D electrical modelling,” *Geophysical Prospecting* **48**, 789–796.
- ZHANG, J., MACKIE, R. & MADDEN, T., 1995 “3-D resistivity forward modeling and inversion using conjugate gradients,” *Geophysics* **60**, 1313–1325.
- ZOHDY, A. & BISDORF, R., 1990 “Schlumberger soundings near Medicine Lake, California,” *Geophysics* **55**, 956–964.

## BIOGRAPHY

<b>NAME</b>	Mr. Puwis Amatyakul
<b>DATE OF BIRTH</b>	7 <sup>th</sup> November 1984
<b>PLACE OF BIRTH</b>	Bangkok, Thailand
<b>INSTITUTIONS ATTENDED</b>	Mahidol University, 2003-2007 Bachelor of Science (Physics) Mahidol University, 2007-2010 Master of Science (Physics)
<b>SCHOLARSHIPS</b>	The Development and Promotion of Science and Technology Talent Project, 2000-present Research assistance, Thailand Center of Excellence in Physics, 2009-present Teacher assistance, Faculty of Science, Mahidol University 2007-2008
<b>HOME ADDRESS</b>	31/72, Ngamwongwan Road Laksi, Bangkok Thailand, 10210
<b>E-MAIL</b>	puwis.mahidol@gmail.com